NAVAL POSTGRADUATE SCHOOL

MONTEREY, CALIFORNIA

THESIS

THERMOPHOTOVOLTAIC ENERGY CONVERSION IN SPACE NUCLEAR REACTOR POWER SYSTEMS

by

Andrew L. Presby

December 2004

Thesis Advisors: Ashok Gopinath
              Sherif Michael

Approved for public release; distribution is unlimited

THIS PAGE INTENTIONALLY LEFT BLANK

REPORT DOCUMENTATION PAGE		*Form Approved OMB No. 0704-0188*

Public reporting burden for this collection of information is estimated to average 1 hour per response, including the time for reviewing instruction, searching existing data sources, gathering and maintaining the data needed, and completing and reviewing the collection of information. Send comments regarding this burden estimate or any other aspect of this collection of information, including suggestions for reducing this burden, to Washington headquarters Services, Directorate for Information Operations and Reports, 1215 Jefferson Davis Highway, Suite 1204, Arlington, VA 22202-4302, and to the Office of Management and Budget, Paperwork Reduction Project (0704-0188) Washington DC 20503.

1. AGENCY USE ONLY (*Leave blank*)	2. REPORT DATE December 2004	3. REPORT TYPE AND DATES COVERED Master's Thesis	
4. TITLE AND SUBTITLE: Thermophotovoltaic Energy Conversion in Space Nuclear Reactor Power Systems			**5. FUNDING NUMBERS**
6. AUTHOR(S) Andrew L. Presby, LT, USN			
7. PERFORMING ORGANIZATION NAME(S) AND ADDRESS(ES) Naval Postgraduate School Monterey, CA 93943-5000			**8. PERFORMING ORGANIZATION REPORT NUMBER**
9. SPONSORING /MONITORING AGENCY NAME(S) AND ADDRESS(ES) N/A			**10. SPONSORING/MONITORING AGENCY REPORT NUMBER**

11. SUPPLEMENTARY NOTES The views expressed in this thesis are those of the author and do not reflect the official policy or position of the Department of Defense or the U.S. Government.

12a. DISTRIBUTION / AVAILABILITY STATEMENT Approved for public release; distribution is unlimited	12b. DISTRIBUTION CODE

13. ABSTRACT (maximum 200 words)

   Thermophotovoltaic energy conversion offers a means of efficiently converting heat into electrical power. This has potential benefits for space nuclear reactor power systems currently in development. The primary obstacle to space operation of thermophotovoltaic devices appears to be the low heat rejection temperatures which necessitate large radiator areas. A study of the tradespace between efficiency and radiator size indicates that feasible multi-junction TPV efficiencies result in substantial overall system mass reduction with manageable radiator area. The appendices introduce the endothermodynamic model of a TPV cell and briefly assess the utility of advanced carbon-carbon heat pipe radiator concepts.

14. SUBJECT TERMS Space nuclear fission reactor, thermophotovoltaics, thermophotovoltaic, thermophotovoltaic cell, radiator, carbon carbon heat pipe, nuclear electric propulsion	15. NUMBER OF PAGES 147
	16. PRICE CODE

17. SECURITY CLASSIFICATION OF REPORT Unclassified	18. SECURITY CLASSIFICATION OF THIS PAGE Unclassified	19. SECURITY CLASSIFICATION OF ABSTRACT Unclassified	20. LIMITATION OF ABSTRACT UL

THIS PAGE INTENTIONALLY LEFT BLANK

THERMOPHOTOVOLTAIC ENERGY CONVERSION IN SPACE NUCLEAR REACTOR POWER SYSTEMS

Andrew L. Presby
Lieutenant, United States Navy
B.S., Carnegie Mellon University, 1997

Submitted in partial fulfillment of the
requirements for the degree of

ASTRONAUTICAL ENGINEER
and
MASTER OF SCIENCE IN ASTRONAUTICAL ENGINEERING

from the

NAVAL POSTGRADUATE SCHOOL
December 2004

Author: LT Andrew L. Presby, USN

Approved by: Dr Ashok Gopinath
                 Thesis Advisor

                 Dr. Sherif Michael
                 Co-Advisor

                 Dr. Anthony J. Healey
                 Chairman, Department of Mechanical and Astronautical
                 Engineering

THIS PAGE INTENTIONALLY LEFT BLANK

ABSTRACT

Thermophotovoltaic energy conversion offers a means of efficiently converting heat into electrical power. This has potential benefits for space nuclear reactor power systems currently in development. The primary obstacle to space operation of thermophotovoltaic devices appears to be the low heat rejection temperatures which necessitate large radiator areas. A study of the tradespace between efficiency and radiator size indicates that feasible multi-junction TPV efficiencies result in substantial overall system mass reduction with manageable radiator area. The appendices introduce the endothermodynamic model of a TPV cell and briefly assess the utility of advanced carbon-carbon heat pipe radiator concepts.

THIS PAGE INTENTIONALLY LEFT BLANK

TABLE OF CONTENTS

LIST OF FIGURES

x

THIS PAGE INTENTIONALLY LEFT BLANK

LIST OF TABLES

THIS PAGE INTENTIONALLY LEFT BLANK

ACKNOWLEDGMENTS

THIS PAGE INTENTIONALLY LEFT BLANK

I. INTRODUCTION

Nuclear reactor power systems have long been utilized to provide mechanical and electrical energy in a variety of environments. Nuclear fuels have much higher energy density than comparable chemical sources and are self contained, requiring no exchange of reactants or exhaust with the external world. These characteristics render nuclear power particularly effective for submarines and spacecraft which share a requirement for compact long lived power sources that can operate relatively independently from the environment.

The power conversion system which transforms reactor heat input into electrical power output is a key component in space reactor power system design. The efficiency with which this system operates strongly affects overall system performance and reliability. Space reactors have traditionally relied on low efficiency static power conversion technologies, such as thermophotovoltaics, with long life and reliability because maintenance is typically impractical. Terrestrial reactors use less reliable but more efficient dynamic systems, such as turbines. An ideal power conversion system would combine the efficiency of a dynamic system with the reliability of a static one.

Photovoltaic cells have a long history of power conversion applications in spacecraft. These cells are static power conversion devices that convert incident light into electrical power. Advances in semiconductor crystal manufacturing have led to thermophotovoltaic cells which convert incident infrared radiation directly into electricity. This thesis attempts to assess their utility for space nuclear reactor power system application.

Performing an assessment of a developmental technology for an advanced application is fraught with danger. This thesis contains academic advice on reactor plant design and it is wise to remember the words of ADM Hyman G. Rickover, the first Director of Naval Nuclear Propulsion.

> An academic reactor or reactor plant almost always has the following basic characteristics: 1) It is simple. 2) It is small. 3) It is cheap. 4) It is light. 5) It can be built very quickly. 6) It is very flexible in purpose. 7) Very little development is required. It will use mostly off-the-shelf

components. 8) The reactor is in the study phase. It is not being built now.
[Ref. 1]

The present work proceeds, with the Admiral's warning in mind, to outline the reasons why space nuclear power systems are desired and to describe their constituent components in Chapter II. Chapters III and IV contain an introduction to thermophotovoltaics and the present state of the art in that technology. Chapter V describes a simple assessment of the engineering tradeoffs involved in using state of the art thermophotovoltaics in a 100 kilowatt class space nuclear reactor power system. This assessment is followed in Chapter VI by predictions of the benefits which further technology development might bring. The assessment contained in this thesis is, in the final analysis, only preliminary. Chapter VII concludes by identifying areas where future work is required.

II.   SPACE NUCLEAR POWER

Major advances in any given technology are costly in time, money and other resources. The motivation that drives the development of new space fission reactor power sources is the subject of the first section below. Subsequent sections describe the subsystems necessary for a space nuclear reactor power system (SNRPS). It should be noted that many different acronyms appear in the literature and there are multiple types of nuclear power systems. SNRPS are defined in this present work as power plants designed primarily to convert the heat of a nuclear fission reaction into electrical power in a space environment. They are to be contrasted with nuclear thermal rockets which use the heat from a nuclear fission reactor to heat propellant to provide rocket thrust and radioisotope thermal generators which convert the heat from radioactive decay into electrical power. These two technologies, while more mature than SNRPS, are not the subject of the current work.

A.   WHY SPACE NUCLEAR POWER?

Experience since the dawn of the Space Age indicates a general upward trend in spacecraft power requirements. Nowhere is this trend more evident than in exploratory spacecraft; compare the Mars Sojourner Rover's 16 watt solar power system to the Mars Expedition Rovers' 140 watts [Refs. 2 and 3]. The trend continues as NASA requires an approximately 100 kWe power system for the Jupiter Icy Moons Orbiter (JIMO) scheduled for launch no earlier than 2011. A successful JIMO program will be the first time U.S. science goals have driven a mission to use an operational nuclear reactor in space. An understanding of why 100 kWe is required for this mission and why alternative technologies are unable to meet the power requirements answers the question posed at the beginning of this section.

JIMO power requirements are based on needs for electric propulsion to increase the number of science targets visited, active sensors that previous spacecraft have been unable to employ at Jupiter and large bandwidth communications to return the data to Earth in a timely manner [Ref. 4]. The benefits in any of these areas are considerable but the utility of high power electric propulsion deserves special mention because it is the best single reason for higher onboard powers. Chemical propulsion works by burning

3

fuels in a reaction chamber and exhausting the products out of a nozzle. The fuel acts as both a source of energy and as the reaction mass to achieve rocket thrust through conservation of momentum. Electric propulsion, in contrast, works by using electrical power from the spacecraft's power system to accelerate an inert propellant. The advantage of this technique is that it permits much higher propellant exhaust velocities than chemical propulsion. This can result in using less mass to achieve the same change in spacecraft velocity thereby freeing up more spacecraft mass for payload. The tradeoff is that electrical propulsion systems typically have lower thrust to weight ratios than their chemical cousins. This makes their trip times sensitive to the local gravity field and propulsion selection dependent on where the system will be used. Electric propulsion performs very well in heliocentric space far outside of the sphere of influence of a planet where it runs for long times to build up velocity changes slowly. Electric propulsion can generally get more payload mass to a distant destination faster than chemical propulsion as long as the power source has sufficient life and power density [Ref. 5].

Higher powers clearly have promise. It is still reasonable to question the need for nuclear technology since solar power has been sufficient for most (though not all) past space power needs. The near Earth space environment is flooded with power. The sun represents a 5800 K fusion powered blackbody source placed at the center of our solar system that provides about 1373 W/m^2 in Earth orbit at no development cost. A contemporary advanced solar panel is 24% efficient at converting the incident sunlight to electrical power, produces 330 W/m^2 in Earth orbit and masses 2.06 kg/m^2. The specific power, defined as the power output divided by the system mass of the solar array, is 160 W/kg [Ref. 6].

The specific power of a given solar array decreases as the solar flux decreases with distance from the sun illustrated below in Figure 1. Recall that electric propulsion systems are sought to increase payload mass and decrease trip times to distant solar system locations. NASA has often sent exploratory spacecraft to Mars and has sent several to Jupiter. The solar flux at Mars and Jupiter is, respectively, 45% and 2% of the Earth orbit value.
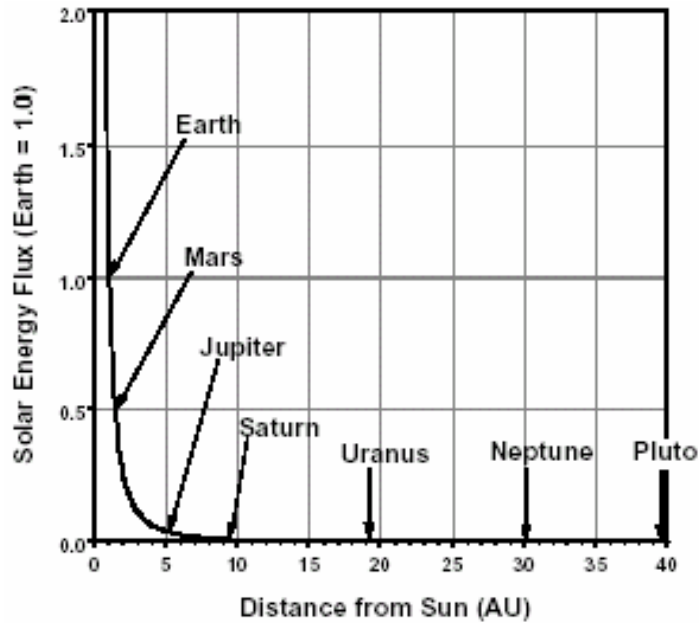
Figure 1.   Solar Flux Energy vs. Distance from the Sun [from Ref. 7, p. 4]

The solar array from our previous example has a specific power of 72 W/kg in Mars orbit and 3.2 W/kg at Jupiter. The diminishing amount of solar power is a problem when a mission is bound for a distant target and explains why none of NASA's probes to Jupiter or beyond have used solar power.

The sheer power level required for a mission may also make solar power unattractive, even in Earth orbit. The low specific mass of solar power must be balanced against the large structures required to collect kilowatts of power. For instance, it takes an array of 303 m^2 to provide 100 kWe in Earth orbit. These large arrays may be difficult or impossible to fit in current launch vehicles and may cause mass increase on other spacecraft subsystems such as attitude control. The United States has a long history of developing low power solutions to design problems but it is still possible that future spacecraft designers will desire higher powers in Earth orbit for active sensing, communications or directed energy applications. President Reagan's Strategic Defense Initiative generated a number of proposals for nuclear powered weapons, communications platforms, and sensor systems for instance [Ref. 8].

Alternative power generation approaches for various power levels appear below in Figure 2. This graph neglects fusion and antimatter reactions as well as experimentally

confirmed quantum zero point energy field fluctuations in favor of those technologies which have actually been used to provide power. The regions represent the general areas where the given energy sources can provide the indicated amount of power for a given period and are primarily determined by the energy density of the storage medium. Nuclear fission power appears to be the only technology able to offer higher power levels for long mission durations [Ref. 9, p. ix]. The increased power and operational lifetime possible with nuclear fission create new opportunities for those willing to pay the large costs of SNRPS development.
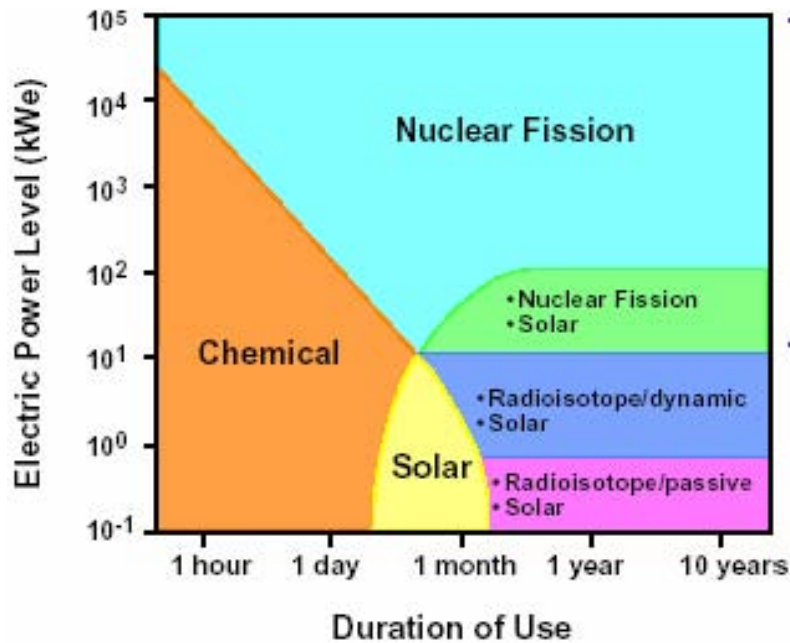
Figure 2.　Comparison of power sources based on power level and duration of use [from Ref. 7, p. 4]

B.   REACTOR

A generic SNRPS consists of the five basic components diagrammed below in Figure 3. This and subsequent sections describe the components in more detail.
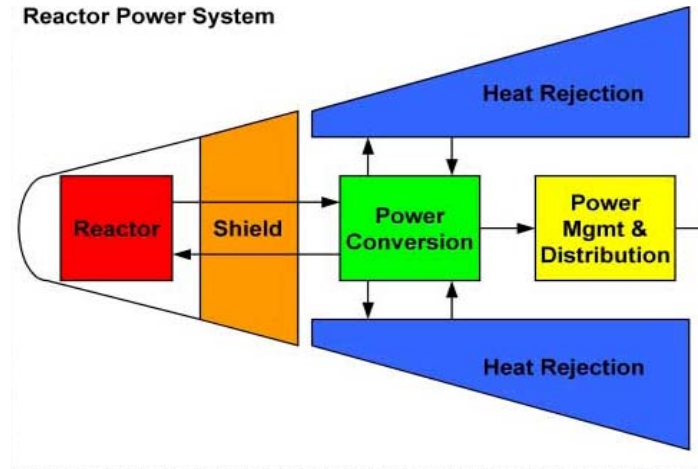
Figure 3.   Functional Block Diagram of a Space Reactor Power System after [Ref. 10, p. 1]

The reactor generates nuclear fission power, converts it to thermal power and passes it on for subsequent conversion into electrical power. A digression into the physics of nuclear fission provides qualitative insight into the choices facing a prospective SNRPS designer and justifies later assumptions made about this component.

Nuclear fission is the act of exciting a nucleus with a neutron and causing it to split. The fission reaction upon which nuclear reactors operate appears below in Figure 4.
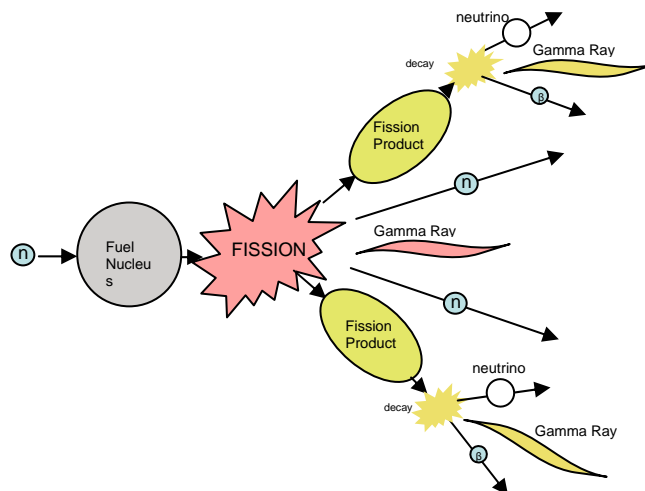
Figure 4.   Generic Fission Reaction

The figure illustrates several things which are important to a reactor designer. First, note the use of a neutron at the left side of the figure to provide the initial energy to encourage the fuel nucleus to split. The neutrons are necessary in order to create an unstable compound nucleus which subsequently splits into the various products diagrammed at the right of the figure. Second, the fission produces a cascade of particles. Each of these particles carries some of the energy liberated a time after the fission event and some of them are radioactively unstable themselves and decay a short time after fission, releasing additional energy. The energy distribution is important in determining how best to extract useful power from a reactor and it is primarily dependent on the choice of nuclear fuel nucleus.

Uranium-235 (U-235) is the fuel of choice for space reactors because it is relatively easy to control, is relatively stable with a 700,000,000 year half-life, and available in national stockpiles. The primary disadvantage of this fuel is that it is hard to obtain because most naturally occurring uranium is the 238 isotope with only 0.7204% being U-235. Space reactor fuel must be highly enriched in the U-235 isotope, that is, U-235 is approximately 93-95% by weight of the uranium in the fuel [Ref. 11, p. 55]. When U-235 splits, it can produce one of over 60 known pairs of fission products, each with an associated probability [Ref. 12, p.107]. A sample U-235 fission reaction is shown below.

$$_0n^1 + {}_{92}U^{235} \rightarrow {}_{36}Kr^{91} + {}_{56}Ba^{143} + 2\,_0n^1 \tag{1}$$
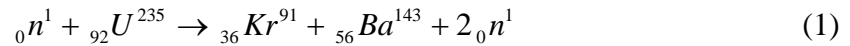
The typical energy distribution from the U-235 fission reaction is shown below in Table 1. The Mega electron-Volt (MeV) unit of energy is common to nuclear physics and is the kinetic energy of an electron accelerated through a million volt potential difference. It is approximately 1.6×10^{-19} J. Chemical reaction energies are typically measured in electron Volts (eV), by comparison, demonstrating why it is said that nuclear fuels are a million times more energetic than chemical fuels. Table 1 contains an average of fission product energies over all of the possible fission products.

Form of Energy	Energy Released (MeV)	Energy Recoverable (MeV)
Kinetic- Fission Products	168	168
Fission Product Decay	27(12 in neutrinos)	15
Fission Gamma Radiation	7	7
Kinetic-Fission Neutrons	5	5
Totals	207	195

Table 1.   Typical Energy Distribution for U-235 Fission after [Ref. 9, p. 37]

The majority (86%) of the energy liberated appears as the kinetic energy of the fission products. These products will only travel a short way inside the reactor and they will transfer their energies into random particle motion as they slow down inside the material that immediately surrounds the site of their birth. That is to say, most of the energy of the fission products is rapidly turned into heat in the fuel and this is the thermal power that the reactor passes to the rest of the system for conversion to electricity. The fission products might deposit their energy locally but the other reaction products may not be so well behaved. Neutrinos interact weakly with matter and leave the reactor, representing the first of many energy losses in the system. Gamma radiation is more interactive than the emitted neutrinos. This is both a blessing and a curse to the designer. The energy of the gamma rays is not necessarily lost and subsequently become thermal output of the core. However, it is impractical to provide enough dense shielding to stop all of the gammas inside the reactor where they can be converted to heat. Some always leak out of the core, making external radiation shielding a necessity to protect sensitive crew or equipment. Overall, a nuclear fission event releases around 195 MeV of usable energy, making the energy density of pure U-235 approximately 8.2×10^{13} J/kg. Again, compare this to 1.35×10^7 J/kg from chemical fuels (hydrogen and oxygen) and nuclear fuel's appeal for space applications becomes clear [Ref. 13, pg. 3].

The neutrons released in fission are necessary to sustain and control the reaction. Every fission event must produce at least one new neutron which survives to perpetuate itself. Such a reaction is called "self sustaining". The fission of U-235 creates about 2.5 neutrons on average. An average value is necessary because the fission reaction can

produce about 60 different sets of reaction products each of which produce variable numbers of neutrons [Ref. 12, p. 107]. 2.5 neutrons would appear to be more than enough to create a self sustaining reaction but the situation is complicated by the energy of the neutrons produced, the fact that some neutrons always leak out of a finite reactor and the necessary presence of materials other than fuel. These combine to ensure that significant numbers of the neutrons produced do not go on to produce new fission events but are lost from the reactor.

The spectrum of neutron energies which result from the fission process is also variable and is given by the empirical formula below [Ref. 9, p. 38].

$$N(E) = 0.453e^{-\frac{E}{0.965}} \sinh(\sqrt{2.29E}) \tag{2}$$

Here, E is the energy in MeV and N(E) is the fraction of fission neutrons which have energy E per unit energy range. A plot of this function appears below in Figure 5.
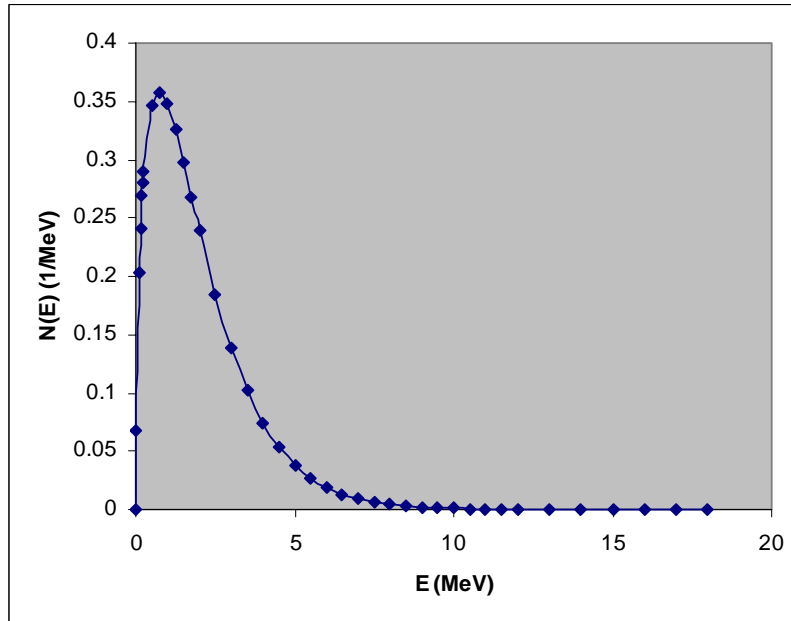
Figure 5.   Fission Neutron Energy Spectrum for U-235

The graph shows that most fission neutrons are born with energies around 0.75 MeV. Neutrons can be divided into two groups based on their energies: fast and thermal. Thermal neutrons are in thermal equilibrium with the surrounding matter. Practically, this means that they have energies on the order of 10^{-5} MeV. Most fission neutrons are born

fast, however and have energies above 10^{-3} MeV [Ref. 12, p. 110]. The important distinction between the two groups is that a U-235 nucleus is approximately 200 times more likely to undergo fission when struck by a thermal neutron than a fast one.

Nuclear reactors are classified according to which group of neutrons they rely on to cause fissions. A fast reactor relies on the fast neutrons that are emitted directly from the fission process itself to go on and cause other fissions. A thermal reactor contains some material, called a moderator, to slow fast neutrons down to thermal speeds in order to cause fissions. The tradeoff here is that fast reactors require more U-235 molecules in them than thermal reactors but do not require any moderator. Actual trade studies require extensive calculation and are beyond the scope of this introduction but the general consensus in the space nuclear power community is that fast reactors are generally smaller and lighter for a given power than thermal reactors [Ref. 11, pp. 47-49].

This is enough information to conceptually examine a nuclear reactor for space applications. A schematic is shown below in Figure 6.
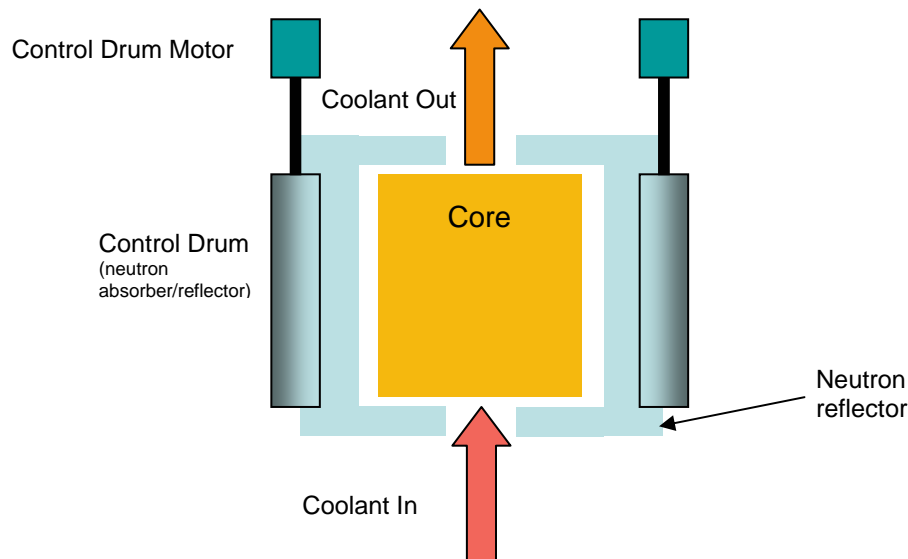
Figure 6.   Generic Space Reactor Schematic Diagram

The core consists of a quantity of highly enriched uranium-235 packaged in a suitable form known as a fuel element. These elements are fabricated from high temperature structural materials to ensure that the precisely determined shape of the core is maintained during thermal expansion and contraction as the reactor changes temperature.

The core is wrapped in a neutron reflector, such as beryllium, which is used to reflect some fraction of the neutrons that escape from the core back in to it so that they are not lost. Movable control drums surround the core serving as selectable neutron absorbers or reflectors. The reflector side acts like the rest of the static neutron reflector: increasing the number of neutrons available for fission in the core. The absorbing side is made of a material which is good at absorbing neutrons, like boron-carbide (B_4C). Exposing the core to this side of the control drum allows neutrons to escape until the fission reaction is no longer self sustaining and the rate of fission drops. The final element in the figure is the coolant that takes the thermal power from the fuel elements and moves it to the electrical conversion equipment. Many different types of coolant are possible; liquid metals have historically been used in US and Russian SNRPS [Ref. 9, p. 36].

Nuclear fission occurs in the fuel elements and they are consequently the hottest elements of the system. We will see later that higher temperatures mean higher efficiencies so the system's overall performance is largely dependent upon the material properties of the fuel elements. The complexities of nuclear fuel material engineering are beyond the scope of the present work, but an overview of the potential fuel forms indicates expected temperature ranges for later analysis.

Fuel elements are required to contain sufficient inventory of fissile fuel to run the reactor, maintain the proper shape of the core, transfer heat to the coolant, contain fission products and do so reliably for the design life of the core. This represents a challenging set of material properties including high creep resistance, thermal conductivity, radiation resistance, thermo-chemical compatibility with other reactor materials, and high strength. Metallic uranium alone is generally unsuitable as a fuel element due to its relatively low melting temperature (1405 K) and chemical reactivity with practically all metals. Uranium is therefore combined with other materials in fuel elements. Zirconium, zirconium hydride, oxides, carbides and nitrides have all been used or proposed for space reactors [Ref. 12, pp. 153-155]. Table 2 below gives a listing of fuel materials, the space reactor program that they were associated with, their flight status, and the operating temperature of the fuel in the proposed application.

Fuel Material	Associated Reactor Program	Flight Status (Duration)	Outlet Temperature	Reference
U-O$_2$	TOPAZ	32 spacecraft flown	873 K	Ref. 14
U-ZrH	SNAP-10A	1 spacecraft flown (43 days)	785 K	Ref. 9
U-ZrH	SNAP-8	nuclear system ground tests (1 year)	920 K	Ref. 9
U-C$_2$	NERVA (PEWEE)	full nuclear system ground tests(40 min.)	2550 K	Ref. 9
U-ZrH	SNAP-2	full nuclear ground tests(max 2800 hr)	920 K	Ref. 9
U-N	SP-100	nuclear/non-nuclear component ground tests	1375 K	Ref. 15
U-N/U-C	SNAP-50	nuclear/non-nuclear component testing (1690 hrs)	1400 K	Ref. 9
U-O$_2$	710 Advanced High Temperature Reactor	nuclear/non-nuclear fuel element testing (7084 hrs)	1920 K	Ref. 5

Table 2.   Fuel Forms from Previous Space Reactor Programs

Table 2 shows a broad range of reactor core temperatures from roughly 800 to 2000 K. Note that the highest temperature (2550 K by the Pewee reactor) was for a nuclear thermal rocket application and has the shortest duration (40 min) listed. This indicates a general trend in reactor design; hot reactors don't last as long. SNRPS are designed to provide electric power consistently for long periods of time (~ years) and therefore higher temperatures are undesirable from the reactor standpoint.

C.   RADIATION SHIELD

Nuclear reactors produce radiation that cannot practically be contained by the reactor itself. Neutrino, gamma and neutron radiations inevitably leak out of the core and the last two can prove harmful to spacecraft components or personnel. A variety of shielding configurations have been proposed for SNRPS use based on a tradeoff between the amount of exposure tolerable by the payload and shield mass. The various geometries are shown schematically below in Figure 7.   Note that the control drive motors are outside the shield to indicate the need to protect sensitive control electronics. Only the shadow shield configuration has been flown because it minimizes the overall shield mass required. It has the drawback of leaving a large portion of the core unshielded. The right side of the figure shows how a separation boom can be used to further reduce the intensity of harmful radiation at sensitive components by increasing the distance between them and the reactor.
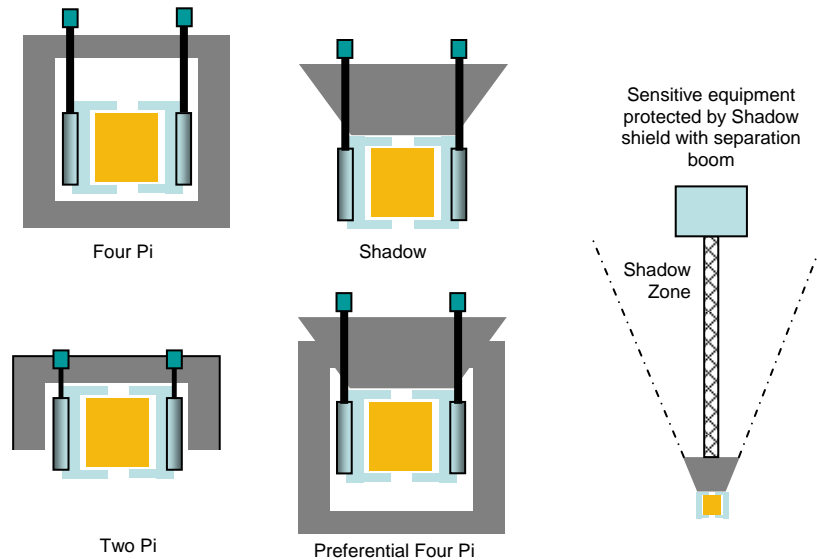
Figure 7.   Flown or Proposed SNRPS Shield Geometries

Tungsten (W) and lithium-hydride (LiH) are the most commonly chosen shielding materials for SNRPS [Ref. 12, p. 376]. Each is selected to deal with different radiation. Tungsten is used to stop gamma rays and lithium hydride for fast neutron shielding. These materials are arranged as shown below in Figure 8. Note that the penetrations for

14

the control drums can create unshielded zones which need further engineering or operational measures to safeguard against.
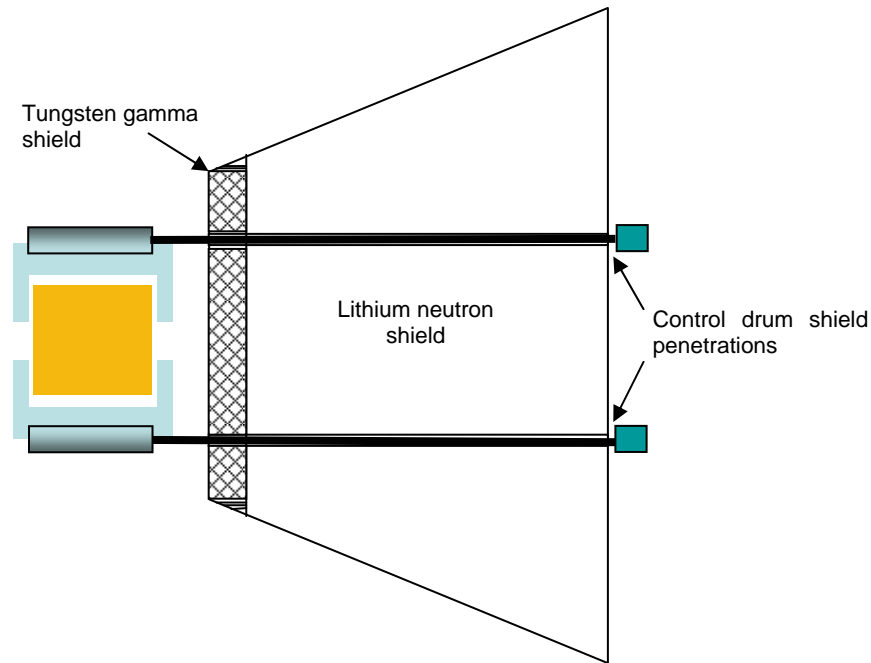
Figure 8. Typical Shadow Shield Schematic Diagram

The order of material in a radiation shield is significant. A dense tungsten gamma ray shield comes first to attenuate gamma radiation that might otherwise go into heating the lithium-hydride neutron shield. The excellent thermal properties of tungsten are compared to those of lithium hydride below in Table 3.

Material	Tungsten	Lithium-hydride
Thermal Conductivity (W/m^2 K)	132	4.6
Melting Point (K)	3653	960

Table 3. Thermal Properties of tungsten and lithium-hydride from [Ref. 11, pp. 66-69]

Tungsten is better suited to disposing of the large amounts of heat resulting from radiation absorption than lithium-hydride. The thickness difference shown in the shield

diagram above is because neutrons progressively slow down through collisions with nuclei as they pass through the lithium-hydride shield, whereas gamma radiation attenuation occurs much more rapidly in the dense tungsten. The lithium shielding is typically encased in another metal for structural strength as shown in the photograph of the Space Nuclear Auxiliary Power 10A (SNAP-10A) flight test model below in Figure 9.
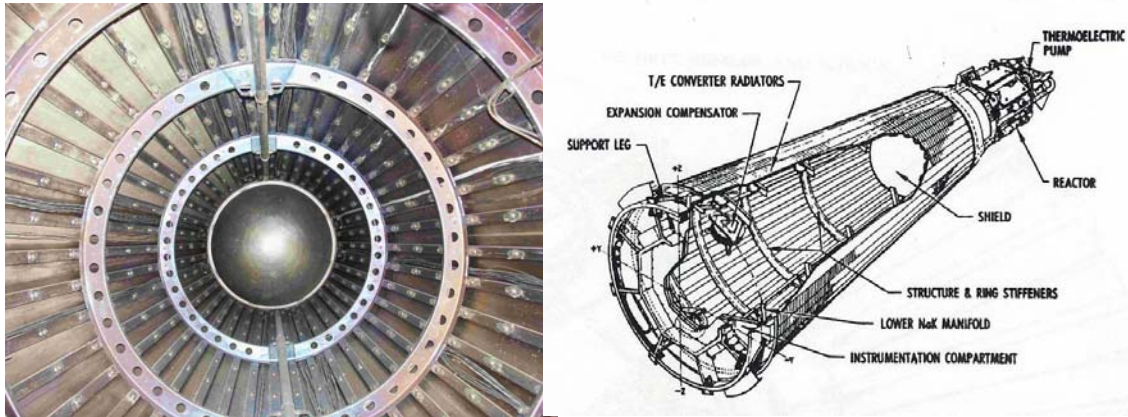
Figure 9.   SNAP 10A Radiation Shield. Photo by Author. Diagram after [Ref. 9, p. 164]

Radiation shielding is typically massive due to the density of the tungsten and the thickness of lithium hydride necessary for fast neutron absorption. The shield is often a significant factor in overall SNRPS mass. Larger volume cores mean larger shielding areas which are even more massive. Higher reactor powers lead to larger fission rates and this means more radiation coming out of the core again leading to more massive shields. These system interactions are complex and methods to economize the required shielding have occupied entire textbooks. The design of such shields is usually dependent upon statistical radiation interaction codes and painstaking trade studies. Simple empirically derived formulae relating shield mass and reactor thermal power exist and will be used to estimate shield mass in later sections.

D.   POWER CONVERSION

The reactor produces thermal power while thrusters and various spacecraft components require electrical power. The power conversion subsystem converts the thermal power from the reactor into electrical power for onboard devices. The variety of power conversion technologies that have been proposed, examined, or actually used in space nuclear power plants defies concise description. They are generally separated into two distinct classes called static and dynamic. Static power conversion systems convert thermal to electrical power directly without moving parts. Dynamic power conversion systems use rotating or reciprocating machinery. This section describes the general considerations facing a system designer in choosing a power conversion technology, the thermodynamic theory of power conversion efficiency, and concludes with some generalizations about the expected performance of the two different classes of systems.

The present work is primarily concerned with the efficiency of thermophotovoltaic power conversion technology and will not attempt to definitively describe the numerous alternatives. Readers interested in details of particular technologies are directed to excellent summaries with a space nuclear focus in [Ref. 9], [Ref. 18] or the proceedings of the annual Space Technology and Applications International Forum (STAIF) in Albuquerque, NM. A complete gas turbine power system design concept for NASA's JIMO mission also appears in [Ref. 10]. Historically, space nuclear power systems such as U.S. radioisotope thermal generators or Russian TOPAZ nuclear fission reactors have relied exclusively upon static conversion technologies. A high level description of a static space reactor power system employing one of these direct electric conversion technologies can be found in [Ref. 12].

The choice of power conversion apparatus has repercussions throughout the system and the designer must balance a number of conflicting influences. The designer must consider efficiency, mass, operating temperature, reliability, vibration, torque disturbance, output power characteristics, and modularity. Efficiency is the primary focus here and will be described in its own section. Other considerations affecting power conversion system selection are briefly described afterwards to illustrate the problems facing a SNRPS designer.

1.   Efficiency

The primary figure of merit for a power conversion system in the present work is its efficiency. Much of the subsequent work is intimately concerned with the effect of varying efficiency on overall power system mass. This section deals with the general thermodynamic theory involved in converting heat into useful work and then goes on to discuss system level design considerations for SNRPS application. There are many different types of efficiency defined in the literature. In simple terms:

$$efficiency \equiv \frac{\text{desired useful work}}{\text{energy expended to obtain that work}} \tag{3}$$

Different definitions of "useful work" and "energy expended" can dramatically vary the reported efficiency of a power conversion process. The literature on this topic is often vague as to the exact definition used in a given calculation. Different communities are interested in different measures of device effectiveness. The nuclear spacecraft engineer will probably make use of several different efficiencies to describe the power flow within a SNRPS. The reactor efficiency, η_{Rx}, is defined as the amount of reactor fission power that is transformed into thermal power by the reactor. The primary losses at this stage are neutrinos, neutrons and gamma rays, some or all of which escape the core and are not converted into thermal power. The transfer efficiency, η_{trans}, is defined as the fraction of reactor thermal power that is transferred to the power conversion system. Losses in this area include thermal radiation from coolant piping to space and conduction to spacecraft structure. These possibilities appear below in Figure 10.
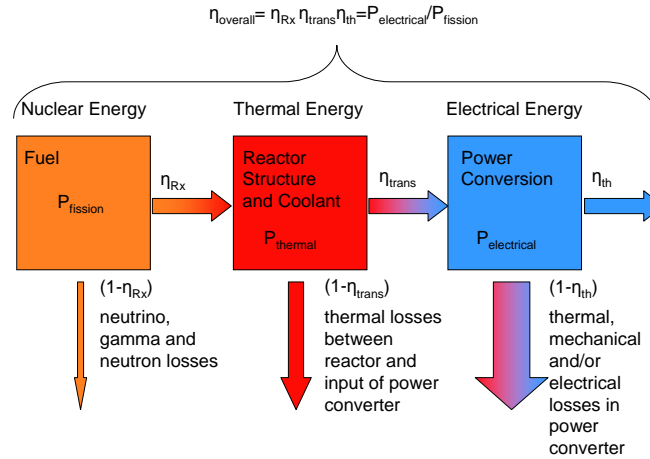
Figure 10.   Energy Conversion Processes and Efficiencies

The major figure of merit for power conversion systems in the present work is labeled thermal efficiency and is defined below. It should be noted that this is the author's terminology and that no standard appears in the literature.

$$\eta_{th} = \frac{P_{elec}}{\dot{Q}_{input}} \tag{4}$$

P_{elec} is the electrical power output to the spacecraft bus at the power conversion system terminals. $\dot{Q}_{input}$ is the thermal power input to the power conversion system. Note that this definition ignores losses in the conversion of stored nuclear energy into random kinetic energy of the reactor system and also neglects heat losses as the heat is sent to the power conversion subsystem.

It is useful to review the theoretical efficiency bounds of conversion from thermal energy to useful work. The laws of thermodynamics provide an upper bound on the performance to be expected from a given power conversion approach. The limit was first developed by Sadi Carnot in 1824 while working on heat engines for the French military. Heat engines convert thermal energy into useful mechanical work. The steam engine is an example. The reversible heat engine is an idealized case in which the total entropy of the system remains constant throughout the process. The input thermal energy to the device must be greater than the amount of useful work extracted due to the second law of thermodynamics.

The entropy and energy flows in a reversible heat engine are schematically diagrammed below in Figure 11.
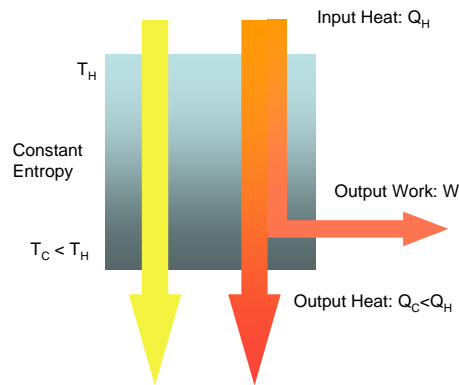
Figure 11.   Conceptual Diagram of a Reversible Heat Engine

A reasonable question is: why can't all of the input heat be converter to work? The answer rests upon a three concepts from fundamental thermodynamics. Work and heat are two forms of energy transfer. Work (W) transfers energy out of a system by changing the external physical parameters that describe it such as pressure, volume, number of particles or voltage. Heat (Q) transfers energy by thermal contact between bodies at different temperatures. But the energy is not the only physical quantity moving through the heat engine. The difference between work and heat lies in the way that entropy (S) is transferred. Recall from thermodynamics that entropy is a measure of the level of disorder in a system. Work is an ordered process. Heat is a massed average of random particle motion. Heat transfers entropy but work cannot. The reason the heat engine cannot completely convert input heat to work is that some heat must remain in the system to carry away the entropy which is required to be conserved or increase by the laws of thermodynamics [Ref. 17, pp. 227-230].

Practical heat engines never match the performance of theoretical simplification because of losses to friction, electrical resistance and other irreversible processes. The efficiency of a reversible engine thus provides an upper limit fixed by physics on the power conversion efficiency of any device which transforms heat into useful work and a performance target for a SNRPS design to aim for. Carnot demonstrated that the Carnot efficiency for an engine which operated between a high temperature reservoir of thermal energy and a lower temperature reservoir is strictly a function of the reservoir temperatures, T_H and T_C.

$$\eta_C \equiv \frac{W}{Q} = \frac{T_H - T_C}{T_H} \tag{5}$$

η_C must be less than one due to conservation of energy holds true. It also cannot be equal to one unless $T_C \to 0$ which ensures that the second law of thermodynamics is not violated [Ref. 17, pp. 240-241].

The Carnot efficiency shows the maximum values that we might expect for our thermal efficiency figure of merit. Practical thermal efficiencies are always less than the Carnot predicted values due to irreversible system losses. For this reason, it is common to see system thermal efficiencies expressed as a fraction of Carnot efficiency. A plot of

20

Carnot efficiency vs. hot reservoir temperature for three different cold reservoir temperatures appears below in Figure 12.
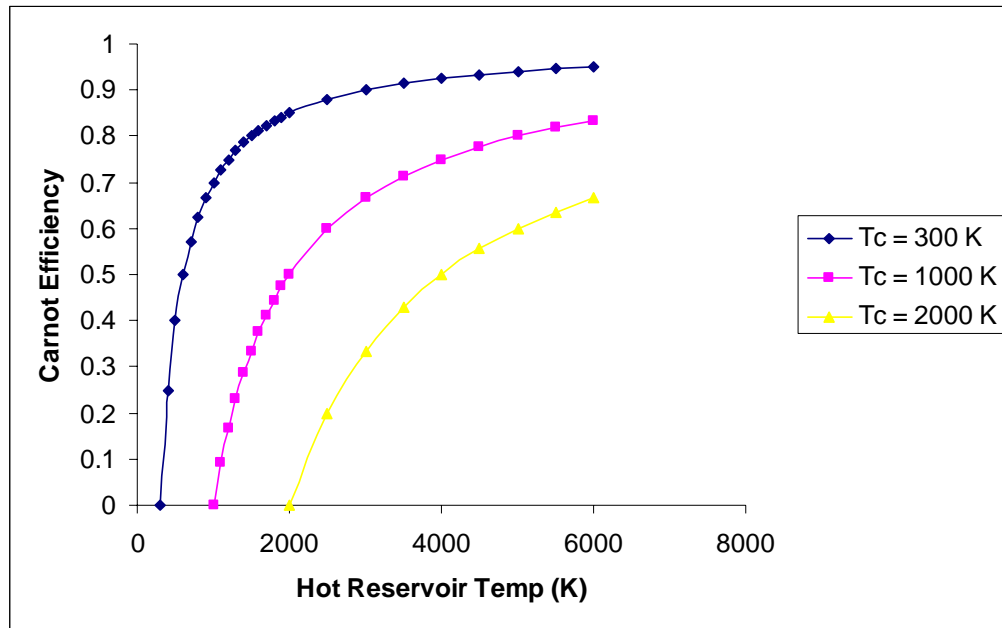
Figure 12.   Plot of Carnot Efficiency vs. Hot Reservoir Temperature for Three Cold Reservoir Temperatures

Two important conclusions can be drawn that define the trade space considered in this thesis. The first is that the efficiency at a fixed cold reservoir temperature increases rapidly with hot reservoir temperature. This drives reactor temperatures to higher values that require expensive material development. The second trend is that raising the cold leg temperature decreases Carnot efficiency. These two trends together define a fundamental problem for the SNRPS designer: use a developmental high temperature reactor heat source and high efficiency power conversion equipment so that the radiator mass is minimized or a lower temperature reactor with the lower conversion efficiency and larger radiator masses.

2.   Other Design Considerations

There are many other factors which drive power conversion subsystem analysis.

a. Mass

Component mass drives space vehicle mass and directly impacts launch costs. Mass minimization is particularly important in nuclear powered spacecraft because the power systems are expected to dominate vehicle mass. The power conversion subsystem has a mass of its own but also strongly drives overall SNRPS mass through the efficiency. Overall power system mass is the primary figure of merit in this thesis.

b. Operating Temperatures

The two temperatures of concern are the heat source temperature, T_H, and the heat rejection temperature, T_C. Lower heat source temperatures decrease efficiency, stress reactor materials less, and increase operational lifetimes. Higher heat source temperatures may require more extensive (and expensive) reactor development. Historically speaking, increasing the heat source temperature has resulted in the creation of more problems than solutions. A more conservative choice of heat source temperatures in early programs coupled with a power conversion approach that can evolve to higher temperatures appears to be a more beneficial approach. The present work fixes heat source temperature and varies rejection temperature. [Ref. 18, p.IV-282]

Heat rejection temperature drives overall power conversion system efficiency by affecting Carnot efficiency as previously described. It also affects overall system mass by driving the required heat rejection radiator area as described in the next section. Generally speaking, low heat rejection temperatures increase power conversion system efficiency but also drive up system mass due to larger radiators. An intermediate heat rejection temperature will usually lead to an optimum overall system mass and this is largely the subject of the present work. [Ref. 18, p.IV-283]

c. Reliability

Space nuclear reactor power systems must be reliable because maintenance will be essentially impossible for the foreseeable future. A number of factors influence reliability such as number of moving parts, temperatures, and system complexity. Selection of components with low failure rates and installation of redundant components are the primary means to ensure reliability. Redundancy penalizes the designer by adding complexity, cost, and mass to the system. Improving component failure rates typically means higher cost components. Static power conversion systems

are generally assumed to be more reliable than dynamic ones by virtue of having no moving parts. [Ref. 18, pp. IV-281-282]

d. *Output Power Characteristics*

The major electrical loads on future nuclear spacecraft are likely to require large quantities (~100 kWe) of high voltage DC power. High DC voltages are desirable from a power transmission standpoint because they minimize current and I^2R losses in transmission lines. Unfortunately DC power can impose extra mass penalties upon many power conversion apparatus, such as rotating machinery, because the output power is AC and extra equipment is required for AC-DC conversion. Static power conversion apparatus output DC without any special efforts on the designer's part.

e. *Vibration and Torque*

Vibration from moving parts in the power conversion system can complicate the precision pointing required by many spacecraft. Rotating power conversion machinery can also produce torques that effect attitude control. These vibrations and torques can be cancelled by mounting redundant machines in opposed pairs but the cost of this solution imposes limits on the power system design. Static conversion approaches obviously do no impose these constraints. [Ref. 18, p. 284]

f. *Modularity*

Modular power conversion apparatus provide partial redundancy and ensure graceful failure of the power system. They also provide the designer with more options in system arrangement and the potential to scale to higher or lower powers as technology advances or requirements change. [Ref. 18, p. IV-284]

3. Power Conversion Options

An exhaustive listing of the efficiencies practical with various power conversion technologies is properly the subject of a textbook. The table below lists predicted efficiencies for a variety of power conversion systems common in the literature. These predicted thermal efficiencies contain substantial uncertainty as they are the result of technology projections from an industry study in [Ref. 18].

Power Conversion Technology	η_C (%)	η_{th} (%)	T_H (K)	T_C (K)
Thermoelectric	55	9	1273	573
TOPAZ II In Core Thermionic	56	5	1873	825
Out Of Core Thermionic	51	13-14	1800	880
Advanced Gas Turbine (Brayton Cycle)	67	32-35	1300	425
2 Phase Turbine-Condenser (Rankine Cycle)	28	14-15	1380	1000
Reciprocating Machinery (Stirling Cycle)	57	40	978	422

Table 4.   Predicted Thermal Efficiency of Representative Power Conversion Systems Assuming 100 kWe System [Ref. 18]

This table highlights general characteristics of the two classes of power conversion systems. Static systems (thermoelectric and thermionic) convert heat into electrical energy with no moving parts but generally have low thermal efficiency and require high temperatures. Dynamic systems (turbines and reciprocating machinery) are familiar from terrestrial application and have higher thermal efficiencies than static systems but are perceived by some to reduce overall system reliability by introducing moving parts. The ideal power conversion system would combine the high efficiency of a dynamic technology with the reliability advantages of a static one.

E.   HEAT REJECTION

Heat rejection equipment can take up a significant fraction of the overall spacecraft mass. This final component of a SNRPS must remove the waste heat from the power converter. This is crucial to avoid exceeding temperature limits and causing component damage. Rejecting heat in space is particularly difficult. Basic physics dictates that heat can be transferred by conduction between two bodies in thermal contact, convection within a fluid or radiation to the environment. A spacecraft operating in a vacuum must rely exclusively on radiation to reject heat. The thermal control issues considered in this thesis are those of heat rejection because the rejection equipment is the

dominant portion of the thermal control system mass at the higher powers attainable by SNRPS. This section introduces the principles of heat rejection, briefly discusses the space heat sink, covers the state of the art in heat rejection technology for spacecraft applications, and introduces the reader to the heat pipe radiator after a brief introduction to heat pipe theory.

1.   Radiator Theory

It is useful to discuss the perfect blackbody as the ideal absorber and emitter of photonic radiation. The blackbody is a theoretical construction which absorbs all incident radiation. It follows that the blackbody is also the perfect emitter. This means that no body at the same temperature can emit more radiation at any wavelength or in any direction. The spectrum of such an ideal radiator at a given temperature, T_{rad}, was first theoretically determined by Max Planck who originated quantum theory in the process. The spectral radiant exitance has units of W/m^2-micron and the spectrum is given below in (6).

$$M_\lambda\left(\lambda, T_{rad}\right) = \frac{2\pi hc^2}{\lambda^5}\left(\frac{1}{e^{\frac{hc}{\lambda k T_{rad}}} - 1}\right) \tag{6}$$

Where h is Planck's constant (6.626x10^{-34} J s), c is the speed of light in a vacuum (2.998x10^8 m/s), λ is the wavelength of radiation in meters, k is Boltzmann's constant (1.3805x10^{-23} J/K), and T$_{rad}$ is the average radiator temperature in Kelvin [Ref. 19, p. 15]. A graph of blackbody radiation at various temperatures appears below in Figure 13.
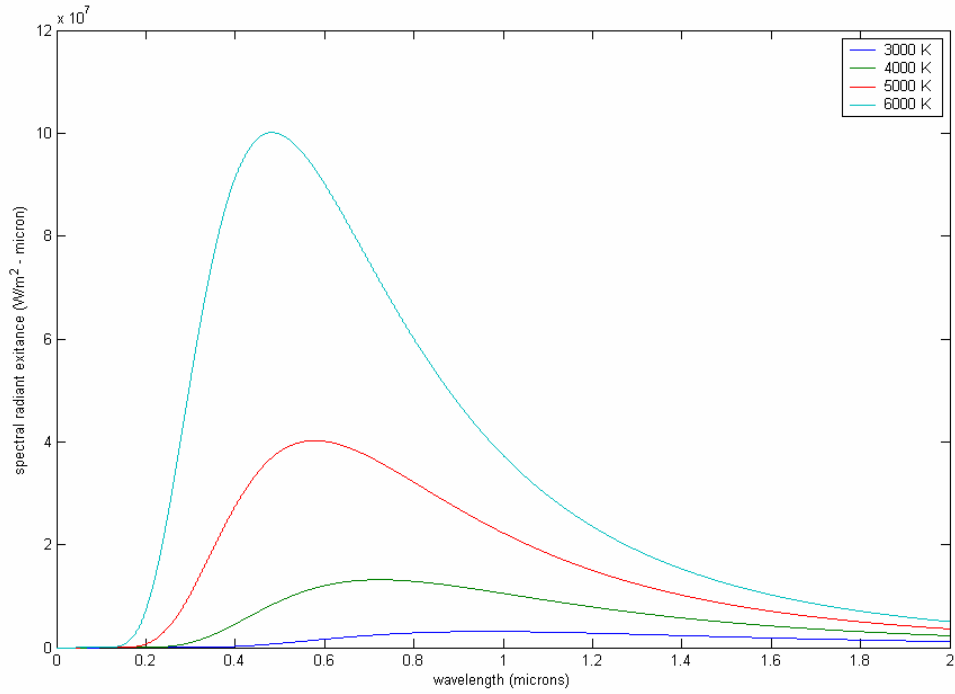
Figure 13.   Blackbody Spectra at 3000, 4000, 5000, and 6000 K

The impact of the fourth power temperature dependence is clear from the large differences between curves. Note that the sun's spectrum is roughly analogous to the 6000K blackbody shown above. The area under each of the curves is the total amount of power that the surface is radiating per square meter at the given temperature and is known as the total radiant exitance. The integral over wavelength of (5) has an analytic solution known as the Stefan-Boltzmann Law and is called simply the radiant exitance of the surface.

$$M = \sigma_{SB} T_{rad}^4 \tag{7}$$

Where σ_{SB} is the Stefan-Boltzmann constant (5.669 x 10^{-8} W m^{-2} K^{-4}) and T$_{rad}$ is again the average radiator temperature in Kelvin. Real radiators fall short of the blackbody ideal but the concept still has practical application. The radiant exitance of real radiators can be compared a blackbody at the same temperature and the ratio is known as the emissivity. The emissivity, ε, is defined below in (8).

26

$$\varepsilon(\lambda) = \frac{M(\lambda)}{M_{bb}(\lambda)} \tag{8}$$

Where $M(\lambda)$ is the radiant exitance of the actual body at a given temperature and wavelength and $M_{bb}(\lambda)$ is the radiant exitance of a blackbody at the same temperature and wavelength. Note that emissivity is often a function of the wavelength, temperature, viewing angle and a host of other properties. Fortunately, many radiators can be approximated as having constant emissivity. Emissivity is then given by (9) below.

$$\varepsilon = \frac{M}{M_{bb}} \tag{9}$$

Radiators that follow (9) are called graybody radiators and they include those used for SNRPS. All thermal radiation in this thesis is assumed to be from graybody radiators.

The Stefan-Boltzmann Law gives the rate of energy transfer out of a unit area of surface. The heat emitted can be found by combining the graybody Stefan-Boltzmann law with the area of the radiator(A_{rad}) and a view factor (F) to account for the fraction of the radiator that has a clear view of open space. This relationship is shown below.

$$\dot{Q}_{rad} = A_{rad} F \varepsilon \sigma_{SB} T_{rad}^4 \tag{10}$$

$\dot{Q}_{rad}$ is the emitted heat leaving the surface in W m^{-2} [Ref. 20, p. 3].

Radiative heat transfer is like other forms of heat transfer in that the radiating object eventually winds up in thermal equilibrium with its environmental heat sink. If the environment is above absolute zero, the rate of heat transfer will be less than given in (10). Space is not at absolute zero. The solar system is dominated by the sun and even interstellar space has a relatively constant 3 K sink temperature. The worst-case environmental sink temperature occurs when the radiator is normal to the incident solar radiation. A slightly more realistic case for the present purpose is a 25 degree angle of incidence and the resultant sink temperatures at various solar system bodies appear below in Figure 14.
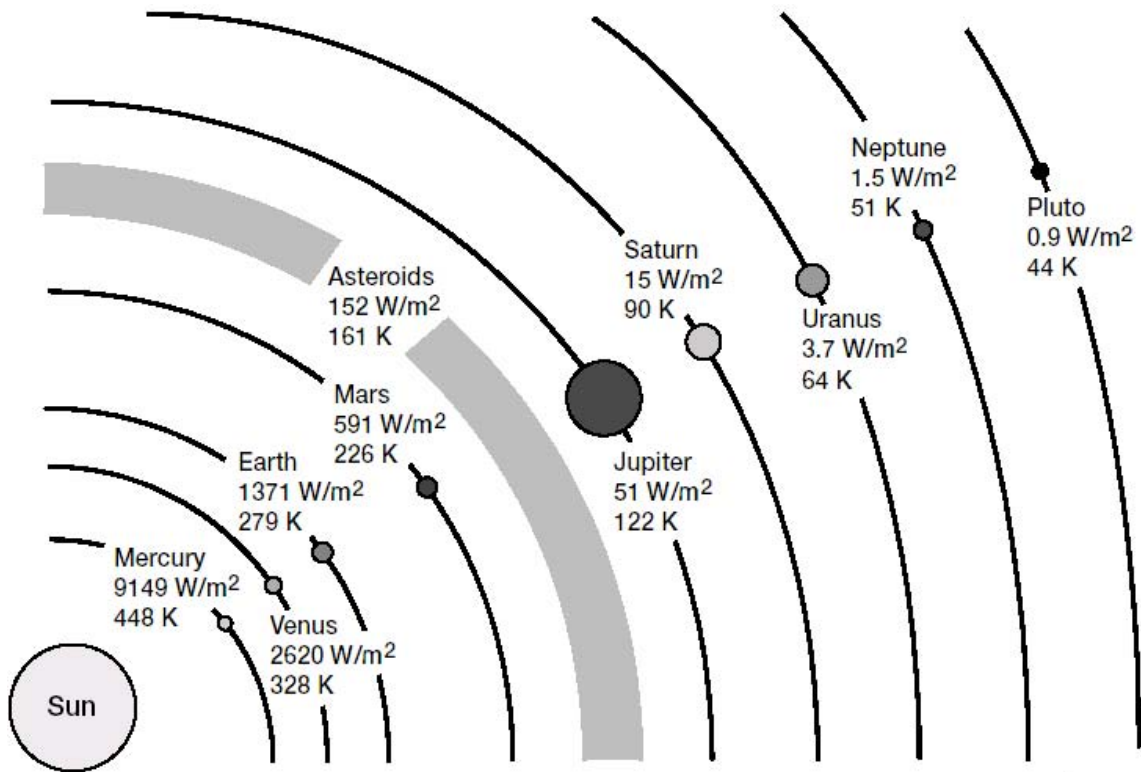
Figure 14.   Solar System Environmental Sink Temperatures for Flat Plate at 25 deg Incidence from [Ref. 20, p.9]

The best way to orient a space radiator is clearly such that it does not see the Sun. This is fortunately relatively easy because most bodies to which a nuclear powered spacecraft might be sent exist primarily in the plane of the ecliptic. Keeping the radiator oriented so that it rejects heat to relatively dark space should be a simple task. The environmental sink temperature is much more complicated to calculate than has been hinted at here. Space radiator operations are complicated by proximity to the Earth or other solar system bodies which act as separate sources of thermal radiation. Detailed thermal analysis is beyond the scope of this thesis. An average value of 200 K for the space thermal sink is used in all following arguments and calculations. This value was selected as the average value for 25 degree angle of incidence between Jupiter and Earth, the destination and origin of the Jupiter Icy Moons Orbiter discussed previously. A lower average value than this might be possible with careful trajectory planning.

The radiated heat equation (10) requires only the addition of the environmental sink temperature to make a simple but powerful model of space radiator performance. The necessary equation is given below.

$$\dot{Q}_{rad} = A_{rad} F \varepsilon \sigma (T_{rad}^4 - T_{\sin k}^4) \tag{11}$$

This is enough information to estimate required radiator area to reject the waste heat from the generation of a given amount of electrical power at a given efficiency. The consequences for a SNRPS designed to generate 100 kWe at 10%, 25% and 50% conversion efficiency appear below in Figure 15.
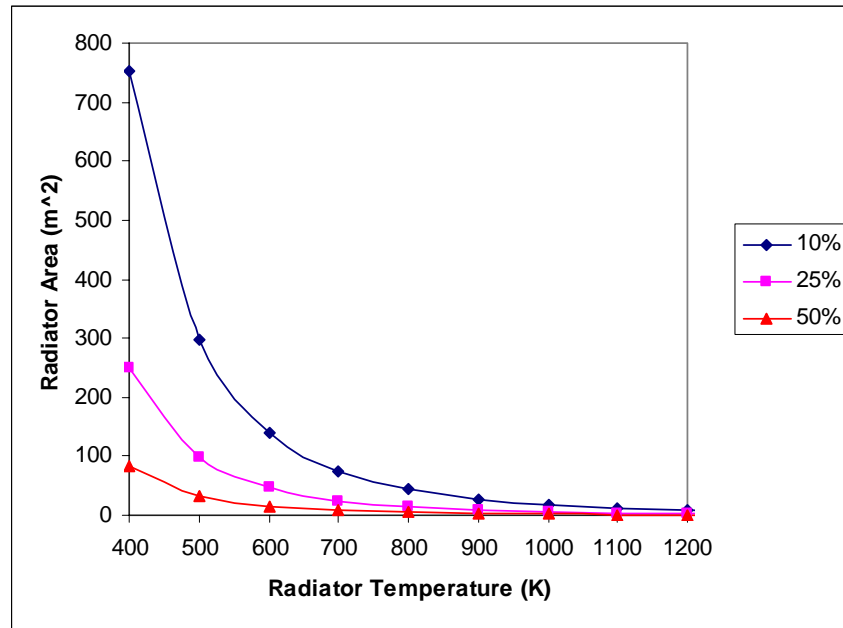
Figure 15.   Required Radiator Area for 100 kWe vs. Radiator Temperature for Three Values of η_{th}

This figure assumes an emissivity of 0.88 for reasons that will be explained shortly, a view factor of unity (indicating an unobstructed view of the space heat sink) and a space sink temperature of 200 K. The sensitivity of radiator size to operating temperature is clear. Equally clear is the benefit of higher power conversion efficiencies. The radiator temperature is determined by the temperature at which the power conversion system must be maintained to operate at the desired efficiency.

Large radiator areas translate into larger power system masses. The specific mass of a radiator is defined as the mass of one square meter of radiating surface. This is the figure of merit for a given radiator technology most often found in the literature. Once the radiator's surface area has been determined, multiplying by the specific mass yields the mass of the radiator. Radiators can be classified as one or two sided, meaning that they radiate to space from one or both sides. Two sided radiators have half the specific mass of single sided ones.

The graph of radiator mass vs. temperature looks identical since radiator mass depends linearly on area. The radiator mass for this case, assuming specific mass of 2.75 kg/m^2, is shown below in Figure 16.
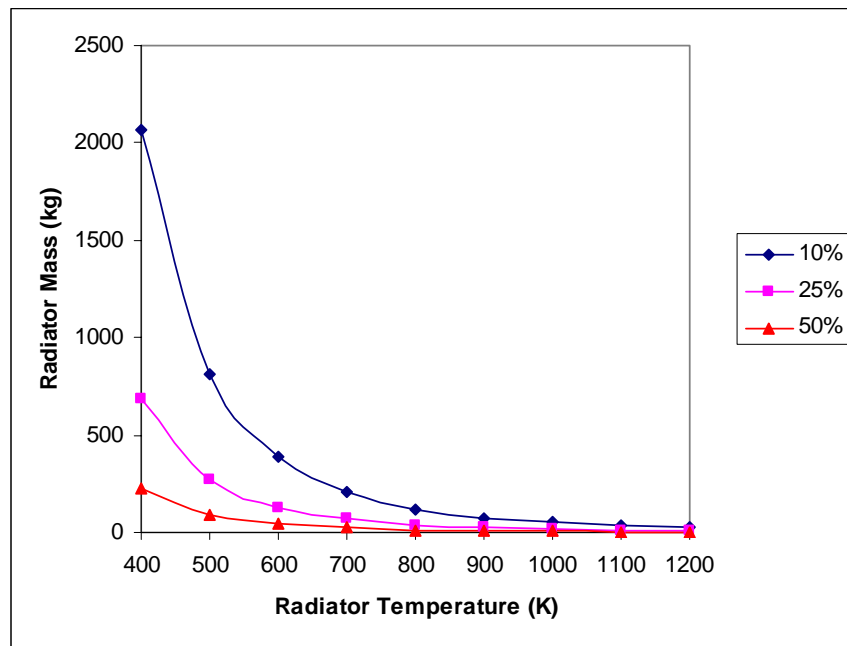
Figure 16. Radiator Mass vs. Temperature for Three Values of η_{th} Assuming 2.75 kg/m^2

This graph shows a strong dependence of radiator mass on operating temperature and reiterates the potential benefits of higher conversion efficiencies. Increased power conversion efficiency and reduced radiator specific mass are critical research and development areas for SNRPS.

2. State of the Art Space Radiators

The radiators in the Early External Thermal Control System (EETCS) presently operating on the International Space Station represent the current state of the art in high power space heat rejection system design. The EETCS is a pumped loop ammonium thermal control system that is designed to reject 14 kW of waste heat to space. Pumped loop heat transport systems, as the name implies, involve the use of a working fluid and the expenditure of electrical power to circulate that fluid. These components complicate systems and thermal control system engineers avoid them whenever possible. The arrangement of the EETCS is shown below in Figure 17.
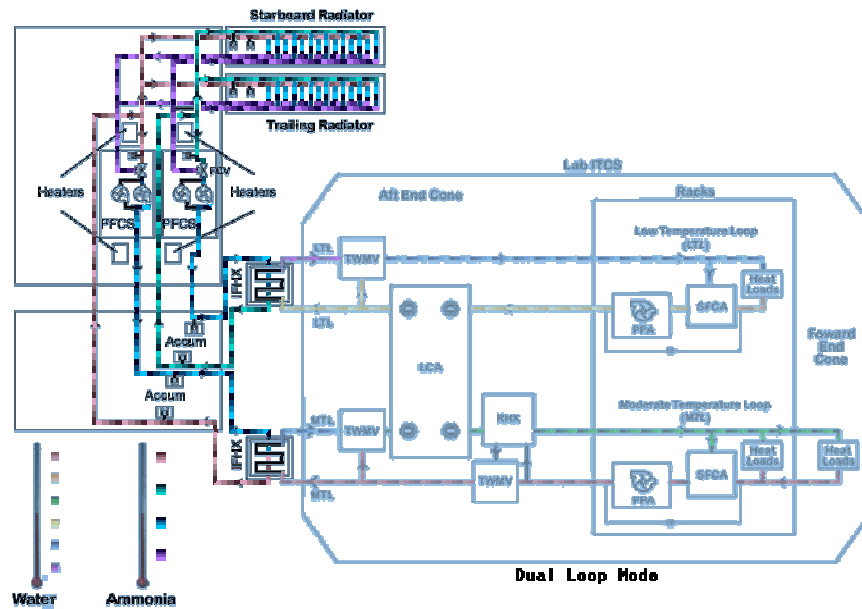
Figure 17.   ISS EETCS Schematic Diagram [courtesy NASA, JSFC]

The ammonia pumps which give the system its name appear in the upper left of the figure. Note the twin cooling loops and multiple pumps that provide the redundancy so important in a crewed spacecraft. The two radiators at the top of the diagram operate at ~300 K [Ref. 22] and have a two-sided specific mass of 2.75 kg/m^2 [Ref. 10, p.5]. These radiators have a total heat rejection area of approximately 147 m^2 and appear below in Figure 18.
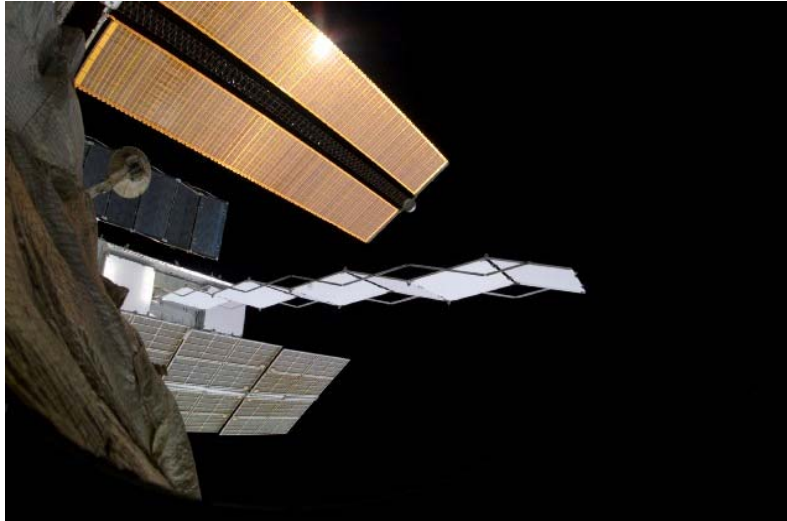
Figure 18.   ISS EETCS Radiator Deployed on S1 Truss[courtesy NASA]

The radiator is the light gray object in the center of the frame. The scissor deployment mechanism is clearly visible as well as two other radiators in the stowed position. The twin gold colored panels at the top and the gray panels at the bottom of the frame are solar arrays. The pumped loop system on the ISS is the highest power radiator currently on orbit. More typical radiators in use today on solar powered spacecraft are entirely passive, typically operate around 300K and have a specific mass of 12 kg/m^2 [Ref. 21, p. 208].

Radiators of this type are too massive for SNRPS use and heat rejection technology must advance to realize the potential of such systems. The area required to reject a given power at a given temperature is fixed because the physics underlying the irradiative heat transfer processes described above are well established and appear unlikely to change in the foreseeable future. The challenge therefore is to reduce the mass of a given radiator area which translates into reducing the radiator specific mass.

The most mature SNRPS space radiator is a heat pipe radiator. A heat pipe is a device that transports heat using two phase liquid/vapor flow. They are attractive for space application because they can move large quantities of heat with high reliability, nearly isothermally, have no moving parts, and operate well in a microgravity environment [Ref. 23, p. 3]. The heat pipe collects heat from a cooled component over a relatively

small area at high heat flux and spreads it nearly isothermally over a large surface area for radiation. A picture of how a heat pipe radiator might cool a component appears below in Figure 19.
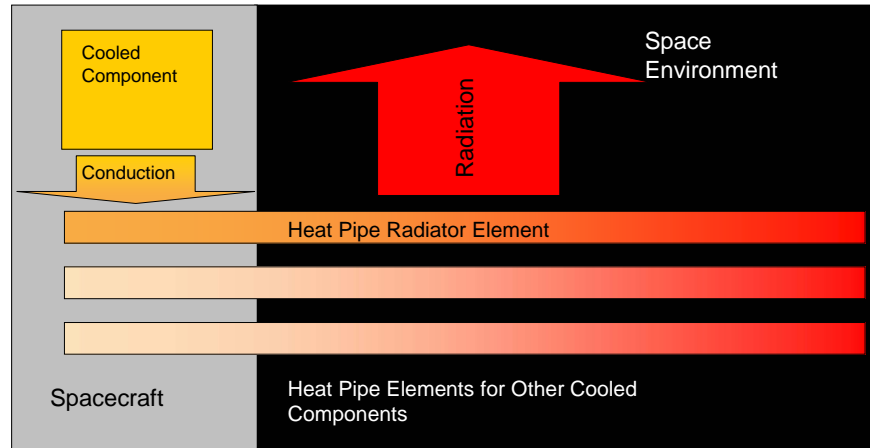
Figure 19.   General Schematic of Space Heat Pipe Radiator

The isothermal property of heat pipes makes them particularly useful as elements in space radiators because they can transfer heat without a significant temperature drop across large surfaces. Radiators that rely on pure conduction to get heat from one end to the other have large temperature drops over their surfaces which translate into lower effective radiator temperatures and larger radiators [Ref. 23, p. 74]. Furthermore, heat pipe radiators offer inherent redundancy to a space heat rejection system. Consider a pumped loop radiator that has a micrometeoroid puncture in a coolant tube. All of the coolant passing through that radiator will ultimately be lost. This means that a single puncture takes out the entire radiator. A given heat pipe radiator element will also lose all of its working fluid as a result of a micrometeoroid puncture. The difference is that that element is only one of many that make up the radiator. Overall radiator and power system performance therefore degrade gracefully [Ref. 24, p. 3]. Following sections describe the operation of a heat pipe in sufficient detail to understand this technology's potential for SNRPS heat rejection purposes. The interested reader will find additional information in [Ref. 23], [Ref. 25] and [Ref. 27].

3. Heat Pipe Theory

Capillary action or capillarity is the pumping force behind heat transfer in a heat pipe. Reliance on this force is what gives heat pipes their ability to operate reliably in a microgravity environment. It is necessary to review the physics of surface tension, wetting and capillary action prior to describing the operation of a heat pipe. Capillary action is a consequence of the surface tension experienced by molecules at the surface of a liquid. All liquid molecules attract and are attracted by surrounding molecules. Molecules in the center of a body of liquid experience no net force because they are acted upon equally by all surrounding molecules. Those at the surface, however, experience a net tension force inwards because there are no molecules to attract them on one side as illustrated below in Figure 20.

Molecule in middle of liquid
No net force

Molecule at surface of liquid
Net force
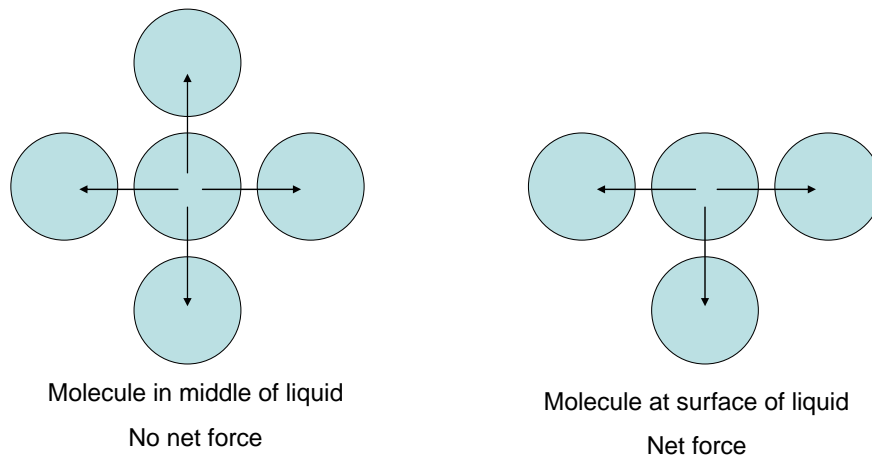
Figure 20.   Net Force on Molecule in Body of Liquid vs. at Surface

The net result of the forces depicted above is that the surface film which covers a liquid is in a state of tension. This aptly named surface tension depends on the force applied and the cross sectional area of the film. The film thickness is probably on the order of one to two molecular diameters but is not well known. The surface tension is defined as a force per unit length to avoid uncertainties over film thickness. The geometry of the situation is depicted below in Figure 21.

F = force at which liquid film breaks
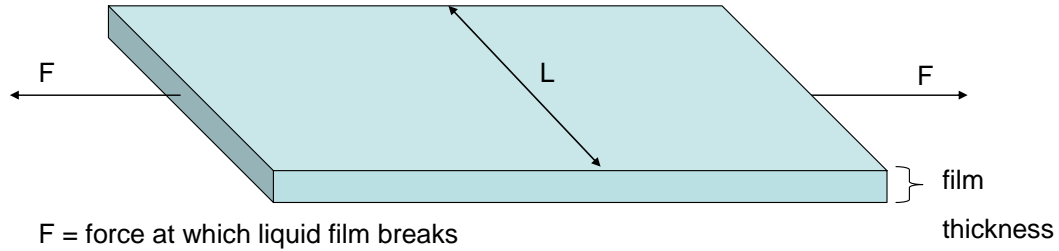
Figure 21.   Surface Tension in a Liquid Surface Film [after Ref. 23]

The surface tension, σ, is a measure of how much tension a liquid surface can support before breaking and is given in (12) below [Ref. 23, p. 14]

$$\sigma = \frac{F}{L} \qquad (12)$$

The surface tension is a characteristic of the type of liquid and the temperature. The increased random kinetic energy of molecules which accompanies a rise in temperature reduces the amount of force which needs to be applied to break a liquid film thereby reducing the surface tension. Surface tension for several liquids appears below in Table 5.

Liquid	Temperature (K)	Surface Tension (N/m)
Methyl Alcohol	323.15	0.0201
Ammonia	284.15	0.0235
Water	293.15	0.0728
Sodium	1089.15	0.121
Lithium	1477.15	0.260

Table 5.   Representative Surface Tension of Various Heat Pipe Working Fluids
[from Ref. 23, p. 14]

The table indicates various potential heat pipe working fluids and their surface tensions at temperatures of interest to heat pipe designers. Higher surface tensions are associated with greater capillary pumping power in heat pipes. The table indicates which working fluids might be useful for higher temperature heat pipe operation.

The interaction of liquids with solid surfaces is crucial to capillary action and, hence, heat pipe design. Consider a drop of liquid in contact with a surface of different material. The liquid droplet tends to partially deform. The degree of deformation is determined by the forces between the molecules in the liquid and those in the solid. These forces can be either attractive or repulsive. The tendency of liquid molecules to stick to each other is called cohesion while adhesion refers to the tendency of liquid molecules to bind to the solid molecules. A liquid is said to wet a solid when the adhesive forces predominate over cohesive forces. A liquid is said to be nonwetting to the solid when cohesive forces predominate. The contact angle that the liquid surface makes with the solid is a measure of the degree to which a given liquid is wetting or nonwetting to a given surface. Contact angles less than 90 degrees indicate wetting and those greater than 90 degrees indicate nonwetting liquids. The situation is diagrammed below in Figure 22.

Wetting Liquid
$\Theta < 90°$

Nonwetting Liquid
$\Theta > 90°$
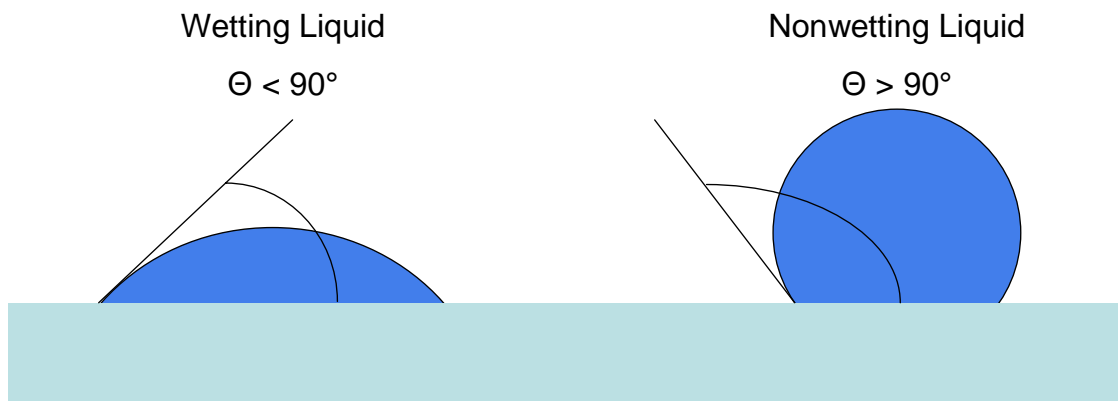
Figure 22.   Wetting and Nonwetting Liquids with Characteristic Contact Angles

The amount of droplet cohesion is related to the surface tension and is therefore determined by the type of liquid and its temperature. The level of adhesion of a given liquid is a function of the solid surface material, level of cleanliness, roughness and a host of other factors. A given liquid may adhere to some solids and not to others. Heat pipe performance is therefore strongly dependent on material selection, fabrication techniques, and cleanliness.

Capillarity is the ability of a curved liquid surface to sustain a pressure differential across itself. The idea is central to capillary action and heat pipe operation. The classic example of capillary action occurs when a thin glass tube is submerged into a pool of

liquid. The liquid establishes a meniscus at some height in the tube according to the wettability of the surface by the given liquid as shown below in Figure 23.
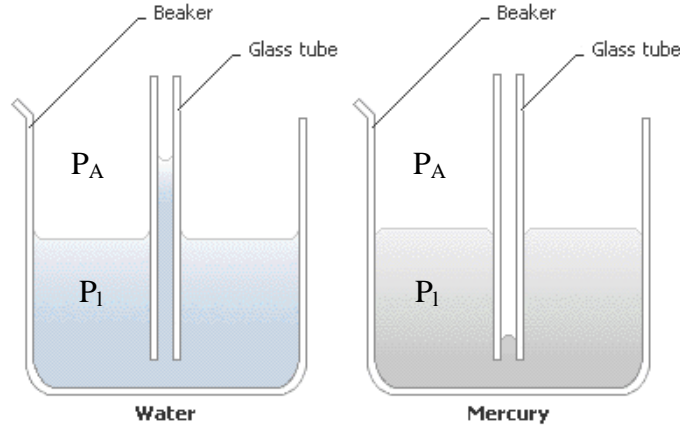
Figure 23.   Capillary Action in Water and Mercury [from Ref. 26]

The water in the figure above is wetting to the glass beaker. The mercury is not. Note the characteristic shapes of the liquid surfaces in the figure and compare them to those in Figure 22. Consider the pressure difference across the water in the left figure. Adhesive forces draw the liquid up as it wets the glass tube and establishes a meniscus. The pressure inside the liquid column inside the glass tube is the same as that at the pool surface: atmospheric pressure, P_A. The pressure decreases as one moves up in the water column. It starts at P_A at the base and decreases to some value, P_l, at the top. The difference between the two pressures is the hydrostatic head of water above the fluid surface in the tube. Assuming that the liquid density remains constant throughout the water column:

$$P_l = P_A - \rho_l g h \tag{13}$$

where ρ_l is the liquid density, g is the acceleration due to gravity and h is the height of the water column. An expanded view of the situation is illustrated below in Figure 24.
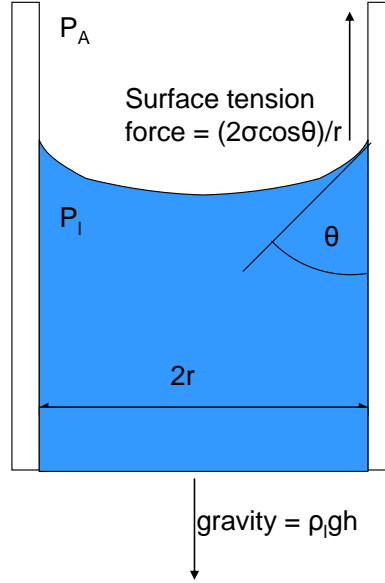
Figure 24.   Expanded View of Wetting Meniscus Showing Force Balance

This situation provides a measure of the pressure differential that the adhesive forces can support. The net pressure differential across the meniscus is $P_A - P_l$. The total downward force from the atmosphere is then obtained by multiplying the pressure differential by the area at the top of the tube, neglecting the curvature of the meniscus.

$$F = \pi r^2 (P_A - P_l) \tag{14}$$

Here r is the inner tube radius. This force must be exactly balanced by the vertical component of the surface tension if equilibrium is to be maintained.

$$\pi r^2 (P_A - P_l) = 2\pi r \sigma \cos\theta$$
$$P_A - P_l = \Delta P_C = \frac{2\sigma}{r}\cos\theta \tag{15}$$

Recall that σ is the surface tension and θ is the contact angle between the fluid and solid surfaces. ΔP_C is the maximum capillary pressure that the liquid can support under the given circumstances. Note that the contact angle can have values greater than 90 degrees which produces negative pressure differentials. This explains why the non-wetting mercury drops down below the pool surface on the right side of Figure 23. Note also that no gravity forces appear in Equation (15).

A hydrostatic pressure differential like the one illustrated above is only one kind of pressure differential that capillary action can offset. It is capillary action which provides the pumping force in a heat pipe. A heat pipe is essentially a recirculating fluid heat transport loop enclosed in a container. It is divided into three sections which appear below in Figure 25.
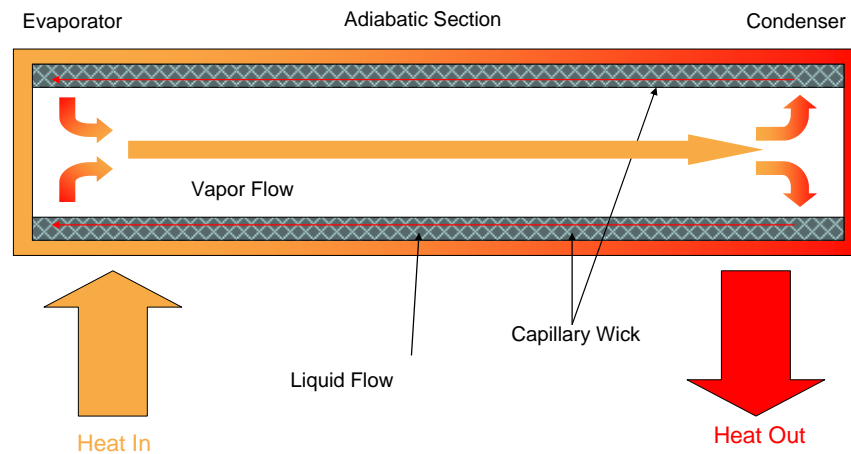
Figure 25.   Basic Internal Components of a Heat Pipe

The heat is applied to the evaporator section to vaporize a working fluid. Vapor then travels through an adiabatic section to the condenser where it is cooled. The resultant liquid is trapped in a porous wick and sent back down the pipe to the evaporator. The pipe relies on the latent heat of vaporization of a liquid to absorb energy in an evaporator section, the resultant pressure gradient to move the resultant vapor to a condensing section, and capillary action through a fine porous wick to return the liquid to the evaporator along the walls. Two reasons that heat pipes are useful in space radiators become clear. The first is that the local acceleration due to gravity does not appear in Equation (15). That explains their utility in microgravity: their capillary pumping action does not depend on gravity for operation. Also, note that the heat transfer occurs when the liquid evaporates at the hot end of the heat pipe. The vapor then travels rapidly to the condenser without significant time to cool. It thus reaches the condensing sites at almost the same temperature at which it started, providing for a nearly isothermal radiating surface and a higher average radiator temperature. Recall that radiator area is strongly dependent on temperature from Figure 15.

The working fluid experiences pressure drops due to frictional forces as it moves around the heat pipe's internal "loop". These pressure drops must be offset by the capillary pressure in the porous wick on the walls of the heat pipe. The most basic limit to heat pipe operation, therefore, is called the capillary pumping limit. This limit is reached when capillary pressure cannot make up for the pressure drop experienced by the working fluid. The evaporator eventually dries out and the heat pipe ceases to function when this limit is reached. Equation (15) gave a general formula for the capillary pressure in the wick of a heat pipe. This equation is commonly simplified to eliminate the contact angle as shown below in Equation (16).

$$\Delta P_C = \frac{2\sigma}{\dfrac{r}{\cos\theta}} = \frac{2\sigma}{r_P} = \frac{4\sigma}{D_P} \tag{16}$$

This defines an effective pore radius, r_p, and an effective pore diameter, D_p. Equation (16) is desirable because contact angles are often difficult to measure. It gives the maximum capillary pressure capability that a given wick/working fluid can produce when the effective pore diameter is equal to the diameter of curvature of the liquid-vapor interface in the pores, D_C, as shown below in Equation (17).

$$\Delta P_{C,\max} = \frac{4\sigma}{D_C} \tag{17}$$

The total pressure drop in the heat pipe is often expressed as a sum of the vapor and liquid pressure drops. The maximum capillary pressure drop must equal or exceed this value in order for the heat pipe to function.

$$\Delta P_{C,\max} \geq \Delta P_{vl} = \Delta P_v + \Delta P_l \tag{18}$$

Other operating limits can profoundly affect heat pipe operation but are less fundamental than the capillary limit and will only be summarized here. They are the viscous, entrainment, boiling, and the sonic limits. The viscous limit is reached when the viscous forces overcome the vapor pressure difference between the evaporator and condenser sections. Heat pipes with extremely long condenser sections can encounter this limit. It is avoided by ensuring that the overall vapor phase pressure drop is less than 10% of the absolute vapor pressure in the evaporator [Ref. 27, p. 78]. The entrainment limit

results from the shear forces at the counter-flowing vapor-liquid interface along the interior surface of the heat pipe. These forces can overcome surface tension, entrain drops of liquid in the vapor flow and lead to evaporator dryout if the heat input is too high. [Ref. 27, p. 85]. The boiling limit at first appears to be mislabeled because heat pipes are inherently two phase devices and boiling is required for their operation. The problem comes when the liquid boils at the heat pipe wall and not at the liquid-vapor interface in the wick. Some critical heat flux applied to the surface of the heat pipe causes this phenomenon which can lead to dryout. The heat flux at which bubbles begin to form on the heat pipe wall is the boiling limit [Ref. 27, pp. 97-98]. Heat pipes operate, to a certain extent, like the converging/diverging nozzles in rocket engines. The evaporator is like the thrust chamber and the condenser is like the nozzle. The sonic limit is reached when the vapor leaves the evaporator at the speed of sound for the evaporator vapor temperature [Ref. 23, p. 126]. This limit differs from others in that it does not necessarily result in evaporator dryout. Instead, it limits the heat transport rate down the heat pipe because the flow is choked by a shock front at the evaporator exit [Ref. 25, p.86].

These operating limits, together with the capillary limit, define a performance map like the one shown below in Figure 26.
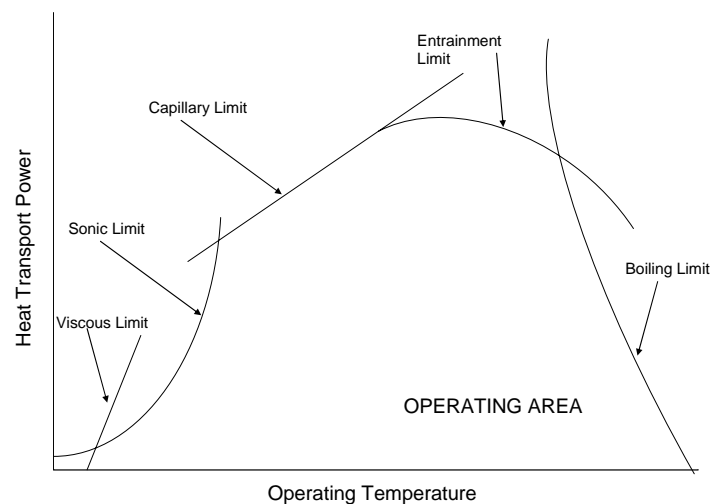
Figure 26.   Generic Heat Pipe Power vs. Operating Temperature [after Ref. 27, p. 124]

A heat pipe can function as long as the input heat flux and operating temperature are within the limits set by this curve. The figure gives a general idea of which limits come in to play in which operating regimes. Proper design will result in a heat pipe that operates well clear of all of these limits across a wide range of temperatures.

F.   SP-100: SPACE NUCLEAR REACTOR POWER SYSTEM

It is useful to see the components described in the preceding sections combine into an actual design. The Space Power-100 (SP-100) system is a good example of a recent space reactor design which illustrates the current state of the art in this country. This program was cancelled before a flight article could be produced. The SP-100 program began in February 1983 as a cooperative venture between the Department of Energy (DOE), National Aeronautics and Space Administration (NASA) and Defense Advanced Research Projects Agency (DARPA). The program was designed to identify the needs of various potential users of a space nuclear power system and develop common expandable hardware to meet them. The program's initial technology goal was the creation of a space reactor with a 100 kWe power rating and a 10 year operational life [Ref. 15, p.35].

Five years of system studies resulted in the selection of the basic technologies by July 1988. The Generic Flight System (GFS) was the baseline configuration. It consisted of a uranium nitride reactor with liquid lithium coolant and refractory metal core construction. Thermoelectrically driven liquid metal pumps circulated the lithium to SiGe thermoelectric power conversion cooled by potassium heat pipe radiators [Ref. 15, p. 29]. The design produced a series of "building blocks" which could be modified as improved power conversion systems became available or different power levels were desired. The operational configuration and basic performance characteristics of the GFS design are shown below in Figure 27.

Mass
5400 kg
Reactor Thermal Power
2.4 MW_{th}
Reactor Outlet Temperture
1375 K
Shadow Shield Half-Angle
17 degrees
Delivered Electrical Power
100 kW_e at 200 V_{DC}
Radiator Temperature
800 K
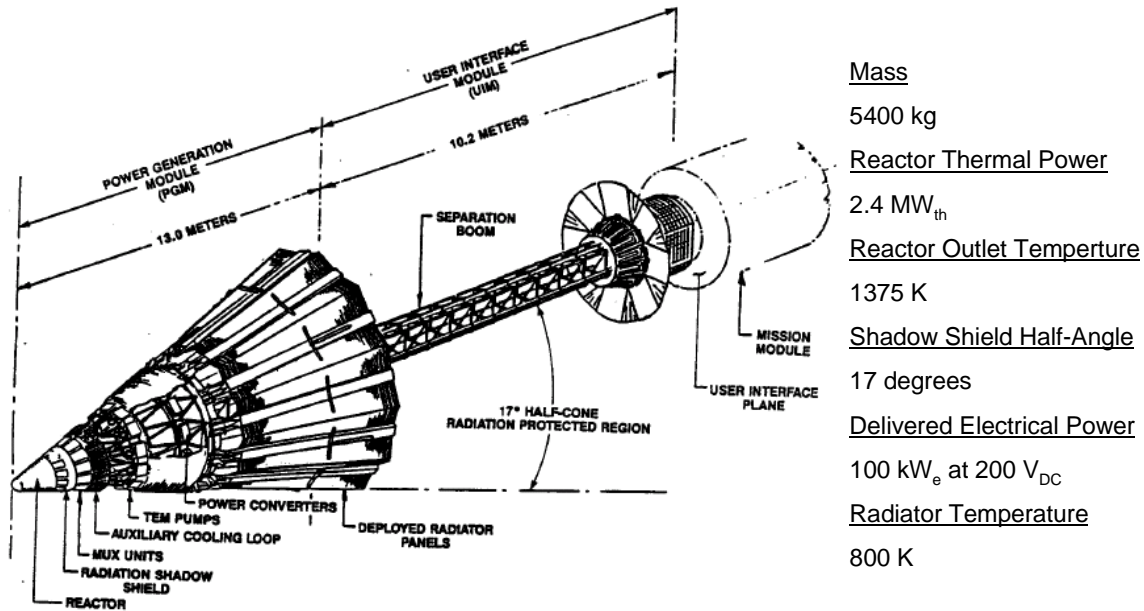
Figure 27. SP-100 Reference Flight System Configuration [from Ref. 15, p. 31]

The total system size was to be 23.2 m from the reactor (considered the "front") to the user interface plane. The reactor itself appears at the left of the figure, as far as possible from the generic payload pictured at the right. A shadow shield immediately "aft" provided neutron and gamma radiation protection in a 34° cone behind the reactor. Aft of this was the power conversion system and radiator panels. These assemblies collectively formed the Power Generation Module (PGM). The separation boom, power conditioning equipment, batteries, payload mounting, and system controls form the User Interface Module (UIM).

1. Reactor and Primary Heat Transport System

The final reactor design appears schematically below in Figure 28. The reactor employed uranium nitride, lithium coolant, and fast spectrum neutrons to maintain the chain reaction. Twelve radially mounted beryllium oxide reflectors controlled the reaction rate during normal usage. There were also three boron-carbide in-core safety rods that provided a redundant emergency shutdown system in case of accident. The reactor pressure vessel and fuel cladding consisted of a niobium alloy. Extensive use of rhenium in the fuel elements protects the fuel from the lithium coolant, minimizes

cladding mass, and acts to control the reactor the event it is immersed in water during a launch accident. The overall thermal power output was 2.4 MWt and the peak end-of-life fuel temperature was 1450 K. [Ref. 16, pp. 2-4]
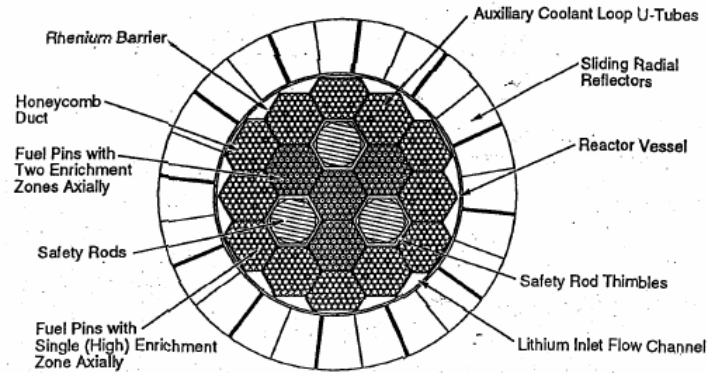
Figure 28.　　　SP-100 Reactor Core Components [from Ref. 16, p.4]

The reactor, reflectors, and radiation shield (discussed in next section) were enclosed in a carbon-carbon re-entry shield designed to keep the reactor at 300K during a re-entry accident. The reentry shield might reach 3200 K during such an accident. The arrangement of the reactor, re-entry shield, radiation shadow shield and reactor control components appear below in Figure 29. [Ref. 16, p. 5]
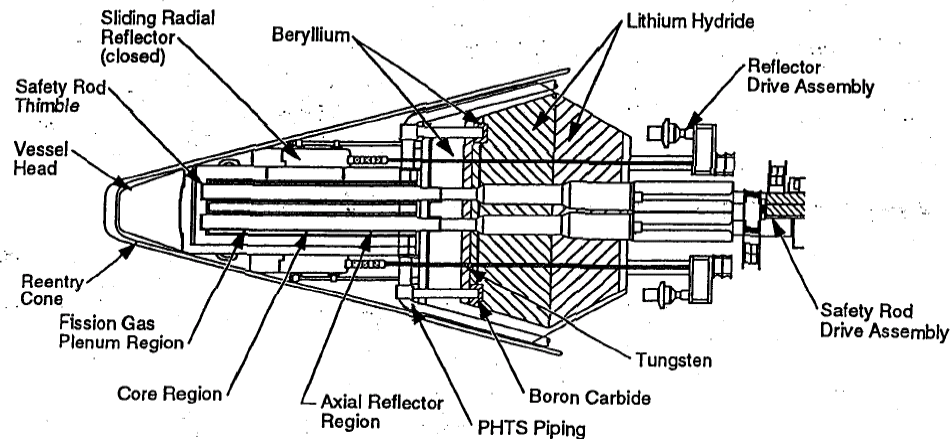
Figure 29.　　　SP-100 Reactor, Control, and Radiation Shield Arrangement [from Ref. 16, p.4]

Also shown in the figure is the arrangement of the Primary Heat Transport System (PHTS) piping which directed hot lithium coolant at 1375 K. There were twelve

coolant loops in the PHTS. The loops shared a common plenum in the reactor vessel so a single micrometeoroid penetration could eventually result in the loss of all coolant. The loops were therefore configured to minimize that possibility. A dual action pump moved hot coolant to the power conversion system via thermoelectric-electromagnetic (TEM) pumps. These pumps were dual action by virtue of the fact that a single pump body circulated both the primary and heat rejection fluids for a given loop (discussed in a later section). A schematic PHTS loop appears below in Figure 30.
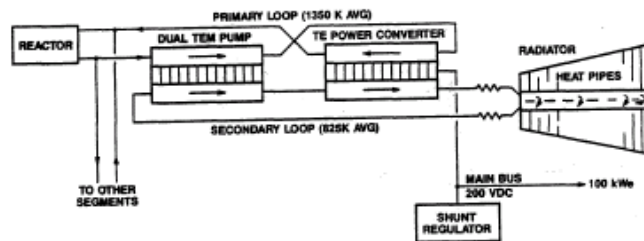
Figure 30.   PHTS Loop Schematic [from Ref. 15, p. 32]

The TEM used the temperature difference between the primary and secondary loops to generate electric current in the molten coolant. The current generated a magnetic field. The interaction of the electromagnetic field produced a force on the coolant proportional to the temperature difference between the loops. This provided an important reactor control element because it tended to increase pumping action automatically when reactor core temperature increased. [Ref. 15, p. 32]

2.   Radiation Shield

The SP-100 radiation shield was a shadow configuration as previously mentioned. The 34° cone angle on the shadow shield reduced the dose to the power conversion systems, radiators, control electronics, and the payload. Payload doses were further reduced by the use of a 22m separation boom which, in combination with the shield, yielded cumulative doses to the payload of 10^{13} neutrons/cm^2 and 10^5 gamma rads (silicon) over a ten year mission. Tungsten and depleted uranium were used for gamma attenuation with the majority of the shield volume taken up with lithium hydride for neutron absorption. The shield structure was primarily to be fabricated from stainless steel. The proximity of the shield to the PHTS piping and reactor vessel head illustrate a typical thermal problem in shield design. The low temperature shielding materials had to

be kept thermally isolated from high temperature components. Beryllium layers embedded in the shield served a dual role as thermal conductors and neutron absorbers. [Ref 16, p. 5]

3. Power Conversion

The twelve independent lithium coolant loops carried thermal power from the reactor to thermoelectric converters. Designers favored thermoelectric conversion largely because it eliminated mechanical parts as possible system failure modes. The system produced output electrical power of 100 kWe at 200V for main bus loads and 300We at 28 V for secondary loads. The system's projected overall thermal to electrical conversion efficiency was on the order of 4%. It used conductively coupled SiGe/GaP thermoelectric converters. The same technology provided the TEM pumps that drove lithium coolant in the primary and secondary loops. 8640 of these cells were split into 12 Power Conversion Assemblies (PCA) and one PCA was placed in each loop. A schematic of the PCA appears below in Figure 31. [Ref. 15, pp. 34-35]
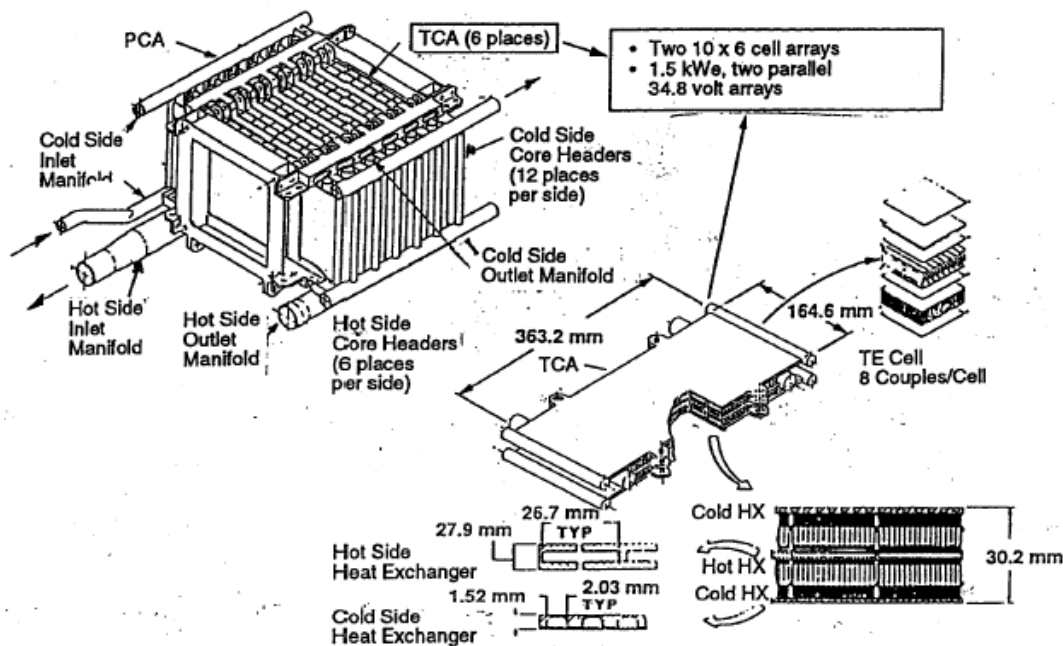
Figure 31.   SP-100 Power Conversion Assembly [from Ref. 16, p. 8]

The PCA consisted of 6 Thermoelectric Converter Assemblies (TCA) each of which held two cell arrays of 60 cells each. The arrays were connected in parallel and the TCA in series to produce the required 200 V output. Each cell array was rated at 1.5 kWe

and the power system was capable of providing the full rated 100 kWe with one loop entirely out of commission. Each PCA also contained hot and cold side heat exchangers and fluid lines to connect it to the primary and secondary lithium coolant loops. [Ref. 16, pp. 7-9]

4. Heat Rejection

Liquid metal coolant loops had flown on the earlier SNAP reactors and thus a considerable body of knowledge existed in their design and operation. The low temperature lithium secondary loop provided a cold reservoir for the power converters and a means to radiate the waste heat. Recall that the TEM pump installed in a loop provided motive power for coolant flow in the primary and associated secondary fluid. The secondary lithium coolant would circulate in a duct to which beryllium-titanium heat pipes with potassium working fluid were brazed to increase radiator area. The total available radiator area was 106.4 m^2 and the radiators operated at 800 K. The duct was armored against micrometeoroid impact because its puncture would result in loss of the loop. The heat pipes were not so armored because sufficient number could be mounted to account for expected losses over design life. The lithium lines had flexible joints to permit deployment of the duct/radiator. [Ref. 15, p. 35]

This section has introduced the motivation for studying space nuclear reactor power systems and described their essential components. The Generic Flight System SP-100 system has been described and will later be used as a baseline to assess the utility of thermophotovoltaic power conversion in future space nuclear reactor power systems. The next two chapters describe this conversion technology in preparation for that assessment.

THIS PAGE INTENTIONALLY LEFT BLANK

III.   THERMOPHOTOVOLTAIC ENERGY CONVERSION TECHNOLOGY

Thermophotovoltaic (TPV) conversion of heat energy into electrical power for spacecraft is closely related to common solar photovoltaic energy conversion technology. The achievements of modern solar cell designers offer hope that TPV will ultimately provide a static conversion technology capable of the high efficiencies presently reached by dynamic systems. This chapter introduces photovoltaic technology, describes the components of a TPV system, and discusses the importance of the incident light spectrum on cell material selection. Some of the radiation terminology and theory described in Chpater II Section E.1 will reappear here to describe the transfer of photons between the TPV cells and their heat source radiators.

A.   SEMICONDUCTOR PHYSICS

Thermophotovoltaic cells are a subclass of photovoltaic cells. These are semiconductor devices that produce and maintain a voltage across their terminals when exposed to a photon flux. This technology is already well known from solar cells. These devices depend on the physics of semiconductors, doping, and p-n junctions so a brief review is appropriate here.

Quantum theory dictates the allowable energy states for the electron cloud around an atom. A discussion of the physics behind these numbers is beyond the scope of the present work. It is sufficient to note that atoms can be classified according to the number of electrons in their outermost energy level or valence band. Silicon, with four electrons in its valence band, is a Group IV material. Electrical conduction in solids is dependent on electrons in the valence shell of atoms becoming unbound and moving freely throughout whatever crystal those atoms are part of. It requires a certain minimum energy to do this. That energy minimum is the bottom of the conduction band. The amount of energy required to get an electron to that level from the valence band is called the band gap energy or band gap of the material. Band gaps are unique to each atom. A material will be an electrical conductor, semiconductor or insulator based on its band gap as shown below in Figure 32.
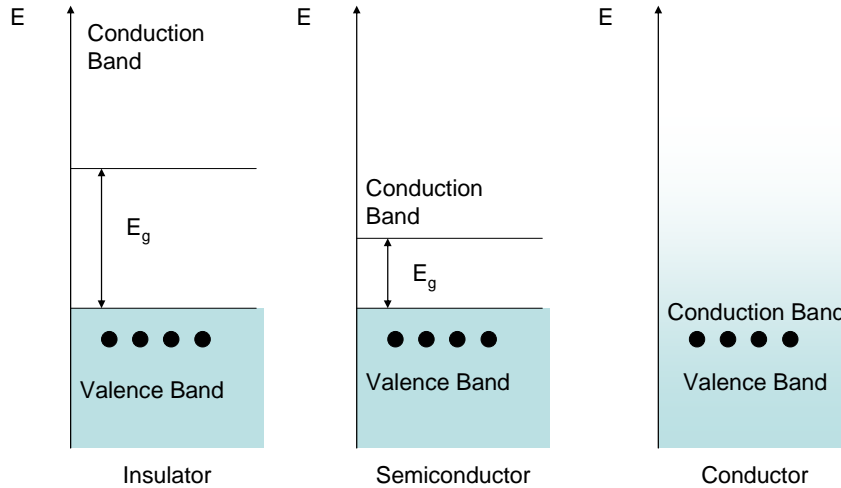
Figure 32.   Band Gap of Insulator, Semiconductor, and Conductor

Relatively non-conductive materials are known as insulators and they have large band gaps. Conductors have zero or negative band gap energies. A semiconductor is a solid whose conductive properties lie between these extremes. The valence band of such materials is full when they are at absolute zero temperature. This renders them insulating at that temperature. Heating the sample adds energy to the lattice. Random thermal excitations then raise a small fraction of the electrons out of the valence band and into the conduction band. These electrons leave behind positive "holes" in the valence band which have been shown to behave like positively charged particles within the lattice. It is thus common to talk about electrons and holes moving around a semiconductor. The electron distribution in a semiconductor at absolute zero and two increasing temperatures above it is shown below in Figure 33. Note that the temperature does not change the band gap in this simplified model. Also note that higher temperatures imply more free energy present in the crystal lattice so that more electrons are excited into the conduction band. These electrons become free charges available for conduction. Thus the material becomes increasingly conducting as the temperature is raised.
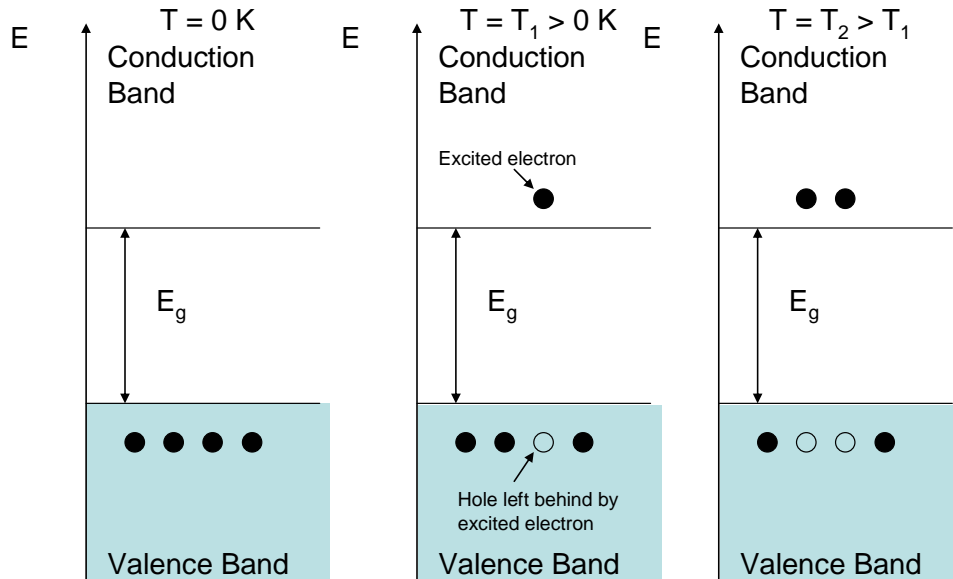
Figure 33.   Band gap of a Semiconductor At and Above Absolute Zero

Impurity addition can also add charge carriers of a particular type to a semiconductor crystal. This is called doping. It works because of the nature of the bond structures that semiconductors make in their pure crystalline form. These bonds are depicted below for a Group IV intrinsic semiconductor in Figure 34. Atoms in the crystal form covalent bonds by sharing their electrons. The valence shells of these atoms are considered full. The electrons have an equal probability of being found in orbit around each nucleus. The addition of an impurity atom with an unfilled valence shell introduces extra electrons or holes into the lattice. Impurities that introduce extra electrons are called donor impurities and those that introduce extra holes are called acceptor impurities. These extra charge carriers are less tightly bound than other carriers and are available to support conduction throughout the lattice. Semiconductors that are doped are called extrinsic semiconductors. The addition of extra electrons through doping creates an n-type material and extra holes produce a p-type material. [Ref. 28, pp. 74-76]

Pure Group IV Semiconductor   N-Type Extrinsic Semiconductor   P-Type Extrinsic Semiconductor

With Group V Donor Impurity Atom   With Group III Acceptor Impurity Atom
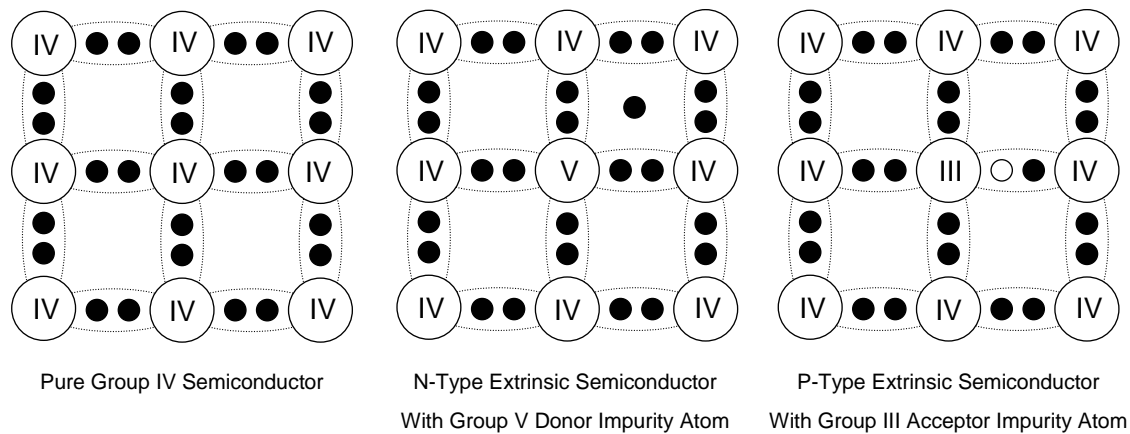
Figure 34.   Bond Structures of Intrinsic and Extrinsic Semiconductor Crystal

The band energy diagram below helps to illustrate the changes in the energy structure of extrinsic materials. Addition of donor impurities places an occupied electron energy level near to the conduction band. Small amounts of thermal energy then move more electrons into the conduction band, increasing the number of free electron carriers. Acceptor impurities place a new energy level near the valence band of the bulk semiconductor. Thermal excitation then moves electrons from the valence band into this intermediate acceptor band and creates holes. It is important to note that the materials remain electrically neutral after doping. It is simply the number of free charge carriers that has been changed. There is always a fixed charge to maintain neutrality. This becomes important in the next section.
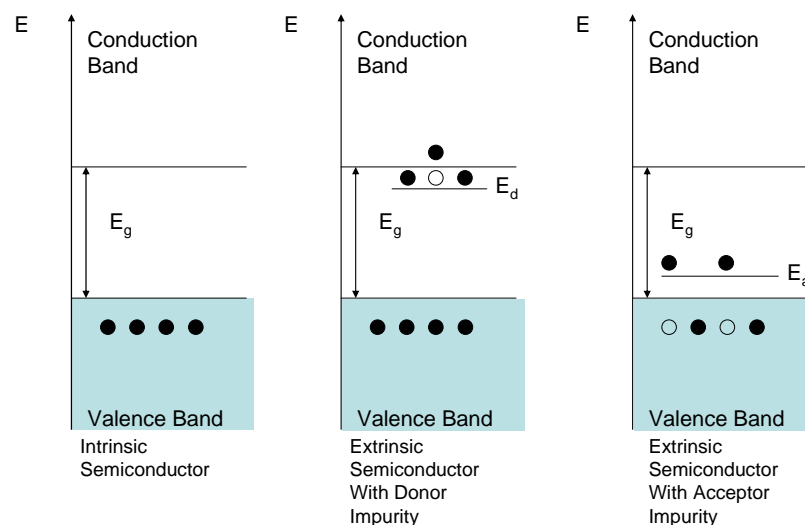
Figure 35.   Energy Diagrams in Intrinsic and Extrinsic Materials [after Ref. 28, p. 76]

52

It should be noted that non-elemental semiconductor materials exist. Solid solutions of Group III and V elements display semiconductor properties. These are called compound semiconductors and are distinguished as binary, ternary, or quaternary based on the number of elements they contain. These compounds will play an important role in the advanced photovoltaic devices discussed later [Ref. 30, p. 512].

B.   P-N JUNCTION

The behavior of junctions formed by the fusion of the two types of extrinsic semiconductor materials is critical to the operation of a photovoltaic cell. Such a p-n junction appears schematically below in Figure 36. Pieces of n and p type materials are brought into intimate thermal, electrical, and chemical contact. Charges can move freely between the two. Each extrinsic material has an excess concentration of free charge carriers of a different type. There is thus a concentration gradient across the junction and free charge diffusion acts to reduce it. This process would continue until homogeneous concentrations had been reached if the overall material was not electrically neutral. The excess charges create local regions of fixed opposing charge whenever they leave their parent material. Thus electrons diffusing across the junction into the p-type material expose positively charged atomic cores. Eventually a local charge separation builds up in a region centered on the junction from which free charges have diffused. This is called the depletion region [Ref. 28, pp. 159-160].
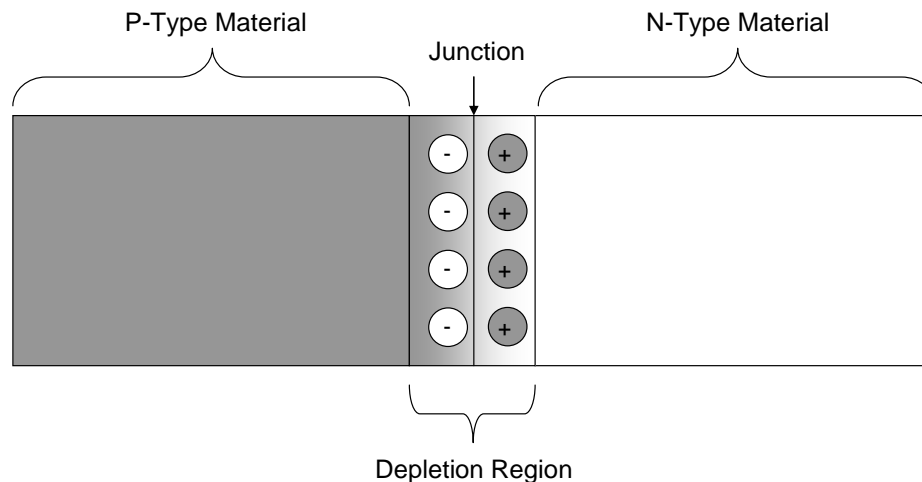
Figure 36.   P-N Junction

53

The electric currents created by the diffusion action and electric field created by charge separation in the depletion region are called diffusion and drift currents, respectively. These currents cancel each other out in p-n junctions under equilibrium conditions. The primary effect for the present purpose is that the electric field created by the exposed fixed charges creates a fixed internal potential difference called the contact potential, V_0, as shown below in Figure 37.
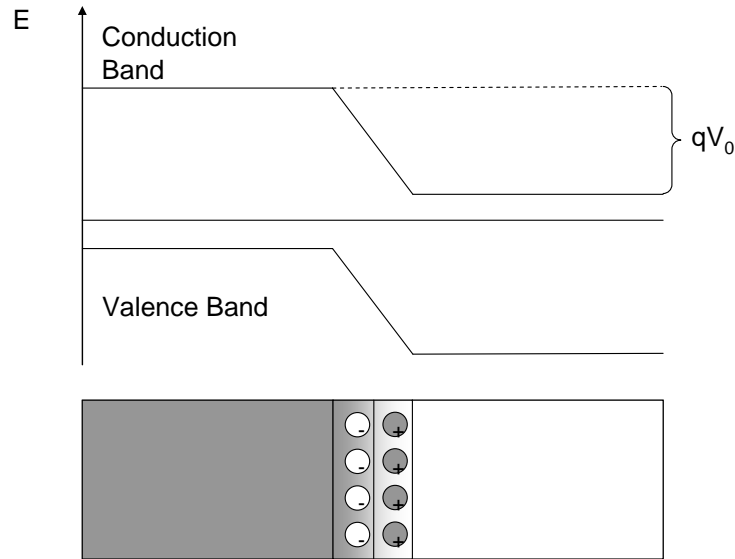
Figure 37.   Energy Band Diagram of PN Junction [after Ref. 28, p. 159]

The energy levels of each material are offset from each other by an amount related to the contact potential and the electron charge, q. The magnitude of the contact potential depends on the number of intrinsic carriers in the device, the temperature and the doping level. This "built in" voltage difference is the mechanism that allows the conversion of incident light to electrical current in a photovoltaic cell.

C.   **PHOTOVOLTAIC CELL**

The contact potential of a p-n junction will separate an electron-hole pair that is created near it and produce a current if the junction is connected to an external circuit. Electron-hole pairs are produced through the photoelectric effect when the junction is illuminated by light. The photoelectric effect occurs when an incident photon is absorbed by a bound electron and transfers enough energy to cause the electron to become unbound. Note that this means that the incident photon requires at least the bandgap

energy to move an electron from the valence to the conduction band. This creates an electron-hole pair. A photovoltaic cell consists of a p-n junction whose plane is illuminated by incident light. Contacts are attached to each of the extrinsic semiconductors to collect the separated charge and direct it to the external circuit. There is typically a continuous contact at the backplane and fingers or filaments on the front plane to allow light into the junction. The contacts are connected to an external load and the cell provides direct current power at a voltage determined by the illumination level and ultimately limited by the contact potential of the junction [Ref. 28, p. 381]. The arrangement of these components and the possible fate of incoming photons are diagrammed below in Figure 38.
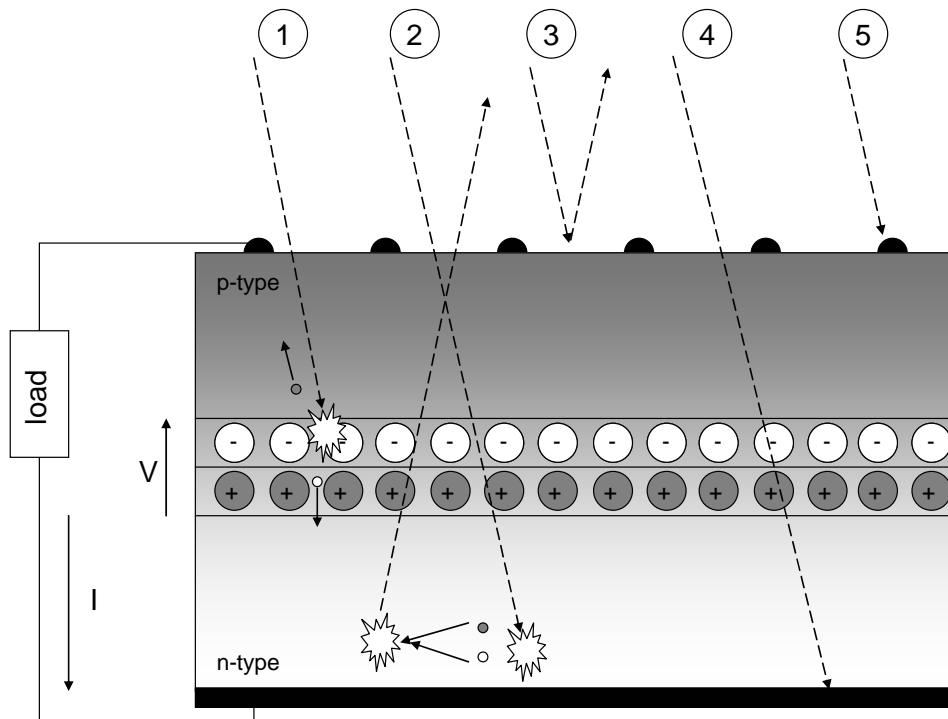
Figure 38.   Schematic of Illuminated Photovoltaic Cell

The photon labeled #1 above follows the path that the device designer prefers. It produces an electron-hole pair close to the junction, the charges separate, and they drive current to the load. Other photons are less well behaved. Some (#2) create electron-hole pairs but too far away from the junction for the local electric field to separate the charges. These carriers recombine; either immediately emitting a photon (shown) or slowly losing

energy due to interactions with the lattice. Some photons (#3) reflect off of the cell surface. Some (#4) pass through the cell without incident only to be absorbed at the backplane. Some (#5) are absorbed or reflected from the contacts at the front surface. Only the first chain of events leads to current in the external circuit. The others result in lost incident energy and increased cell heating both of which lower efficiency and output power. [Ref. 29].

The energy of the incident photons effects cell performance in more ways than simply determining whether charge pairs are produced. Obviously photons whose energies are below the band gap of the cell will not produce electron-hole pairs. Some of these photons will be still absorbed in the cell and cause heating. This heating increases cell series resistance and decreases efficiency. Photons that have energy higher than the band gap cause over-excitation losses. These losses result when excited electrons surrender energy to the semiconductor lattice. This also leads to cell heating with its attendant drop in efficiency. Thus, the efficiency of a cell is generally maximized when it is exposed to photons whose energies are above but near its bandgap.

There are other internal processes which conspire to prevent charges from flowing to the external circuit even when they are born in sufficient proximity to the junction to ensure separation. Internal recombination of charge can still occur within the bulk semiconductor material as a charge travels to the contacts. This recombination is enhanced by impurities and imperfections in the crystal structure which leave holes in the lattice to absorb passing electrons into covalent bonding. These impurities include the dopants necessary for junction formation and doping levels are therefore a significant consideration in photovoltaic cell design. The contact potential is proportional to the doping concentration which drives the designer to high doping levels but doping increases recombination and reduces output current. Ohmic resistance associated with the junction, the bulk material and the contacts also reduces output current and voltage. [Ref. 28, pp. 382-383]

D.   THERMOPHOTOVOLTAIC SYSTEM COMPONENTS

The traditional use of photovoltaic conversion has been converting solar flux into electrical power in spacecraft. The present section introduces the thermophotovoltaic system which converts the photon flux radiated from a heat source into electrical power.

The components of a TPV system appear below in Figure 39. They are discussed in more detail in succeeding paragraphs.
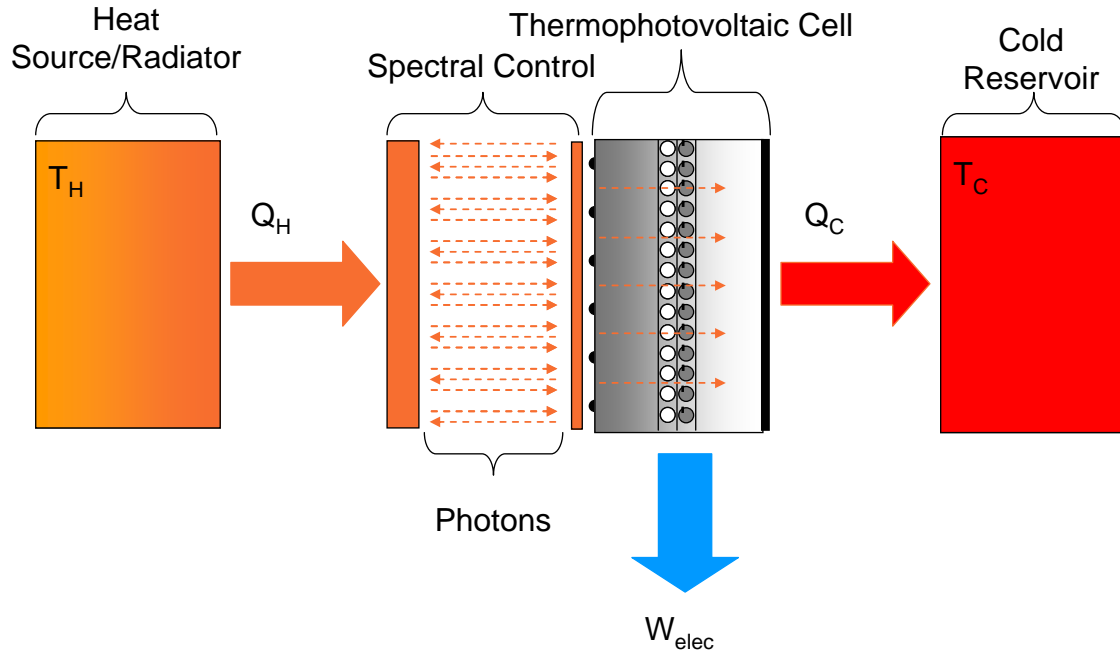
Figure 39.   Components of a TPV System

1.   Heat Source

The heat source contains thermal energy at temperature, T_H, and a radiator to emit photons for conversion. Chemical, solar thermal, and nuclear sources have all been used or considered for TPV applications. The temperature of the heat source is important to system performance because higher efficiencies are generally possible with higher radiator temperatures. The Carnot efficiency of Equation (5) describes this relationship for a generic heat engine. Later chapters illustrate the tradeoffs between heat source radiator temperatures, photovoltaic device efficiency, and the resultant impact of the heat rejection system. The temperature of the nuclear fission reactor heat source in this thesis is primarily limited by the thermal tolerance of fuel materials as mentioned in Chapter II. The specific temperature limits chosen for analysis are detailed in later sections.

2.   Spectral Control

The spectral control components increase system efficiency by ensuring that photons reaching the TPV device have sufficient energy for the photoelectric effect. Recall that photons are required to have energy greater than the semiconductor bandgap

to excite electrons into the conduction band. Designers commonly employ three types of spectral control in TPV systems. Selective emission tailors the output spectrum of the heat source radiator by the use of a selective or filtered radiator. Reflective spectral control places a filter/reflector at the surface of the TPV device. Transmissive spectral control reflects unused photons out of the device and back to the heat source radiator [Ref. 30, pp. 512-513]. The three types of spectral control and the components to implement them are illustrated below in Figure 40. Note that reflective and transmissive spectral controls are similar to recuperation in more conventional heat engines discussed in Chapter II.
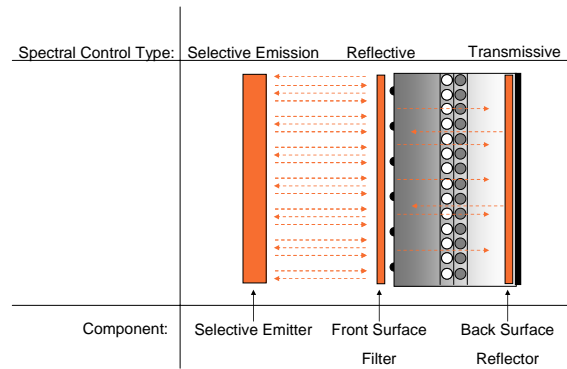
Figure 40.   Spectral Control Methods

Spectral control methods can appear alone or in combination. Choices among them involve design tradeoffs. Selective emission tailors the output spectrum from the heat source radiator at the expense of reducing the overall power transmitted to the photovoltaic cell and the output power of the device. Reflective spectral control does the same thing to a lesser degree because practical filters are imperfect and will absorb some of the light that the photovoltaic cell could have converted into electricity. Transmissive spectral control tends to maximize the output power density of the device because it maximizes input photon flux and only rejects the unused photons. A combination of both reflective and transmissive spectral control promises slighter higher efficiency at the cost of lost output power density [Ref. 30, pp. 512-513].

3.   Thermophotovoltaic Cell

The thermophotovoltaic cell is identical in principle and function to the photovoltaic cell described in Section C above. The term "photovoltaic" is general and

ignores the important question of the spectrum of incident light that the cell coverts to electricity. Thermophotovoltaic cells convert light down into the infrared range of the spectrum. More on the consequences of this appears below in Section E.

4. Cold Reservoir

The cold reservoir of a thermophotovoltaic system maintains the cell at some low temperature, T_C. It performs the same function as the cold reservoir in the heat engine described in Chapter II: it provides the necessary thermal sink to ensure that thermal energy flows through the power converter. Maintaining the cold reservoir temperature is one of the particular challenges of applying TPV to the space power systems described in this thesis. Note that a TPV system in space is likely to have two radiators: one for the heat source mentioned above and another to reject waste heat. The first is known as the heat source radiator and the second simply as the radiator or heat rejection radiator in this thesis.

The ability to tailor a heat source and control the photon spectrum incident on the photovoltaic cell represents an essential difference between the solar photovoltaic and thermophotovoltaic systems. It also adds complexity to the design and construction of the TPV system, particularly the cells themselves. The next section discusses the crucial impact of photon spectrum on photovoltaic device material selection and design.

E. INCIDENT LIGHT SPECTRUM AND MATERIAL CONSIDERATIONS

Preceding paragraphs have only mentioned the spectrum of the incident radiation and its relation to photovoltaic cell performance. The present section describes this in more detail. A photon must carry sufficient energy to excite an electron out of the valence band and into the conduction band to generate charges in a photovoltaic cell. The energy carried by a photon is related to its wavelength through the following relationship.

$$E_\gamma = \frac{hc}{\lambda}$$
$$E_\gamma[ev] = \frac{1.24}{\lambda[\mu m]}$$

(19)

Here, h is Planck's constant (6.626 x 10^{-34} J-s) and c is the speed of light in a vacuum (3 x 10^8 m s^{-1}). The equation is also given in a more convenient form that produces energy in eV when wavelength is provided in microns.

Photons with insufficient energy will not produce the photoelectric effect but they can be absorbed by the lattice or the back surface of the cell. Furthermore any excess energy absorbed by the electron beyond the bandgap energy is generally lost as the unbound electron moves about the lattice. Both of these events cause heating, reduce power density, and decrease cell efficiency.

Picking semiconductor materials with appropriate bandgaps is thus critical to photovoltaic cell design. Bandgap energies of various photovoltaic cell materials and corresponding photon wavelengths appear below in Table 6. Note that a range of bandgaps is often possible by varying the relative concentration of the constituent atoms in compound semiconductors.

Material	E(eV)	λ (µm)
GaAs	1.42	0.87
Si	1.12	1.11
GaSb	0.72	1.72
Ge	0.66	1.88
InGaSb	0.6	2.07
InGaAsSb	0.50-0.74	2.48-1.68
InAsSbP	0.39	3.18

Table 6.   Bandgaps of Semiconductors [after Ref. 31, p. 26]

The bandgaps from Table 6 appear graphically superimposed over blackbody spectra representative of TPV heat source radiator operating temperatures in Figure 41. The arrows in the figure indicate the portion of the photon spectrum that is above the bandgap energy of the indicated material. Only light to the left of the indicated wavelength is convertible in a photovoltaic cell. The blackbody temperatures recall the fuel element temperatures from Table 2 to give some indication of materials which might be chosen for SNRPS application.
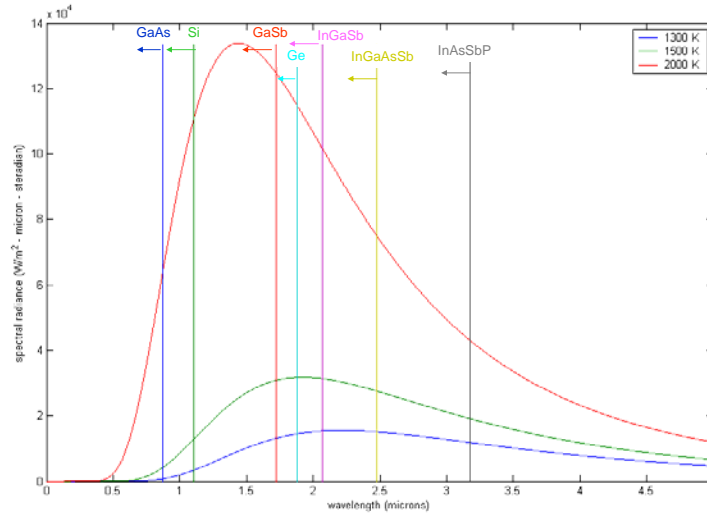
Figure 41.   Blackbody Spectrum vs. Bandgaps from Table 6

The figure gives a general idea of how much light is accessible to a cell made of a given semiconductor material. The table below indicates the fraction of incident light that is available at each of the three blackbody radiator temperatures. These numbers were calculated by integrating the spectral radiance under the blackbody curve up to the bandgap wavelength and dividing through by the total area under the curve as determined by the Stefan-Boltzmann law. Clearly, the use of a low bandgap material and a high temperature heat source radiator make the most light accessible to the TPV power conversion system. Recall, however, that excess energy above the bandgap will contribute to cell heating and decrease performance, and that heat source design considerations may limit the usable outlet temperature.

Material	1300 K	1500 K	2000 K
GaAs	0.1%	0.5%	3.5%
Si	1.0%	2.6%	10.7%
GaSb	11.2%	18.5%3	38.1%5
Ge	15.4%	23.9%	44.6%
InGaSb	20.8%	30.4%	51.6%
InGaAsSb	33.1%	43.8%	64.2%
InAsSbP	51.6%	61.7%	78.1%

Table 7.   Percentage of Incident Light with Energy Greater than Bandgaps from
Table 6

This chapter has introduced the physics of semiconductors, the basic operation of photovoltaic cells, the parts of thermophotovoltaic systems, and the process whereby the incident spectrum drives photovoltaic device material selection. The next chapter expands upon this discussion with a description of the metrics that the TPV community uses to measure performance, a method to predict TPV efficiency, and the current state of the art in TPV device design.

IV. STATE OF THE ART IN THERMOPHOTOVOLTAIC DEVICES

This chapter discusses the measures of effectiveness common in the TPV device community and the present state of the art of this technology. A simple theoretical model to predict efficiency is described and the results compared with the performance of actual devices. This chapter concludes by introducing the monolithic integrated module approach to increase the output power density and efficiency of TPV cells. This approach appears ideal for space nuclear reactor power system application.

A. MEASUREMENTS OF TPV SYSTEM PERFORMANCE

A meaningful attempt to introduce the current state of TPV technology requires an understanding of how the performance of a system is described in the literature. The five standard measures of performance are essentially the same as in the solar photovoltaic community. They are short circuit current, open circuit voltage, fill factor, quantum efficiency, power density, and efficiency.

The operation of a photovoltaic device with an external load is often characterized by a current-voltage curve like the one shown below in Figure 42.
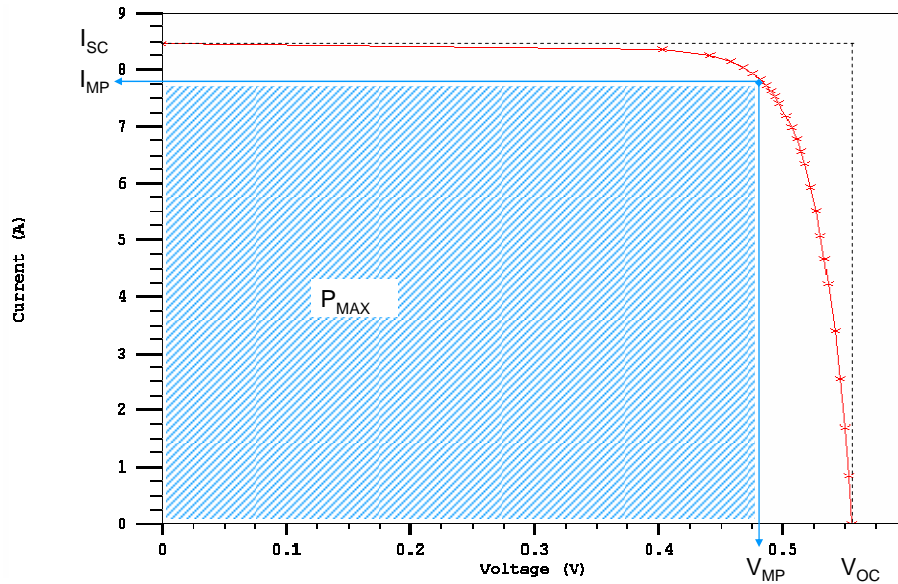
Figure 42.   Simulated I-V Curve for TPV Cell

The short circuit current, I_{SC}, is the current that flows through the cell when it is shorted out. The open circuit voltage, V_{OC}, is the voltage across the cell when there is no current flowing. Of course there is no power being generated by the cell under either of these conditions. One can think of the current as a measure of the number of charges flowing through the external circuit and the voltage across the diode as the average amount of useful work each of those charges does. Both must be non-zero for work to be done. Cell voltage and current will both be less than V_{OC} and I_{SC} during normal operation. The cell will produce maximum power for some voltage and current combination. These are the max power values of voltage and current, V_{MP} and I_{MP}. The blue shaded area on the graph is the maximum power that the cell can output, P_{MAX}. The V_{OC} and I_{SC} define the intercepts of the curve. The fill factor characterizes its shape. Fill factor is the ratio of the maximum output power to the product of the short circuit current and open circuit voltage. It is expressed in percent as defined below.

$$F.F. = 100 \frac{P_{MAX}}{I_{SC}V_{OC}} = 100 \frac{I_{MP}V_{MP}}{I_{SC}V_{OC}} \tag{20}$$

These definitions are identical to those used for solar photovoltaic cells. Also familiar from solar photovoltaics is the quantum efficiency, Q.E. This is defined as the percentage of incident photons that generate an electron-hole pair. Quantum efficiency is not typically a limiting factor in either solar photovoltaic or thermophotovoltaic overall device efficiency [Ref. 32, p. 3322]. Q.E. is a factor in but not to be confused with the device efficiency which is defined as the fraction of total incident photon power converted into electrical power as shown below.

$$\eta_{solar} = \frac{P_{MAX}}{P_{incident}} \tag{21}$$

This definition is similar to the thermal efficiency definition described in Chapter 2 and is based on measured quantities. This efficiency definition is a convenient standard for solar cells because there are materials with band gaps readily suited to the conversion of most of the solar spectrum. The central distinction between solar PV and TPV efficiency descriptions is that a TPV system can and should reflect light back to its heat source while solar cells are unable to do this. Recall from the previous chapter that only 33% of

the light in a 1300 K blackbody spectrum is above the lowest available bandgap in the InGaAsSb material system. This represents an upper limit on device efficiency if the solar cell definition were used. A 25% efficient InGaAsSb cell would produce an overall device efficiency of only 8.3% if efficiency means output electrical power divided by total incident power. Spectral control will attempt to reflect as much of the remaining 67% back to the heat source radiator as possible and the definition of efficiency given in (21) above does not reward that attempt. The TPV community is still in an early stage of development so their definitions are not yet standardized. There is some impetus to establish a standard. The standard TPV efficiency used in this thesis uses the amount of heat actually absorbed in the cell. This definition (shown below) also makes it easier to estimate the amount of waste heat that will need to be transferred to the cold reservoir [Ref. 33, pp. S228-S229].

$$\eta_{TPV} = \frac{P_{elec}}{\dot{Q}_{Abs}} \tag{22}$$

The definition of η_{TPV} carries the important assumption that power returned to the heat source radiator can be recovered and "reused" by the spectral control system. This recuperated power is generally assumed to have the benefit of reducing the power output required by the energy source to heat the radiator and is expected to reduce the power output requirement of the heat source.

B.   RADIATIVE THERMO-CHEMICAL ENGINE TPV MODEL

The analysis of this section closely follows that of Dr. Jeffery Gray and Dr. Ali El-Husseini at Purdue University [Ref. 34], who estimated output power density and TPV efficiency (given by η_{TPV} above) over a heat source temperature range from 1500 to 3000 K. The author coded a version of the model in MATLAB in order to examine a heat source radiator temperature range from 1000-2000 K. This temperature range is of nearer term interest to SNRPS design as described in the Reactor Section of Chapter 2. The model was verified against the case in [Ref. 34] and then run on the new temperatures to provide the figures in the next section. A derivation of the model's governing equations and results of the verification can be found in Appendix A.

65

The model estimates P_{elec} and $\dot{Q}_{Abs}$, using a thermodynamic treatment of the TPV process in which photons are the working fluid. The maximum potential efficiency is then estimated using Equation (22). Recall that the Carnot efficiency of Equation (5) predicts the maximum possible performance for a reversible heat engine operating between two temperatures and that a reversible heat engine is one in which the entropy of the system remains constant. The model presented here represents the next level of realism by assuming that radiative recombination is the limiting loss mechanism in the cell. This means that the cell can be modeled as an endoreversible thermodynamic heat engine. An endoreversible heat engine is an irreversible heat engine in which entropy creation is restricted to transport processes, in this case the exchange of photons between the heat source radiator and the TPV cell [Ref. 36, p. 75]. The model presented here ignores internal resistance losses, non-radiative recombination of electron hole pairs, and a host of material concerns. It thus represents a more realistic limit than the Carnot efficiency but still optimistically predicts TPV performance. The performance of actual TPV systems should be some fraction of that predicted by this model.

The radiative efficiency model below assumes that the heat source radiator and TPV cell are blackbodies emitting at T_H and T_C. Output electrical power is found using Equation (23) below. Note that the first equation generically provides output power for any operating voltage and must be maximized to find the power at V_{MP}.

$$P_{OUT} = \frac{2\pi V q_e}{c^2 h^3}\left[(1-R)\int_{E_L}^{E_H} \frac{E^2 dE}{e^{\frac{E}{kT_H}}-1} - \int_{E_G}^{\infty} \frac{E^2 dE}{e^{\frac{E-V}{kT_c}}-1}\right] \tag{23}$$

$$P_{elec} = P_{OUT}(V_{MP})$$

Where V is the operating voltage of the cell (V), R is reflectivity of any spectral control components employed, F is the view factor to the heat source radiator, E is the photon energy, c is the speed of light, h is Planck's constant, and k is Boltzmann's constant. E_L and E_H are the high and low pass band energies of any spectral control components employed. E_G is the bandgap energy of the semiconductor material.

The heat absorbed by the cell is calculated as the difference between the emitted power of the heat source radiator, P_E, and the power reflected back to it, P_R. A reflection

66

efficiency, β, is the spectral control efficiency. It is the fraction of the light between E_H and E_L that the reflective spectral control components actually send back to the radiator. Perfect spectral control means that the filter reflects 100% of the light outside of its design band back to the radiator. The reflected power equation is structured to model band pass reflective spectral control methods. The relevant equations appear below in (24). The similarity between (24) and (6) is not coincidental. The spectral radiant exitance of a blackbody is the post integration form of the P_E equation expressed with wavelength as the independent variable instead of energy.

$$\dot{Q}_{Abs} = P_E - \beta P_R$$
$$where$$
$$P_E = \frac{2\pi}{c^2 h^3} \int_0^\infty \frac{E^3 dE}{e^{\frac{E}{kT_H}} - 1}$$

$$(24)$$

$$P_R = \frac{2\pi}{c^2 h^3} \left(\int_0^{E_L} \frac{E^3 dE}{e^{\frac{E}{kT_H}} - 1} + R \int_{E_L}^{E_H} \frac{E^3 dE}{e^{\frac{E}{kT_H}} - 1} + \int_{E_L}^\infty \frac{E^3 dE}{e^{\frac{E}{kT_H}} - 1} \right)$$

This equation neglects the radiation emitted by the TPV cells but that contribution is considered negligible in practical TPV systems [Ref. 34, p. 7].

C.   MODEL IMPLICATIONS FOR CELL DESIGN

The consequences of the radiative efficiency model drive cell designs to an optimum bandgap for a given heat source radiator temperature and spectral control efficiency. This section examines the progression for a TPV system with no spectral control, to one that reflects 100% of below-bandgap photons back to the radiator, and ending with a more practical one that only reflects some fraction of below-bandgap photons. The results in this section are for the temperature range from 1000-2000 K and cover the bandgap range defined by the materials in Table 6. All cells in the examples below are maintained at 300 K unless otherwise stated. Note also that this section uses the TPV efficiency definition of (22) because the reflected energy is assumed to be recuperated.

We begin with a TPV system that has no spectral control. Efficiency and output power plots appear below in Figure 43.
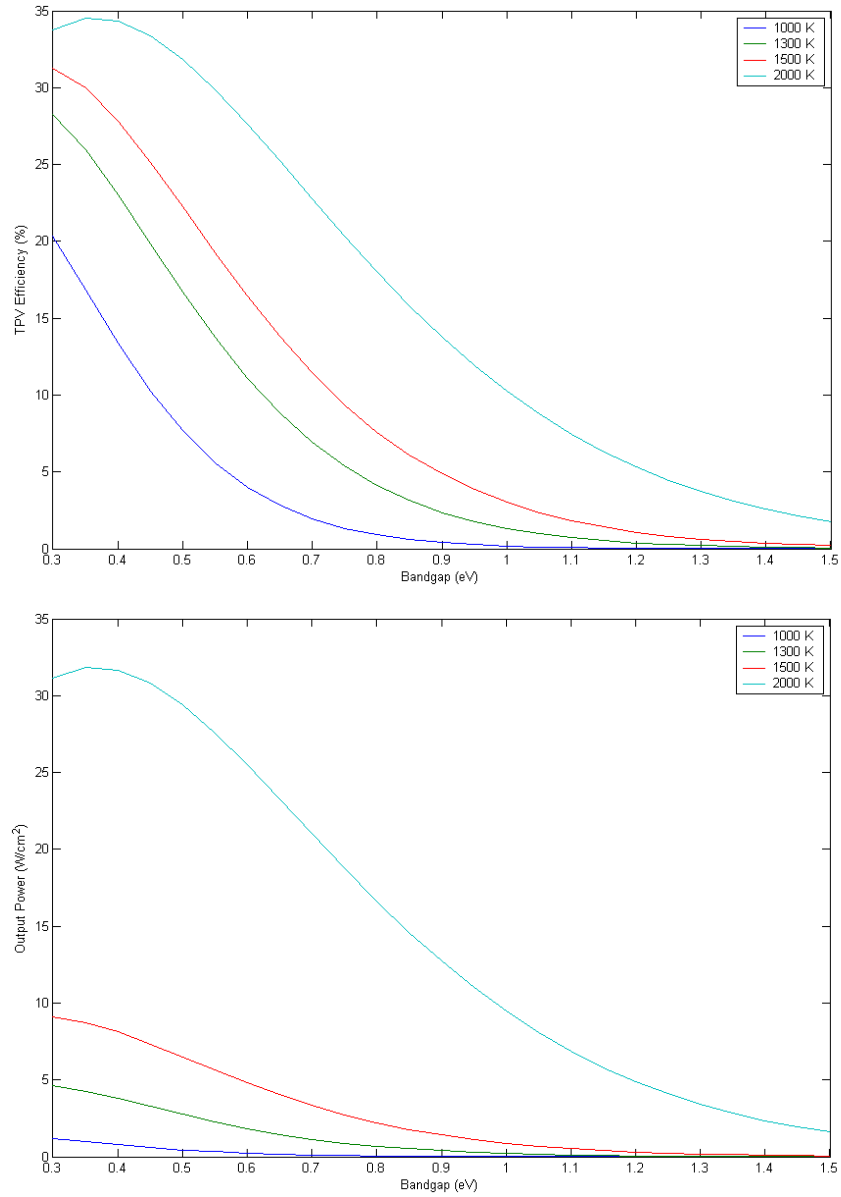
Figure 43.   TPV Efficiency and Output Power for 300 K Cell with No Spectral
Control

The model predicts maximum efficiency and output power at the lowest bandgap.
This is unremarkable and consistent with the increase in available light for conversion at
a given temperature made possible by a lower bandgap as illustrated previously.

Efficiency can be improved by adding reflective spectral control below the bandgap energy. The graphs below represent the performance of a TPV system in which 100% of the light that is below the bandgap is reflected back to the heat source radiator and recuperated.
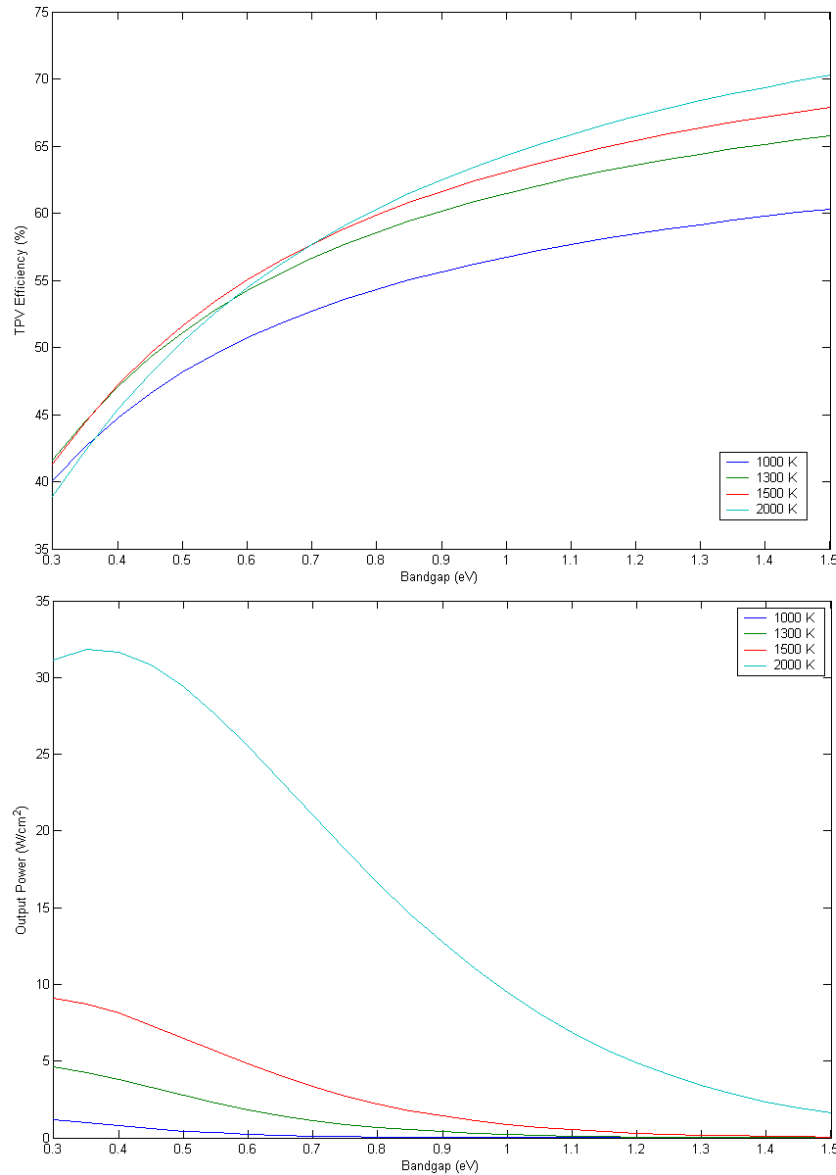
Figure 44.　　　TPV Efficiency and Output Power for 300 K Cell with Perfect Spectral Control

Note that the efficiency curve is monotonically increasing and favors high bandgap cells. The power output curve is unchanged, however, so the price of high

69

efficiency is lower power density. Higher efficiencies may theoretically be possible with higher bandgap cells and perfectly reflective spectral control but real systems will have imperfectly reflective spectral control. The effect of imperfect reflective spectral control efficiency, modeled here by setting β to 75 %, is illustrated below in Figure 45.
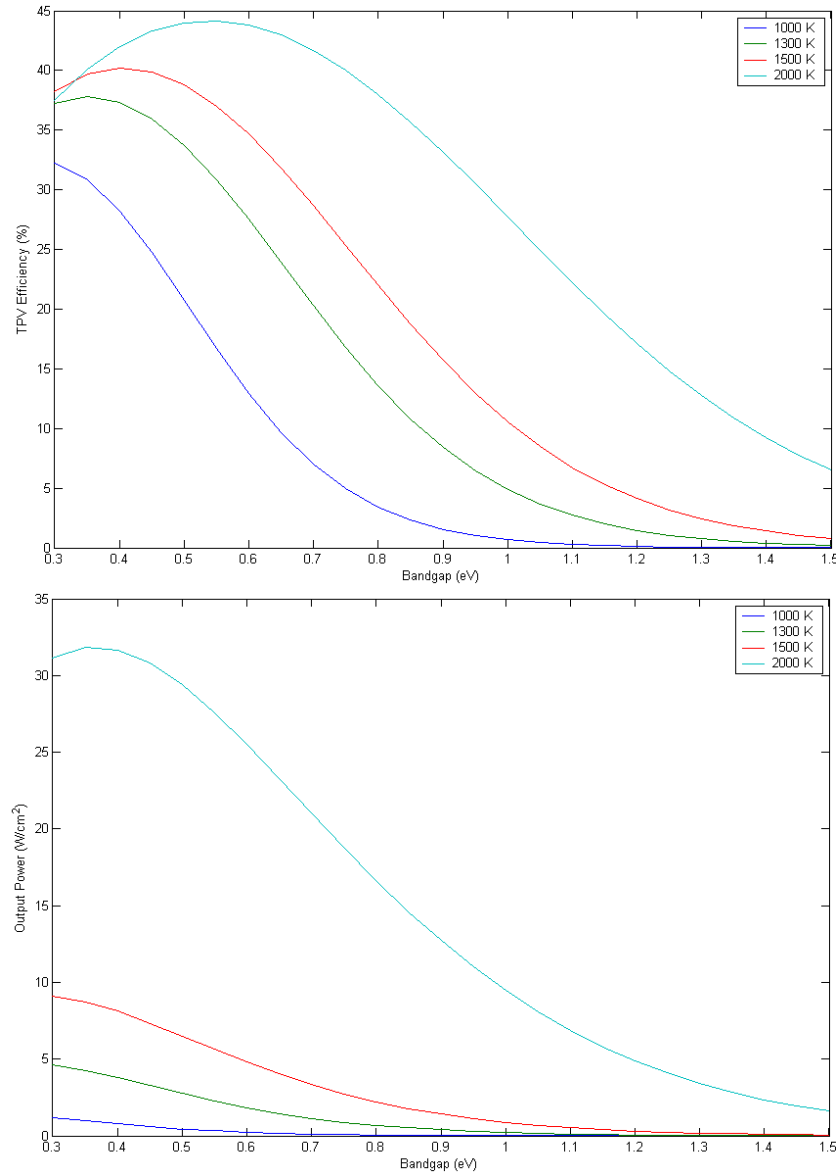
Figure 45.   TPV Efficiency and Output Power for 300 K Cell and Imperfect Spectral Control.

It is clear that an optimum bandgap exists to maximize the TPV system efficiency when spectral control is imperfect. Note that the efficiency maximum does not correspond to

the output power maximum. This implies that a range of bandgaps will be required to meet different efficiency and output power requirements.

The efficiency curves above show the case where the spectral control reflects 75% of the light back the heat source radiator. It is reasonable to examine how the efficiency curve varies with spectral control efficiency. This analysis appears below in Figure 46. The efficiency curves represent TPV efficiency for beta values from 70 to 100% for a 1300 K heat source radiator.
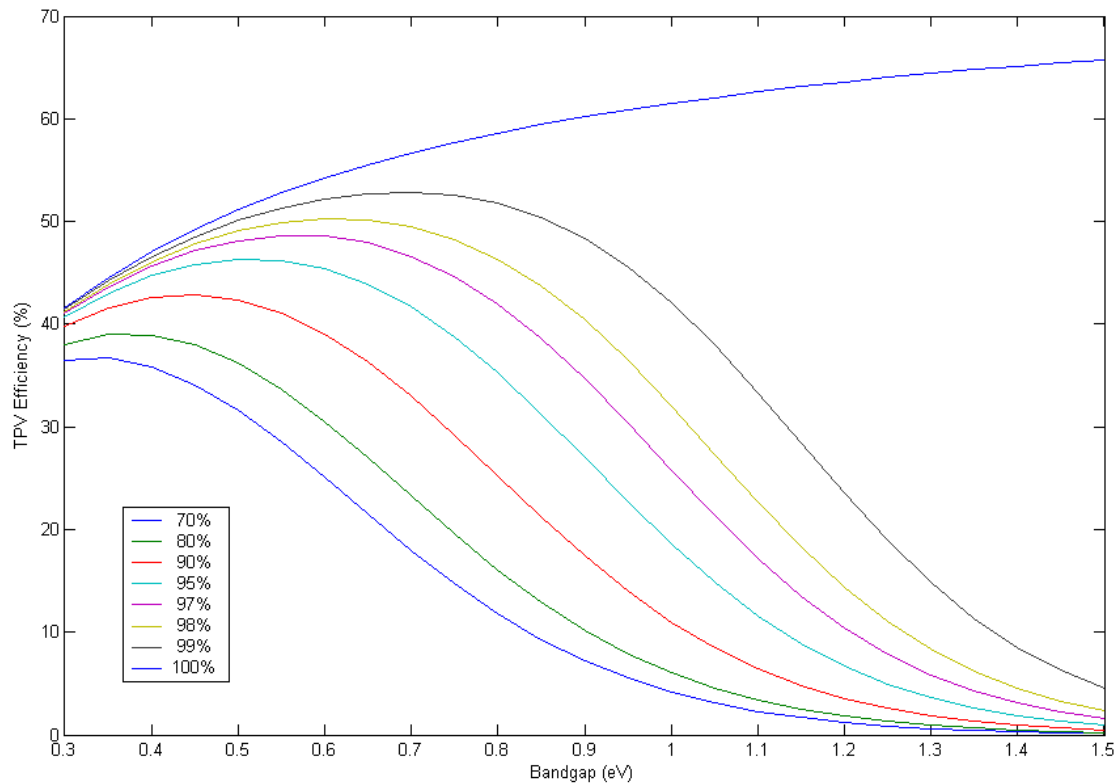
Figure 46.   TPV Efficiency with 1300 K Radiator, 300 K Cell and Varying Spectral Control Efficiencies

The figure makes it apparent that small changes in spectral control efficiency can dominate overall device efficiency. Even a 1% variation from perfect reflection greatly reduces device efficiency because of the large fractional increase in input power. The efficiency maxima occur in a bandgap range from 0.35 to 0.7 eV. Note that increasing spectral control efficiency moves the efficiency maxima to higher values at higher bandgaps.

The expected behavior of a TPV device at various cell operating temperatures is of particular interest in assessing the technology for SNRPS application. A plot of TPV efficiency vs. device temperature for a 0.6 eV bandgap and 70% efficient spectral control appears below in Figure 47.
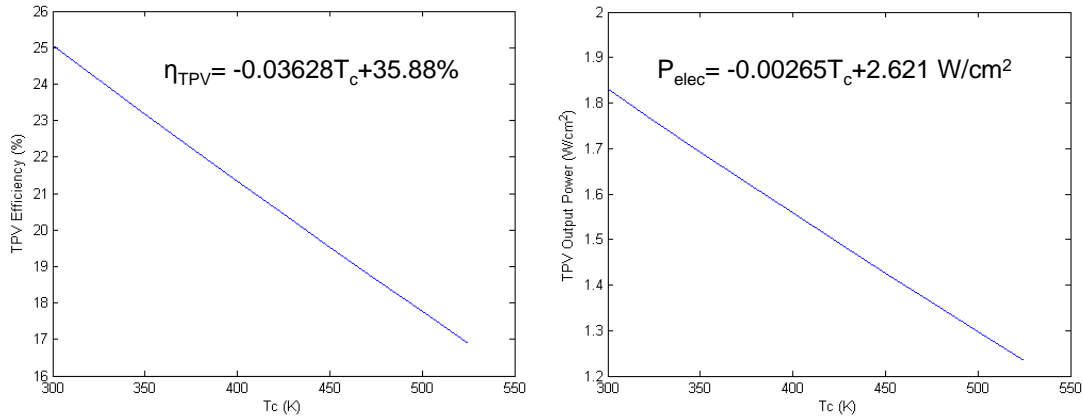
Figure 47.   Theoretical Device Performance vs. Temperature for 1300 K Heat Source Radiator, 0.6 eV Bandgap and 70% Efficient Spectral Control

The model predicts linear degradation of TPV cell performance over the range of operating temperatures from 300 to 525 K to a root-mean-square fit error of 0.04% for efficiency and 0.27% for power density. Later sections demonstrate that real devices exhibit linear behavior in the laboratory, though with steeper slopes.

D.   EXISTING CELL DESIGNS

TPV development efforts have, until recently, focused on cell and filter optical component designs. This has started to change within the last two years with several groups calling for increases in overall system testing. The technology development risk associated with TPV is still considered moderate to high [Ref. 35, p. 3]. A great deal of filter and cell development has taken place, however. Much of this development effort centers on relatively low power 0.5 to 1 kW military and commercial portable power generation activities.

A number of semiconductor materials have bandgaps in the range required by TPV devices. The band gaps accessible and lattice constants with various compound semiconductors appear below in Figure 48.
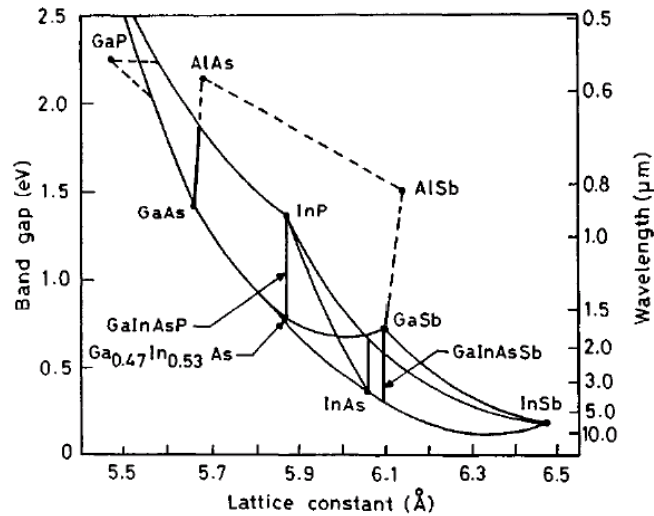
Figure 48.   Bandgap Energy vs. Lattice Constant for Various Compound
Semiconductors [from Ref. 37, p. 5822]

The green shaded area represents the bandgap range of the previous plots, 0.3-1.5 eV. GaSb, InGaAsSb, InGaSb, InAsSbP and Ge have all been used in TPV devices [Ref. 38, p. 434]. Note that a wide variety of bandgaps are available within a relatively narrow range of lattice constants. The lattice constant gives some idea of how difficult it will be to grow layers of each material onto a substrate. Additionally GaSb and InP are commercially available substrates for the construction of semiconductor devices [Ref. 30, p.512]. The different layers required by a cell structure can be applied using technologies familiar from the semiconductor industry, for instance metal organic vapor phase epitaxy (MOVPE) or vapor phase diffusion. MOVPE produces more complicated structures and appears to deliver slightly superior performance but the diffusion process is simpler and presumably cheaper to implement [Ref. 39, p. 285].

1.   Single Junction Cells

Photovoltaic cells are often classified by the number of p-n junctions present. Most TPV devices fabricated at the time of this writing have had a single junction. A single junction TPV cell must contain, at a minimum, all the features previously shown in Figure 38. These are a p-n junction and electrical contacts at the front and rear surfaces to collect charges and pass them to an external circuit. A practical single junction cell appears below in Figure 49.

73
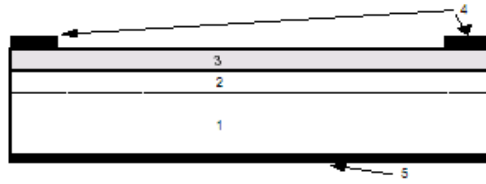
Figure 49.   Practical Single Junction TPV Cell [from Ref. 38, p. 435]

Region 1 in this device is the substrate upon which it is grown. This substrate also acts in some cases as the base (current collector). Region 2 is the base where distinct from region 1. Region 3 is an emitter, which is diffused into the device. Regions 4 and 5 are front and back contacts. This figure is from a study which illustrates the relative performance characteristics of simple single junction TPV devices made with diffused emitters from a variety of materials. The bandgaps chosen were 0.72eV (GaSb), 0.66 (Ge), 0.6eV (InGaSb), 0.55eV (InGaAsSb), and 0.39eV (InAsSbP). Details on the materials utilized appear below in Table 8.

Part of the cell	GaSb-cell	InGaSb-cell	InGaAsSb-cell	InAsSbP-cell	Ge-cell
1. Substrate	n-GaSb single and polycrystal.	n-InGaSb polycrystalline	n-GaSb single crystal	n-InAs single crystal	p-Ge single crystal
2. Epitaxial base	none	none	n-InGaAsSb	n-InAsSbP	none
3. Diffused emitter	p-GaSb	p-InGaSb	p-InGaAsSb	p-InAsSbP	n-Ge
4. Front side contact	Ti/Ni/Au				Ni/Au-Ge
5. Backside contact	Au-Ge				Ti/Pd/Ag

Table 8.   Materials Used for Regions in TPV Cells [from Ref. 38, p. 435]

The purpose of the study was to identify a TPV material to replace GaSb structures in "low temperature" (T_H<1273 K) applications by comparing the performance of different cells. These cells were tested under the NASA Jet Propulsion Laboratory's Large Area Pulsed Solar Simulator (LAPSS). This simulator does not produce a blackbody spectrum so output power densities are not readily comparable to the radiative efficiency model described above. The results of the illumination tests do, however, provide representative performance figures for actual TPV devices. They appear below in Figure 50. [Ref. 38, pp.436-438]

74
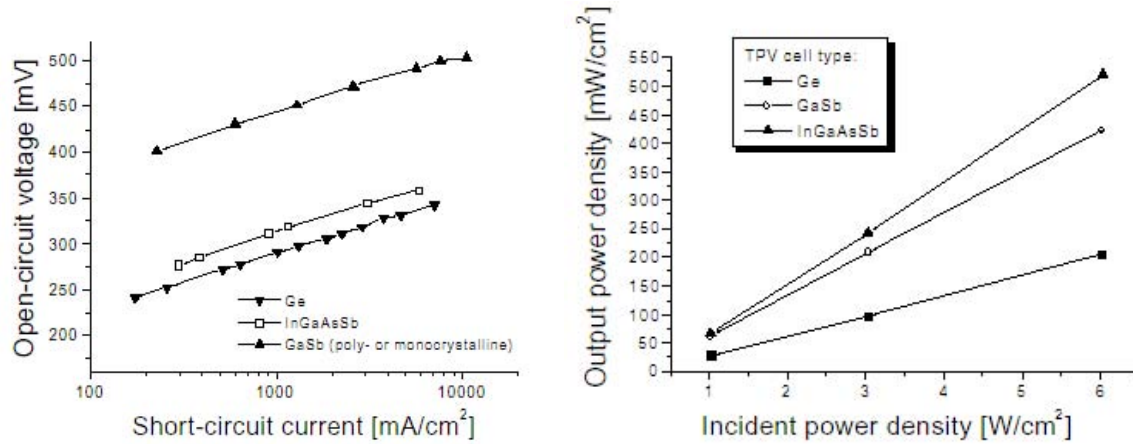
Figure 50. V_{OC} vs. I_{SC} and Output vs. Input Power Density(T_C=298 K) [from Ref 38, p. 438]

Note the relative performance of the InGaAsSb and GaSb cells. The lower bandgap InGaAsSb cells produce more output power than the popular GaSb cells but at a lower open circuit voltage. This is expected because the open circuit voltage across an illuminated p-n junction is ultimately limited by the contact potential at the junction, as described in the previous chapter. Conversion of lower energy photons produces lower open circuit voltage across the junction. Lower voltages in DC systems mean that higher currents must be applied to achieve a give power level. High currents mean higher I^2R losses that lead to lower efficiencies and power densities.

2.   Monolithic Integrated Modules

The use of monolithic integrated modules (MIMs) can overcome the issues that result from low devices output voltages. A MIM consists of a number of small series interconnected photovoltaic diodes grown on the same insulating substrate. These devices have a number of advantages. The first is that the series interconnected diodes sum their voltages at the device terminals. Output voltages are commonly ~10V because large numbers of small diodes are packed onto a given surface area. Compare this to the fractional volts from the single junction devices described above. Another advantage is the potential for greater redundancy. The diodes can be arranged in a variety of series/parallel configurations which reduce the consequences of single cell failure. This is akin to familiar solar array design philosophy. Indeed, a MIM can be thought of as an array on a chip. The use of a non-conducting substrate means that the device can

75

theoretically be mounted directly to the cooling apparatus thereby simplifying system design and construction. Finally, proper choice of substrate materials produces integrated spectral control structures which can dramatically increase device efficiency. [Ref. 40, p. 414-415]

The Solid State Electronic Materials group at Bechtel Bettis, Inc., in West Mifflin, PA, is working on TPV MIMs that may be applicable to space nuclear power systems in the hundred kilowatt electrical range. After several iterations of device design, the group reported on a TPV MIM with 20% efficiency in 2003 and achieved higher efficiencies through improved spectral control in 2004 [Refs 30 and 40]. This MIM is offered here as a prototype for later consideration. It is also an example of the tradeoffs involved in TPV design and the complex structures that result. Consider first a single diode from the MIM as it appears below in Figure 51.

| Si₃N₄ Anti-Reflection Coating |
| n InPAs Contact/Window |
| n+ InGaAs Emitter |
| p InGaAs Base |
| p InPAs Back Surface Field |
| p++ InGaAs Tunnel Junction |
| n++ InGaAs Tunnel Junction |
| n+ InPAs Lateral Conduction/Buffer |
| Semi-insulating InP Substrate |
| Si₃N₄ Reflector |
| Gold Back Surface Reflector |

Figure 51.   Cross Section of Single Diode from Bettis TPV MIM [from Ref. 40, p. 415]

Light enters from the top of the figure. The Si_3N_4 coating suppresses reflection at the surface and allows the light into the device. Note that this anti-reflection coating is the extent of the front surface spectral control in this device. The power producing portion of the device is a double heterostructure (DH) cell with a 0.6 eV bandgap InGaAs compound semiconductor single junction diode as the active layer. The double heterostructure is formed by surrounding the active layer with doped InPAs layers. They

76

serve to increase efficiency by reducing recombination of minority charge carriers at junction surfaces. The top n-doped InPAs layer also acts as the top contact of the diode. This structure is connected to another InPAs layer with an InGaAs tunnel junction (TJ). The tunnel junction is a highly doped layer which allows current to flow between the adjacent semiconductor layers with minimum voltage loss. This lowest InPAs layer is n-doped to increase its mobility and allow it to act as a lateral conduction layer between this diode and adjacent ones. This lateral conduction layer has a graded composition to permit growth of the InGaAs active material on top of the lattice mis-matched InP substrate. InP is insulating so that current is confined to the n-doped InPAs lateral conduction layer above it. InP is also largely transparent to the wavelengths of interest so that photons will pass through the substrate and reflect off of the gold back surface reflector. The Si_3N_4 preserves the polish on the back surface reflector by preventing the gold from diffusing into the InP. [Ref. 40, pp.415-416]

The double heterostructure device described above must be connected in series with similar devices to complete the MIM. The method for doing this appears below in Figure 52.
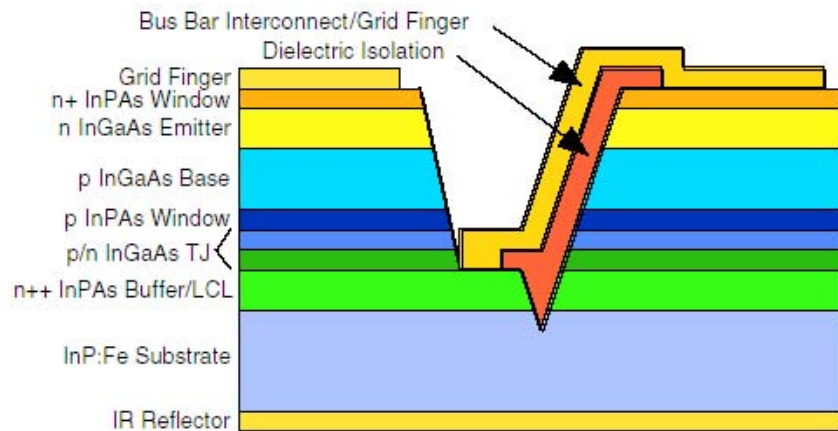
Figure 52.   Cross Sectional View of DH Cell Structure Showing Connection to Adjacent Cell [from Ref. 41, p. S212]

The figure shows how an etched groove down to the lateral conduction layer (LCL) allows a bus bar to run from the conduction layer of the left cell to the top contact of the right cell. This bus bar region is coated with gold reflective coating because

simulation showed that device performance degraded when light was allowed into the side of the junction. Experiment has shown that this gold coating improves performance. [Ref. 41, p. S211]

The Bettis group connected thirty of the cells described above in series. The edges of the cell contain bus bars to allow connection to other MIMs in a large array as shown below in Figure 53.
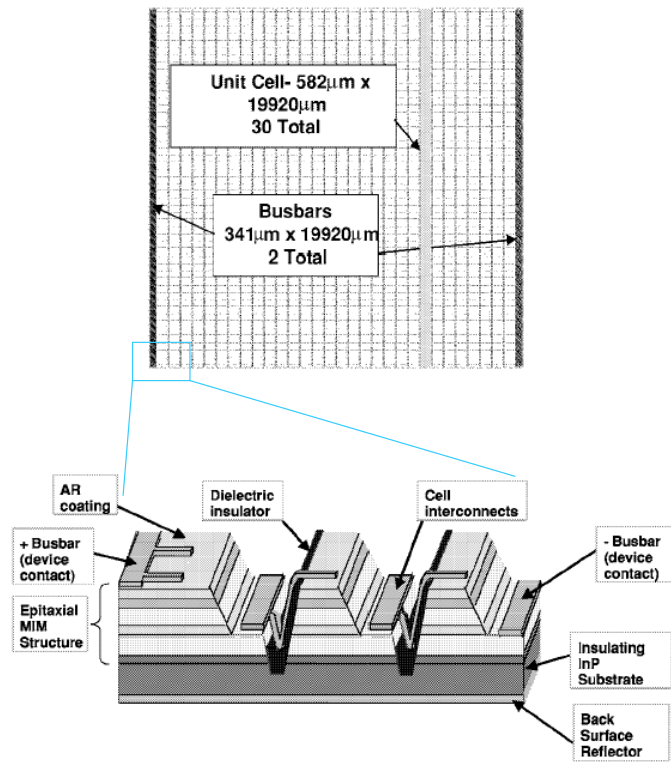
Figure 53.   Layout of 2cm x 2cm Bettis MIM with Exploded View Showing Cell Connection to Device Bus Bars [from Ref. 40, p. 417]

The Bettis MIM described above has the best performance for application in large high power arrays of any device surveyed. The 4 cm^2 MIM produced 0.90 W/cm^2 under 1331 K silicon carbide heat source radiator illumination with the device temperature held at 301 K (27.6°C). Device efficiency was 20.6%. Recall that the radiative model described earlier predicted ~1.8 W/cm^2 and 25% efficiency for a TPV cell operating under similar conditions with 70% spectral control efficiency. Note that the silicon carbide radiator was a gray body which tends to maximize power density at the expense

of efficiency. Bettis achieved higher efficiency in 2004 by adding a front surface filter for improved spectral control [Ref. 41, p. S212]. The performance of both devices appears below in Figure 54. The cells in both of these figures are at about 300 K.
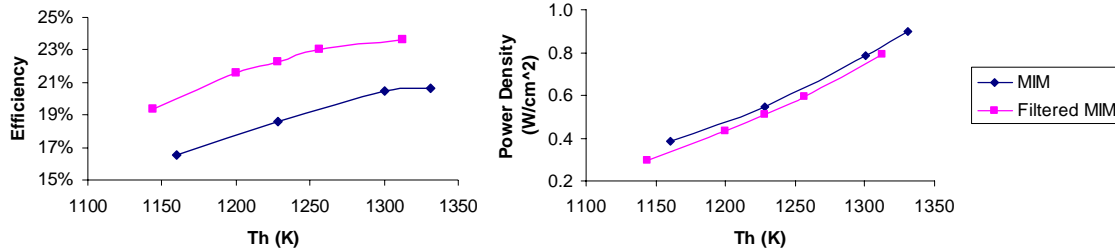
Figure 54.　　　Performance of Bettis MIM (with and without filter) [after Ref. 30, p. 513]

　　　Note that the filtered cell achieves higher efficiency at the price of slightly lower power density. Recall that the reason for this is that real filters absorb some of the incident in-band light which lowers the number of charge carriers produced in the cell.

　　　Comparison of this data to the radiative efficiency model presented earlier is difficult because the emissivity of the gray body SiC heat source radiator used in the tests is not available. The emissivity is a function of wavelength (photon energy) and varies significantly from the blackbody ideal. This is an issue because it decreases the expected output power calculation significantly and effects the efficiency prediction in uncertain ways. However the comparison gives some indication of the validity of the model. The predicted vs. actual efficiencies for the MIM and a 0.6 eV endoreversible TPV diode with 60% efficient spectral control appear below in Figure 55. Note that the model assumes an average emissivity of 0.5 as an approximation from the SiC radiator from [Ref. 42, p.25].
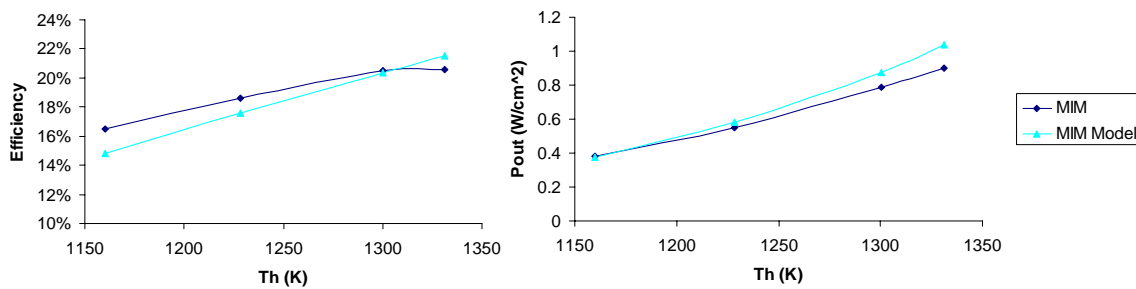
Figure 55.　　　Predicted and Measured Performance of Unfiltered MIM

The comparison between the filtered MIM and a 0.6 eV endoreversible TPV diode with 70% efficient spectral control appears below in Figure 56.
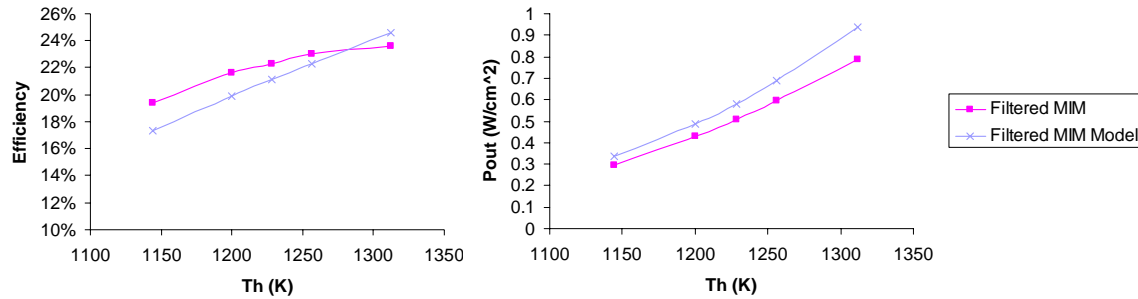
Figure 56.   Predicted and Measured Performance of Filtered MIM

Surprisingly, the model tends to under-predict the efficiency of the device for both the filtered and unfiltered cases. This is attributed to the speculative nature of the emissivity approximation. The model appears to consistently predict filtered MIM efficiency with an average error of 5% (relative). It also consistently under predicts filtered MIM output power density with an average error of 15% (relative). This is partly due to the fact that absorption in the filter is not accounted for in the model. This thesis is primarily concerned about efficiency because that it has multiple effects throughout the power system. Output power density is less important to the present work because it primarily affects only the required heat source radiator/TPV module area. These areas and masses are not likely to be driving factors in nuclear space power systems because the reactor, shield, and heat rejection radiator masses have consistently been much larger than power conversion system masses.

The relationship between device performance and operating temperature determines the cooling power required and is a major driver in system design. Recall that the output power density and efficiency are expected to decrease linearly as shown above in Figure 47. The observed behavior of the filtered and unfiltered Bettis MIMs confirms this expectation as shown below in Figure 57.

80
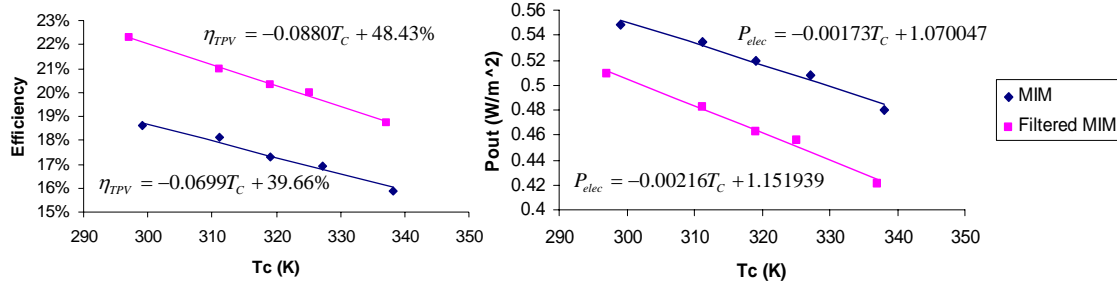
Figure 57.   Measured MIM Performance with T_C (T_H=1300K) [after Ref. 30, p. 513]

The filtered MIM's performance falls off more rapidly with temperature than the unfiltered MIM. The filter cutoff wavelength was set by design and is independent of temperature. The MIM's bandgap changes with temperature, however. A less sensitive filter should be possible if it is designed for the desired operating temperature [Ref. 30, pp. 514-515]. The slope of the efficiency vs. T_C curve is particularly important in sizing heat rejection radiators as will be discussed later.

This chapter has presented a model which enables a designer to make rough estimates of TPV parameters for use in system design. Most significantly, the model shows the critical role that spectral control efficiency plays in determining overall TPV efficiency. That efficiency is crucial to any benefit TPV will bring to a SNRPS. This chapter has also given samples of the state of the art in TPV device fabrication and compared them to the results of the theory. Of these, MIM technology offers the promise of a highly efficient, high voltage, and reliable building block for the production of TPV power conversion arrays. Significantly, these devices may themselves be interconnected to produce high voltage DC power straight off of such an array. The next chapter assesses the impact of using the Bettis MIMs for power conversion with an SP-100 class reactor heat source.

THIS PAGE INTENTIONALLY LEFT BLANK

V. ASSESSMENT

Thermophotovoltaic cells promise attractively high efficiencies, direct energy conversion with no moving parts, and increased modularity in construction. Additionally, TPV offers the potential to eliminate secondary pumped thermal transport loops by direct attachment to heat pipe radiator elements and the potential for direct conversion of heat to high DC voltage electrical power required by advanced electric thrusters by building arrays of monolithic interconnected modules. These are enticing capabilities. These assets are counterbalanced from the technical standpoint by lower operating temperature tolerances. A decision to explore TPV for SNRPS application rests of an assessment of these potential benefits versus the costs. Any such assessment must quantify effects on system parameters. Efficiency alone is an insufficient metric. This study focuses on the overall system mass and radiator area. TPV power conversion has something to offer an SNRPS if the overall system mass can be reduced at an acceptable cost in radiator area.

A. METHODOLOGY

The basic approach is to use the SP-100 as a baseline and assess the impact of replacing the thermo electric power conversion and heat rejection systems described in Chapter II with TPV converters with directly coupled heat pipe radiators. This approach is chosen because the SP-100 program reached a high level of nuclear system development. Nuclear component development and testing is widely regarded as the most expensive part of a reactor program [Ref. 43, p. 824]. Use of preexisting SP-100 experience is thus expected to reduce overall system development cost. This first assessment uses the published information on the Bettis MIM from the previous chapter with extrapolations into the device operating temperature regions of interest.

The developmental status of TPV technology forces significant assumptions to be made. These are enumerated and justified as required in the "Methodology" section below. Subsequent sections describe the results obtained and preliminary analysis on trends observed. Significant numbers assumed in the analysis appear below in Table 9.

Parameter	Value
Electric Power	100 kWe
Reactor Outlet Temperature	1300 K
Space Sink Temperature	200 K
Radiator Emissivity	0.85
Radiator Specific Mass	4.67 kg/m^2

Table 9.   Numerical Values Used for Analysis

The reactor outlet temperature is slightly lower that which SP-100 delivered to its thermoelectric converters (~1369 K) to account for an increased temperature loss between the reactor and heat source radiator. This value was also attractive because previous TPV simulation work conducted at Naval Postgraduate School examined this temperature range [Ref. 31]. The emissivity selected is the lifetime emissivity requirement for the SP-100 heat pipes and the specific mass of a single sided heat pipe radiator is from [Ref. 44]. This analysis also assumes that the power conversion thermal efficiency given by Equation (4) is dominated by the TPV system efficiency given in Equation(22). This is consistent with flat plate heat source radiators optically coupled to arrays of TPV devices and relatively close spacing (~cm's) common in TPV systems.

An Excel™ model was written which analyzes TPV efficiency vs. radiator temperature for the given power level and determines required input thermal power from the reactor and rejected thermal power load on the radiator. The model uses reactor thermal power to estimate reactor and shield mass. It uses rejected thermal power to estimate radiator area and mass. The individual masses are then combined with the masses of other components of the SP-100 system to get an estimate of the total mass of the power system after replacing the thermoelectrics with TPV and allowing the changes in rejected thermal power and required input power to work their way through the

system. Table 10 below indicates subsystem component masses of the SP-100 power system and which ones are affected by this assessment.

Subsystem (* indicates that mass varies with rejection temperature in the model)	SP-100 Mass (kg)
Reactor *	700
Primary Heat Transport*	500
Shield*	1000
Power Conversion*	370
Heat Rejection*	850
Power Management and Distribution	390
Reactor Control and Instrumentation	290
Structural/Mechanical	480
Total*	4580

Table 10.   SP-100 Subsystem Masses [Ref. 44, p. 3-5]

1.   Estimating Effect on Reactor Mass

A significant benefit of TPV conversion technology is the relative ease of recuperation. The energy which spectral control reflects back to the heat source radiator is not lost to space and represents a considerable amount of power that the reactor heat source does not have to make up. The net effect of this is to reduce the amount of thermal power required of the reactor to the amount of energy absorbed in the TPV device divided by the thermal transport efficiency of reactor thermal power to the heat source radiator as shown below in Equation(25). Transfer efficiency is estimated from the available SP-100 data as 98%.

$$P_{Rx} = \frac{\dot{Q}_{Abs}}{\eta_{Trans}}$$
(25)

The reduction in reactor thermal power is assumed to translate directly into a less massive reactor and primary heat transport system. Reactor mass is assumed to vary according to an empirical relationship for fast reactor mass vs. thermal power from [Ref. 11, p. 62].

$$m_{reactor}[kg] = 132 \ln \left(P_{Rx,Th} \left[kW_{th} \right] \right) - 325 \tag{26}$$

The primary heat transport system was assumed to vary linearly in mass with system thermal power. Design data for the SP-100 indicates a specific mass for the primary heat transport system of approximately 0.2 kg/kW$_{th}$. This estimate includes reactor, fuel, piping, control rods, pumps, gas separators, accumulators, re-entry shield and thaw heat piping. The final equation for reactor mass estimation appears below.

$$m_{reactor}[kg] = 132 \ln \left(\frac{\dot{Q}_{Abs} \left[kW_{th} \right]}{\eta_{Trans}} \right) - 325 + 0.2 \frac{\dot{Q}_{Abs} \left[kW_{th} \right]}{\eta_{Trans}} \tag{27}$$

2.   Estimating Effect on Shield Mass

The shield mass is assumed to scale with reactor thermal power according the following relation given in [Ref. 11, p. 70].

$$m_{shield} \left[kg \right] = 26.5 \left(P_{Rx} \left[kW_{th} \right] \right)^{0.461} \tag{28}$$

This relationship was derived during studies of scaling the SP-100 heat source to a variety of output power levels between 100 kW$_{th}$ and 10 MW$_{th}$. It assumes a seven year mission life, a 34° shield cone angle, a 20 m separation boom, and the same EOL radiation dose at the end of that boom.

3.   Estimating TPV and Heat Rejection Radiator Area and Mass

The relationship between the power conversion system efficiency and radiator mass is a function of the power conversion device operating temperature. This thesis assumes that the device operating temperature is equivalent to the radiator temperature, a simplification justified by the use of heat pipe radiators with low temperature drops across their lengths. The heat that must be rejected for a given power level is related to the system efficiency by

$$\dot{Q}_{Rad} = \dot{Q}_{Abs} - P_{elec} = P_{elec}\left(\frac{1}{\eta_{TPV}} - 1\right) \qquad (29)$$

A higher operating temperature for the power conversion system will generally shrink the radiator area but decrease the device operating efficiency by making fewer states available for energy conversion activities. Decreasing efficiency means that the amount of waste heat goes up and this increases the required radiator area. The balance between these two expressions is expected to produce a minimum heat rejection radiator area for a given output electrical power, a constant hot side temperature, and a given TPV temperature/efficiency relationship. An expression for radiator area in terms of electrical power output and TPV efficiency is obtained by substitution into (11)

$$A_{rad} = \frac{P_{elec}\left(\dfrac{1}{\eta_{TPV}\left(T_{rad}\right)} - 1\right)}{F\varepsilon\sigma(T_{rad}^4 - T_{\sin k}^4)} \qquad (30)$$

This equation produces an estimate of the required radiator area for a given output electrical power. A unity view factor, F, results in an estimate of total radiating surface area required. The specific mass of the SP-100 heat pipe radiator is used to estimate the required mass, assuming heat pipe radiators with the evaporator sections in direct thermal contact with the TPV cells and in the same conical configuration as the reference radiator. This arrangement assumes that the secondary lithium coolant loop of the SP-100 can be avoided in a modular TPV system. This mass savings is expected to offset the increased radiator area required by the lower heat rejection temperature required by TPV systems.

Equation (30) makes the temperature dependence of η_{TPV} explicit and includes the assumption that device operating temperature is equal to the radiator temperature. The relationship between efficiency and temperature is the basis for selecting a device operating temperature and radiator area. Recall that this relationship is expected to be roughly linear for a MIM with imperfect spectral control as demonstrated in the previous chapter.

This analysis uses the data for the Bettis MIM published in [Ref. 30] to establish $\eta_{TPV}(T_{rad})$. These data must undergo significant extrapolation to be useable at the desired device operating temperature range. These extrapolations are acknowledged as the largest assumptions in this analysis. First, the heat source radiator in the published data is at 1228 K. Linear interpolation between the published efficiency data shifts the intercepts up to those characterized by the filtered and unfiltered MIMs published performance at 1300 K. Second, this analysis assumes that the dependence remains linear past the range of temperature data actually taken. The published data is linear up to 338 K. This analysis assumes that the slope of that line extends out to 500 K. The published and extrapolated data appear below in Figure 58.
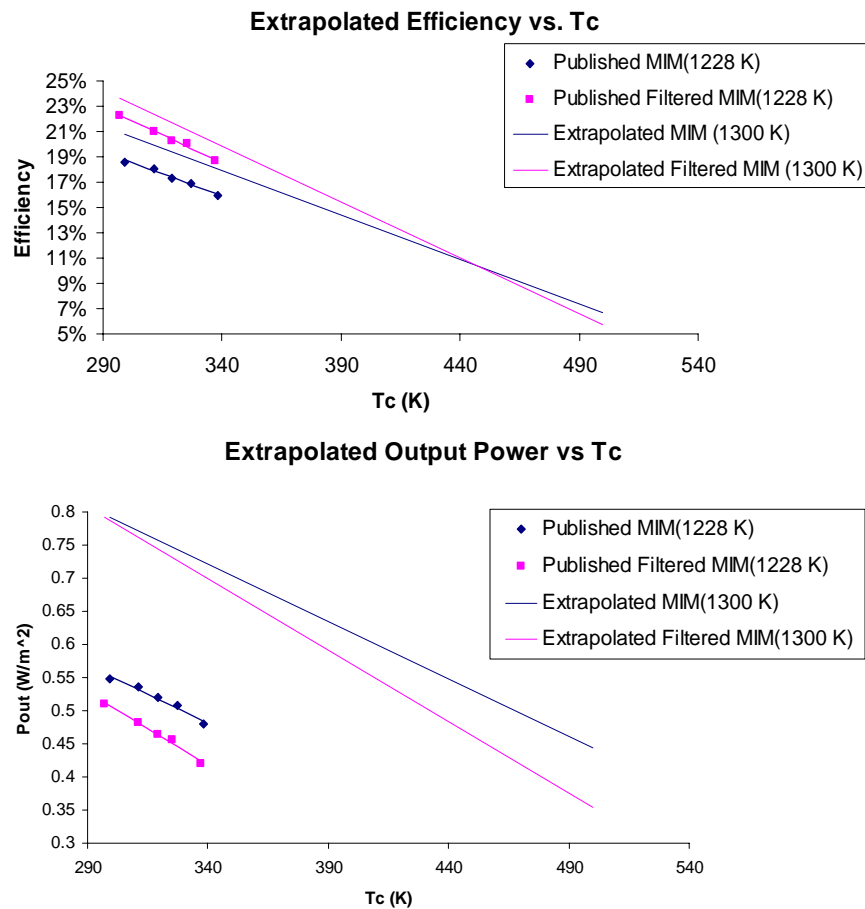
Figure 58.   Published (T_H=1228K) and Extrapolated (T_H=1300K) Efficiency and Output Power Density for Bettis MIM [after Ref. 30.]

Note that the effect of the filter temperature mismatch is represented in these figures by the steeper slope of the filtered-MIM performance lines. This was done to obtain a conservative estimate. Later estimates will assume that the filtered MIM's temperature performance can be made at least as good as the unfiltered.

The area of TPV required for a given electrical power is calculated as a function of the extrapolated power density above. The mass of a large TPV array had to be estimated because there is no indication in the literature that anyone has ever built one. It is assumed that the primary mass of a TPV array will be the structure, not the TPV cells. This thesis therefore uses the specific mass of a Spectrolab triple junction solar array panel with a 6 mil coverslide, 2.36 kg/m^2 [Ref. 45]. The heat source radiator is assumed to be a finned jacket on the primary coolant piping with a specific mass equal to the heat rejection radiator's specific mass.

B. RESULTS

The results of the optimization for both the filtered and un-filtered MIM appear below in Figure 59.
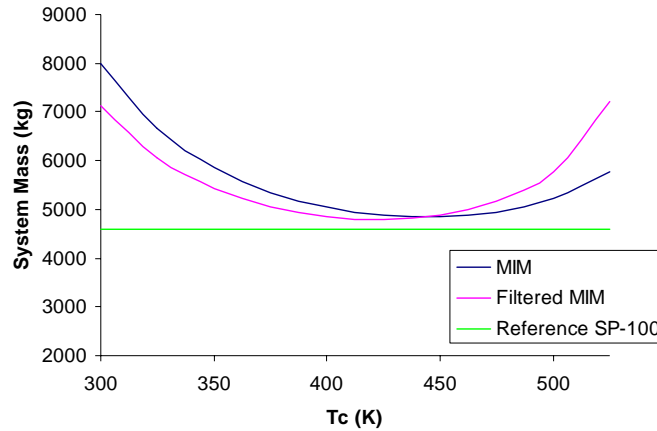
Figure 59. Overall System Mass vs. Heat Rejection Temperature

Note that the reference system mass appears above for the original source data from SP-100. The minimum mass of 4790 kg occurs at a rejection temperature of 425 K for the filtered MIM. The unfiltered device produces a slightly higher mass until the steeper slope on the unfiltered MIM's efficiency curve takes over at 425 K. The TPV

system with single sided radiators masses 4.6% more than the reference SP-100 system. Subsequent sections examine the distribution of the mass difference by subsystem.

1. Reactor and Primary Piping Mass

The dependence of reactor mass on heat rejection temperature appears below in Figure 60.
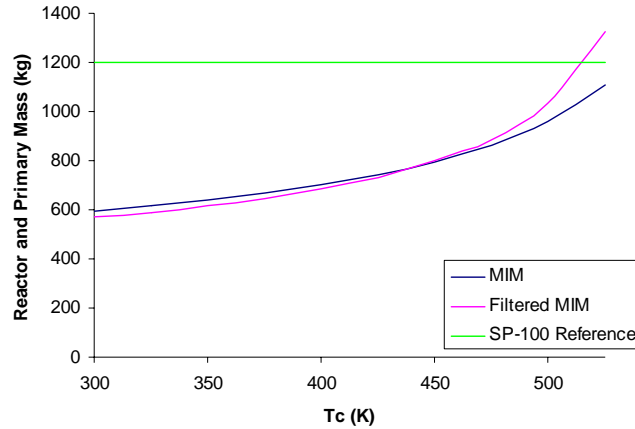
Figure 60.　　　Reactor Mass vs. Heat Rejection Temperature

The figure is monotonically increasing and the smallest reactor mass appears at the lowest rejection temperature. This is to be expected since the TPV efficiency is at a maximum at that temperature. Notice that the filtered MIM produces slightly smaller reactor masses until its efficiency drops below the unfiltered MIM at high temperatures. The minimum overall mass system has a reactor mass of 686 kg. This value is 57% of the SP-100 value and illustrates the utility of recuperation; more recuperation means less power output required from the reactor and a smaller reactor.

2. Effect on Shield Mass

The dependency of shield mass on heat rejection temperature appears below in Figure 61.
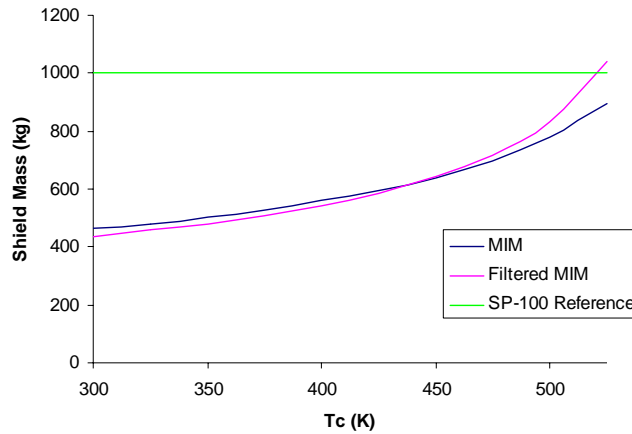
Figure 61.   Shield Mass vs. Heat Rejection Temperature

This graph shows the expected close dependence on reactor thermal power. The higher efficiency of the TPV system again produces lower mass subsystems. The differences that filtered and unfiltered MIMs produce in shield mass are again functions of their efficiencies. The minimum mass (T_c=425 K) system has a shield whose estimated mass is 54% of the reference SP-100 shield.

3.   Effect on Radiator Mass

The temperature dependence of radiator mass on rejection temperature appears below in Figure 62.
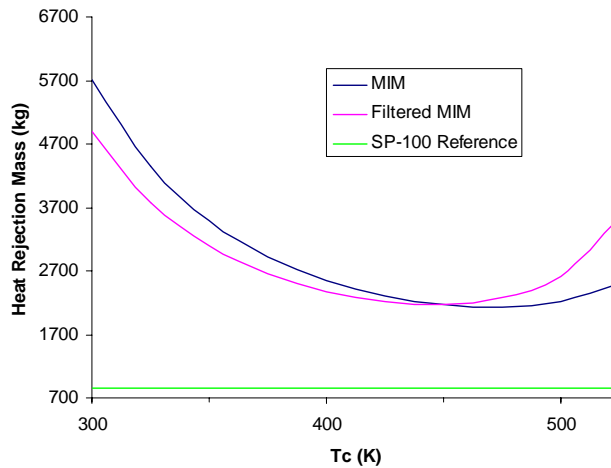
Figure 62.   Radiator Mass vs. Rejection Temperature

It is clear from the figure that an optimum rejection temperature results in a minimum radiator mass. It is also clear that this radiator is more massive than the reference SP-100 radiators. The minimum overall mass system at 425 K has radiators that mass 2218 kg. This is 383% the mass of the reference SP-100 heat rejection system. These are both expected consequences of the lower rejection temperatures. Note that the unfiltered MIM has a slightly lower minimum radiator mass (2130 kg) than the filtered MIM (2179 kg). This is due to the fact that the unfiltered MIM's efficiency drops off more slowly with increasing rejection temperature than the filtered MIM's. They eventually intersect at approximately 450 K, the unfiltered MIM's efficiency is higher and the radiator mass is lower after that point.

C.   THE COOLING PROBLEM

The massive heat rejection radiators completely eliminate any mass advantages gained from increased TPV efficiency. The decreases in reactor and shield mass are insufficient to compensate for the larger radiators required at the lower operating temperature. The sheer area involved presents problems as well. A graph of radiator area vs. heat rejection temperatures appears below in Figure 63.
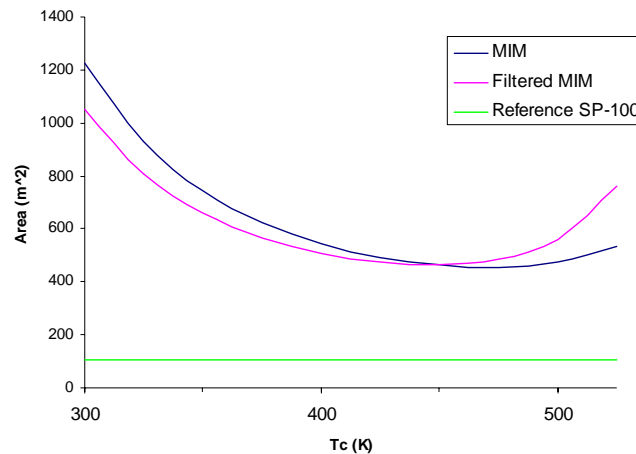
Figure 63.   Heat Rejection Radiator Area vs. Rejection Temperature

475 m^2 are required at 425 K for the filtered MIM. This is a 449% increase over 106 m^2 for the reference SP-100 radiators. The difference is due to the 450 K difference in heat rejection temperatures and appears to present insurmountable practical difficulties. The problem is illustrated below in Figure 64.
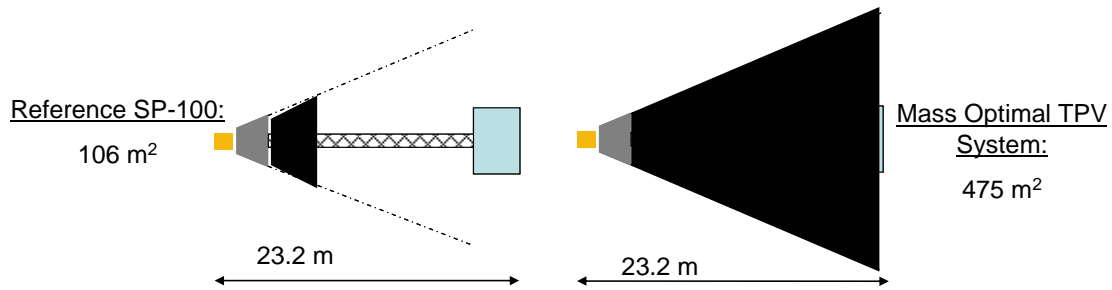
Figure 64.   Reference SP-100 vs. Mass Optimal TPV Radiator Sizes

The larger radiator complicates launch packaging, deployment, and interferes with the operation of the Power Management and Distribution shunt radiator mounted on the User Interface Module (blue box to the right of the reference figure). It is also difficult to conceive of a heat rejection radiator design that could service the relatively small TPV array (17.54 m^2) while being restricted to the approximately 5m heat pipe element lengths expected with low temperature heat pipes using a water working fluid[Ref. 54].

This chapter has described the assumptions, methodology, and results of an assessment of current developmental TPV technology applied to a SNRPS. The current developmental TPV MIMs appear to offer no benefit for this application. Advances in device efficiency and space radiators may change this situation and are the subject of the next chapter.

THIS PAGE INTENTIONALLY LEFT BLANK

VI. FUTURE DEVELOPMENTS

The analysis of test data from present developmental MIMs indicates that lower mass reliable space power systems are possible at the price of unwieldy low temperature space radiators. Smaller and or lighter radiators are clearly desirable. Two approaches suggest themselves; raise system efficiency or increase the amount of radiator area that can be packed into a given mass or volume. Radiator technology is not the central concern of the present work and will not be considered further in this section. The interested reader will find useful information on an advanced heat pipe radiator materials and other concepts for reducing radiator specific mass in <u>Appendix B</u> and [Ref. 9].

Carnot showed us that the efficiency of a heat engine may be increased by increasing its input heat temperature. This means higher reactor temperatures, more development risk, and more costly nuclear system testing. The approach in this chapter is to suggest the potential of TPV by making assumptions about future technology developments and using the system model to assess the impact on overall system mass and radiator area. This involves a certain amount of speculation and a skeptical treatment is warranted. The assumptions made are backed up by laboratory data whenever they could be obtained from the published literature.

A. TEMPERATURE MATCHED FRONT SURFACE FILTER

One way to improve efficiency has already been discussed; create a filter that is temperature-matched to the bandgap of the filtered Bettis MIM. Recall that the filtered MIM's performance suffered more than its unfiltered counterpart at high temperatures because the front surface filter had been designed for the device bandgap at 300 K. The device bandgap changes as it gets hotter but the filter's cutoff stays constant. This section assumes that a filter can be designed for each device operating temperature between 300K and 525K at which a filtered MIM might be expected to operate. This assumption is also made by the MIM's designers [Ref. 30, p. 514]. Mathematically, this means that the filtered and unfiltered MIM's efficiency and output power lines have the same slope when plotted vs. device operating temperature as shown below in Figure 65.
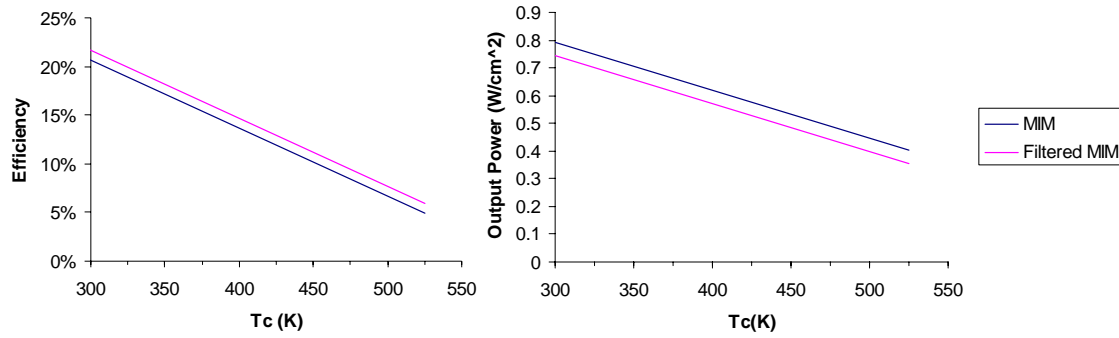
Figure 65.   Temperature Corrected Filtered MIM Performance vs. T_C

This allows the filtered MIM to retain its efficiency advantage over the unfiltered MIM over the entire T_C range. The system efficiency at the new minimum mass point is approximately 1% higher than the un-corrected filter discussed in the last chapter. The amount of radiator area required by the minimum mass system is reduced by 57 m^2 (12%) to 418 m^2 and the operating point shifts up to 450 K. The effect on radiator area and overall system mass is shown below in Figure 66.
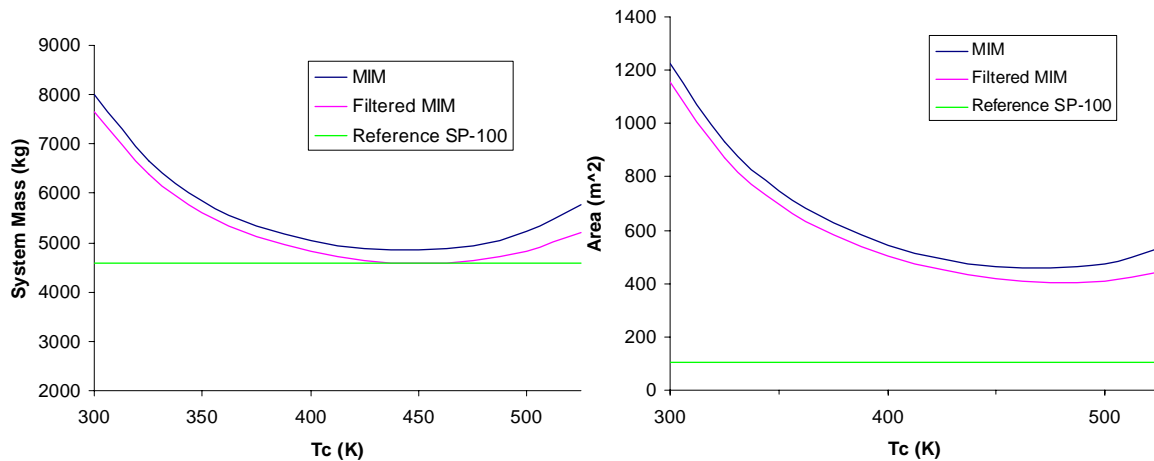
Figure 66.   System Effect of Temperature Corrected Filtered MIM

The temperature corrected filter makes the filtered MIM slightly more competitive with the reference SP-100 case. The minimum overall system mass is 4592 kg, 0.3% heavier than the reference case. The radiators are 394% the size of SP-100's however and further improvements in efficiency appear desirable.

B. **IMPROVED SPECTRAL CONTROL EFFICIENCY**

Recall from Chapter IV the profound effect which spectral control efficiency had on overall system efficiency. It is reasonable to use the radiative model developed previously to estimate the possible effects of increased spectral control efficiency on system parameters. The radiative model merely provides a means of prediction. Its use requires the assumption that the correlation between the radiative model and actual MIM behavior will hold for higher spectral control efficiencies. This assumption makes the following analysis speculative until such time as more advanced devices are fabricated. The importance of spectral control efficiency was highlighted in Figure 46. but a simpler presentation should make the benefits even more apparent. The filtered Bettis MIM previously described had a spectral control efficiency of 70% and a bandgap of 0.6eV. The figure below contains a plot of device efficiency for a 1300 K heat source, a 300 K cell, and two values of spectral control efficiency.
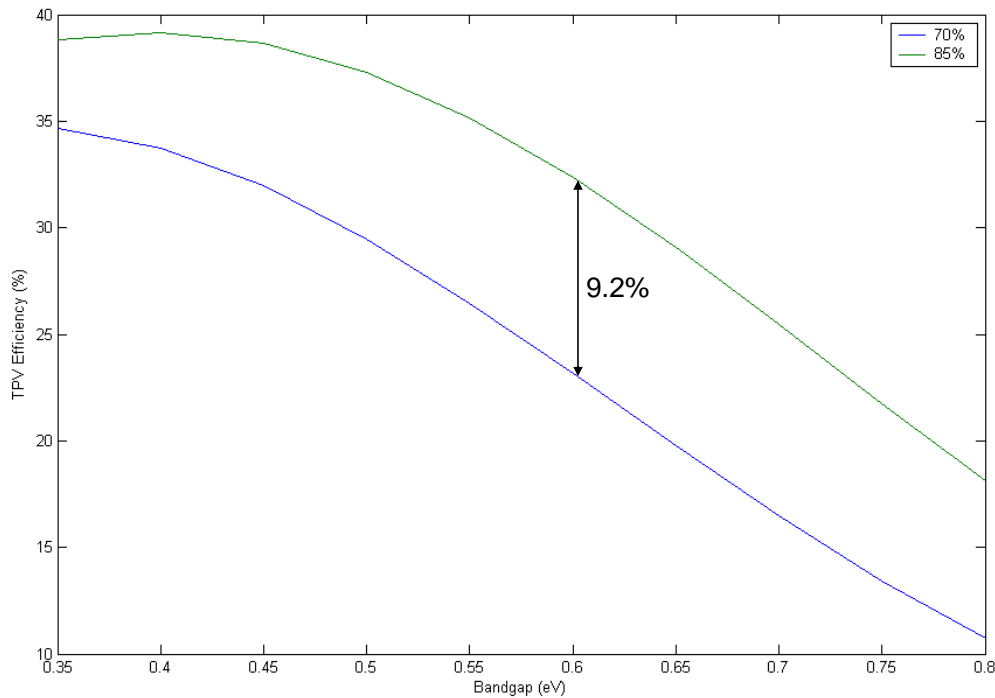
Figure 67.   Benefit of Improved Spectral Control for 0.6eV Cell

The benefit is an increase of 9.2%. This section assumes that 85% efficient spectral control is achievable. The Bettis team has recently reported 83% efficient spectral control for a 0.52 eV tandem filter at 325 K with an in-band reflectivity of 10% making the achievement of their near term 85% spectral control efficiency goal plausible. [Ref. 46, p. 172]

Figure 46. also demonstrated that further efficiency increases can be obtained with lower bandgap cells. A plot of predicted TPV efficiency versus cell bandgap for 85% efficient spectral control at various device operating temperatures from 300 to 525 K appears below in Figure 68.
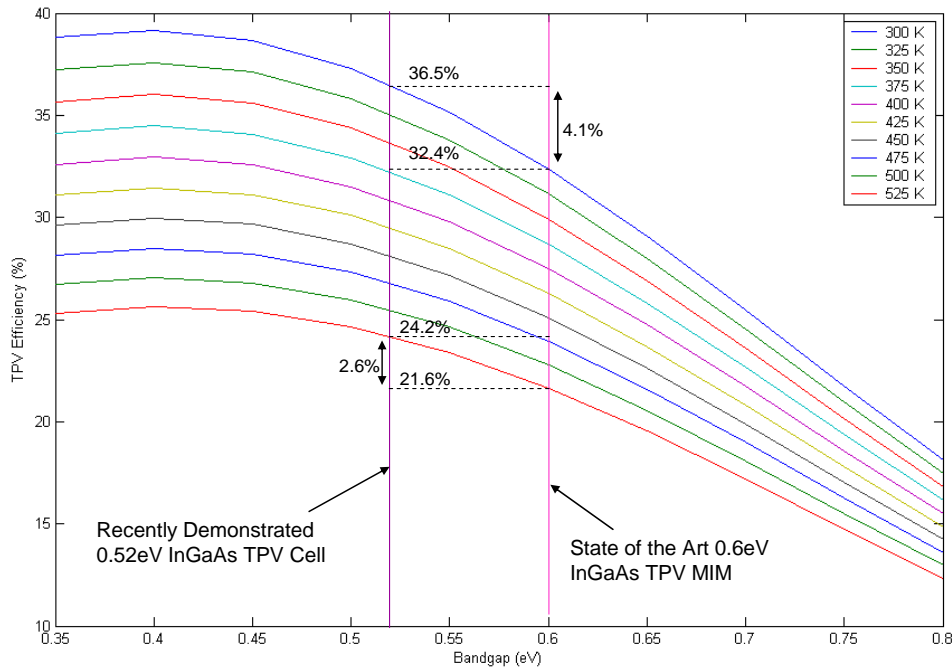
Figure 68.   Theoretical Device Efficiency Difference Between 0.6 eV and 0.52 eV for T_H=1300K, β=85% and Various T_C

It is clear that even higher efficiencies can be found at lower bandgaps. Lower bandgaps mean more available photocurrent and increased efficiency. The shift from 0.6eV to 0.52 eV provides a theoretical increase of 4.1% in efficiency at 300 K and 2.6% at 525 K. The MIM described and analyzed previously was fabricated with a 0.6 eV InGaAs active layer. Bettis has also recently reported development of a 0.52eV InGaAs single cell device. The device layer design is almost identical to the single cells in the

MIM described previously but the relative concentrations of indium, gallium, and arsenide are different. Initial testing of the device indicates that it would produce a short circuit current density of 3.65A/cm^2, open circuit voltage of 0.307 V, and a fill factor of 62.5% under ~1273 K illumination. The device cross section and the single cell layout appear below in Figure 69.
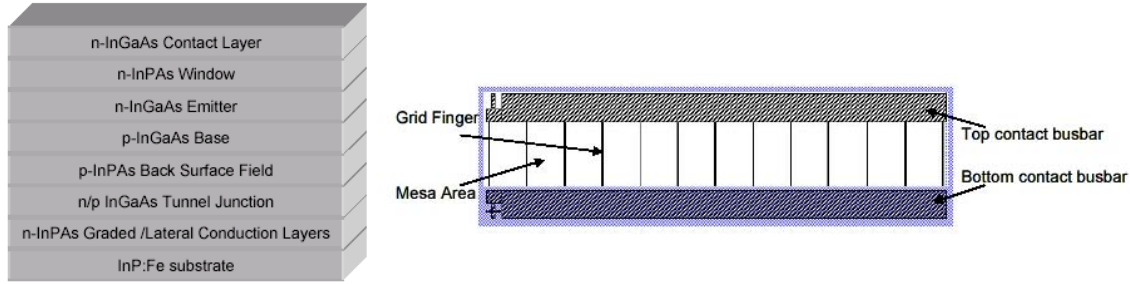
Figure 69.   Schematic Cross Section and Top View of Single Cell 0.52eV InGaAs TPV Device [from Ref. 47, p. 447]

Progress with this device encourages consideration of the benefits of a 0.52eV MIM combined with an 85% efficient spectral control system. The method here assumes that the resultant device's efficiency at 300 K is predicted from the radiative model. The following analysis assumes that the model over predicts the device efficiency at 300K by 5% (relative). The result is the assumption that a 0.52 eV InGaAs MIM with 85% efficient spectral control will have an efficiency of 34.7% at 300 K. This prediction is taken as a starting point to extrapolate an $\eta_{TPV}(T_C)$ relationship by assuming that a TPV MIM can be designed at 0.52 eV with a temperature matched filter over the whole device operating temperature range of interest. Mathematically, this means assuming a 0.52 eV MIM will have the same slope $\eta_{TPV}(T_C)$ as the unfiltered MIM. The result of these assumptions if the following conjectural equation for $\eta_{TPV}(T_C)$.

$$\eta_{TPV}(T_C) = \frac{-0.0699\%}{°K} T_C + 34.7\% \tag{31}$$

The calculations here assumes that the output power density performance of the device is identical to the temperature matched filtered MIM described in the previous section. This assumption is probably conservative because the increase in available photocurrent should increase the output power density of the device. There is little other

choice for comparison because the radiative TPV model predicts output power within 20% at best. The output power relationship used for heat source radiator sizing is given below.

$$P_{elec}(T_C) = -\frac{0.0017W}{cm^2 K}T_C + 1.265\frac{W}{cm^2} \tag{32}$$

The remarkable result of this admittedly uncertain chain of assumptions is shown below in Figure 70.
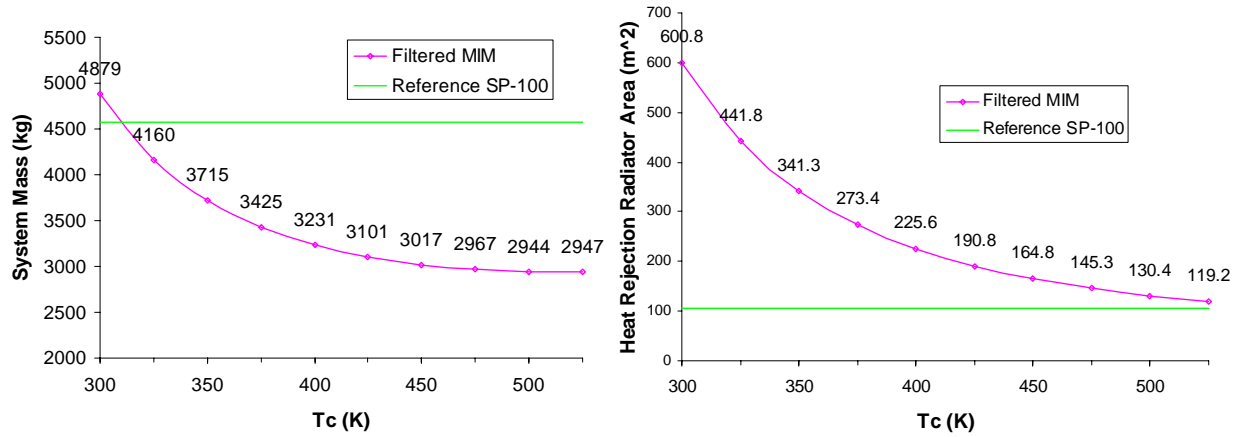
Figure 70.   Overall System Mass and Radiator Area for Conjectural 0.52eV MIM Assuming 95% Predicted Efficiency

Things are now becoming interesting. The absolute minimum overall system mass case above masses 2944 kg which is a 36% reduction over SP-100. The cost is a heat rejection radiator area of 130 m^2 (only 123% the reference SP-100 radiator area). The devices in this case are projected to operate at 20.7% efficiency at 500 K.

This curve by necessity contains many assumptions. Two deserve special mention. The first is that it is assumed without evidence that a TPV device will operate 160 K beyond the highest temperature for which experimental data has been collected. The uncomfortable reader will note that a 400 K TPV operating temperature produces a system mass of 3231 kg and radiator area of 225.8 m^2. This system mass is 71% that of SP-100 and the radiators are 213% larger. Radiators this size would extend 15 m down the SP-100 boom and would have much less chance of interfering with the radiators on the User Interface Module.

100

The other critical assumption is that a 0.52 eV InGaAs MIM can be built to operate with 95% of the efficiency predicted by the radiative thermo-chemical TPV model. This assumption is conservative for the one existing data point (i.e., the Bettis MIMs) but it is important to assess what happens if the difference is larger. The effect on system mass and radiator area for a 0.52eV device with 75% of the predicted performance at 300 K is shown below in Figure 71.
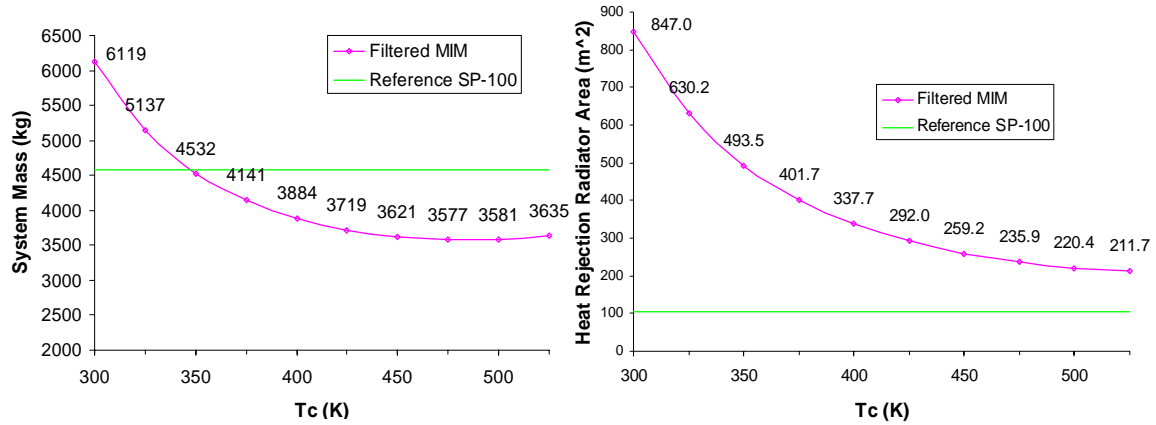
Figure 71.   Overall System Mass and Radiator Area for Conjectural 0.52eV MIM Assuming 75% Predicted Efficiency

The minimum mass system still shows masses less than SP-100 at 3577 kg with a radiator area 220 m^2. This is a 22% reduction from SP-100 mass with approximately twice the radiator area. This represents a substantial mass improvement with realizable radiator area.

C.   MULTI-JUNCTION CELLS

Another reason to expect that large fractions of the theoretical efficiency can be achieved is the multi-junction or tandem TPV cell. Recall from Chapter III that above band gap photons that enter a cell will cause over-excitation losses as generated electrons lose energy to the semiconductor lattice. This causes cell heating and reduces the overall device efficiency. An ideal photovoltaic converter consists of an infinite number of finely graded bandgaps. Each one absorbs a small fraction of the incident light just above it own bandgap and leaves the rest to the other junctions. All of the heat transfer in this idealized device takes place completely reversibly through photon emission and absorption between the heat source radiator and the cell. The radiative thermo-chemical model of

101

TPV power conversion used previously does not take these losses into account. Their reduction represents a major step toward realizing the efficiency goals of the previous section. [Ref. 48, p. 17]

Real multi-junction devices approximate this ideal by layering a finite number of p-n junctions in an attempt to reduce such losses. Each junction has a different bandgap. The junctions are stacked atop each other such that the incoming photons enter the highest bandgap junction first. The lower energy (longer wavelength) photons penetrate deeper into the device to interact with the lower bandgap junction. The two junctions must be interconnected with low series resistance and maximum optical transparency to most efficiently sum their voltages and drive current through an external load as illustrated below in Figure 72.
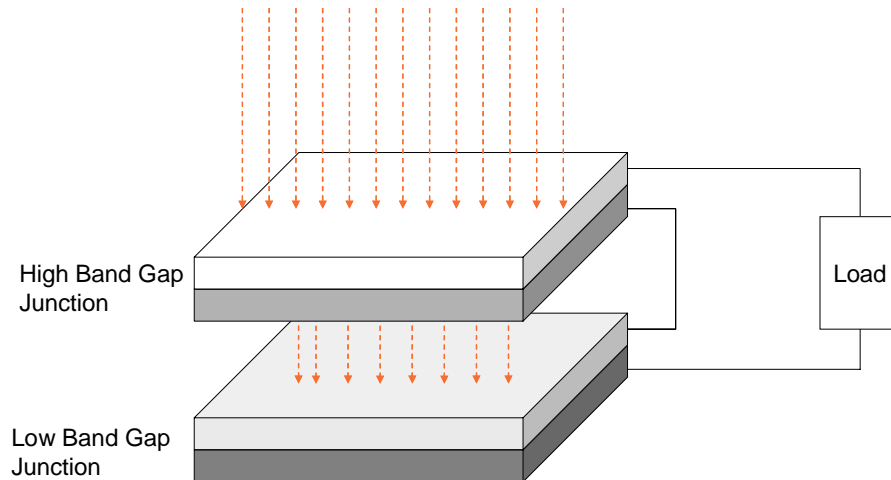
Figure 72.   Multi-Junction Photovoltaic Cell Schematic

Multi-junction cells are thus expected to approach ideal radiative diode performance more closely with an increasing number of junctions. This approach is not without problems. Additional features in a device increases series resistance and losses. Nonetheless, the multi-junction approach has been used to great effect in solar cells. The configuration shown above is known as a two junction cell for obvious reasons. Triple junction InGaP/GaAs/Ge solar photovoltaic cells are presently in service on board Earth orbiting spacecraft. They routinely operate with 28.3% efficiency at the beginning of life before exposure to the near-Earth radiation environment [Ref. 4]. A five junction

AlGaInP/GaInP/AlGaInAs/GaInAs/Ge cell with approximately 19% efficiency under standard vacuum solar illumination (AM0) and an open circuit voltage of 4.744V has also recently been fabricated[Ref. 52, p.617].

These devices make it likely that multi-junction TPV systems can be fabricated. Indeed, tandem TPV converter diodes have recently begun appearing in the literature. One device developed at Bettis uses an InGaAsP top layer with a 0.72eV bandgap and an InPAs bottom layer with a 0.6eV bandgap. The structure of a single device appears below in Figure 73.

Epitaxial-side Illumination

Grid Metal Contact

Contact Layer

High-Eg $In_{0.82}Ga_{0.18}As_{0.71}P_{0.29}$/ $InP_{0.64}As_{0.34}$ DH LMM Diode

Tunnel Junction

Low-Eg $In_{0.69}Ga_{0.31}As$/ $InP_{0.64}As_{0.34}$ DH LMM Diode

Tunnel Junction

Compositionally Graded $InP_{1-Y}As_Y$ n-type Buffer Layers/LCL

InP Semi-insulating Substrate
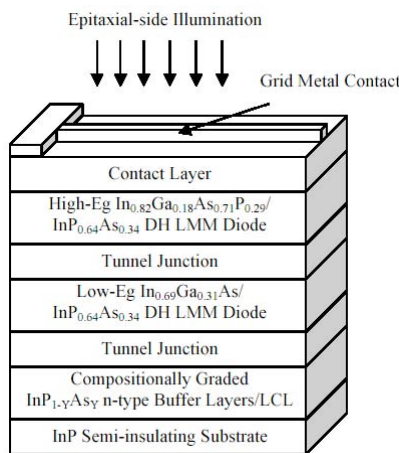
Figure 73.   InGaAsP/InGaAs Tandem TPV Device [from Ref. 49, p. 483]

The tunnel junction is recalled from the MIM architecture described in Chapter IV as a thin highly doped layer which minimizes the voltage lost between two semiconductor layers. Other features serve similar functions to those previously described. Illumination of a single diode under ~1273K gray body source provided an open circuit voltage of 0.504 V, a short circuit current density of 0.069 A/cm^2, and a fill factor of 72.3% with the device at 298 K [Ref. 49, p. 486]. This implies a power density of 0.025 W/cm^2 under these conditions. The device efficiency cannot, unfortunately, be calculated because the available literature does not specify the emissivity and spectral control efficiency of the radiator used for the tests. This example does serve to illustrate that multi-junction cells are viable for TPV application, however.

Tandem devices have also been interconnected in both series and parallel to produce different classes of MIM. The organization that appears to have done the most work for this application is, predictably enough, Bechtel Bettis. They have reported on the fabrication of at least two tandem MIM designs in the literature [see Refs. 41 and 50]. At least one MIM has been tested under ~1273 gray body illumination (emissivity ~0.3) and produced 6.14 volts open circuit, 0.292 A/cm^2 short circuit current, and a fill factor of 67.6% at a device temperature of 325 K. [Ref. 50, p. 894-895]. This is roughly 1.2 W/cm^2. The efficiency of the device was not reported in the literature and is not computable with the information reported.

These devices are just beginning to see production for TPV applications and much of the available literature is concerned with fabrication rather than performance. Limited available time has prohibited the development of multi-junction model for this thesis. Wanlass and Albin have produced an extensive model for a tandem cell which should be published early next year (2005) [Ref. 51].

An early estimate of multi-junction TPV performance may be found by analogy to another photovoltaic device application. The sun provides much less intensity for solar cells to work with than the nearby heat source radiators discussed in this thesis. The 1300 K blackbody considered previously generates an incident power density on a nearby TPV cell of ~160,000 W/cm^2. Recall from Chapter 2 that solar cells in Earth orbit work on 1,373 W/cm^2. This is 117 times less energy. Since higher incident light concentrations are known to improve the device efficiency, solar cell designers have built cells and placed them under optical concentrators or non-imaging magnifiers to increase the efficiency of solar power systems. They have also built tandem cells for use in these systems. Recent literature reports solar concentrator arrays using triple junction InGaP/InGaAs/Ge cells have achieved greater than 36% device efficiency under 100-500X concentration conditions analogous in power density to those in a TPV system without the beneficial ability to send unused light back to the radiator [Ref. 53, p. 585].

This section suggests that thermophotovoltaic power conversion may have substantial benefit for space nuclear reactor power systems. Improved spectral control techniques such as filter-device temperature matching, and increased spectral control efficiency have the potential to dramatically reduce overall system masses while maintaining reasonable radiator sizes. Preliminary results for multi-junction devices give hope that the substantial fractions of theoretical device efficiency required will soon be achieved. Results from solar concentrator multi-junction cell tests show that photovoltaic devices can operate at high efficiencies under illumination conditions analogous to those found in the SNRPS TPV system considered here.

THIS PAGE INTENTIONALLY LEFT BLANK

VII. CONCLUSIONS

Theory suggests that multi-junction thermophotovoltaic power conversion devices operating at feasible efficiencies in concert with a realistic near-term space nuclear reactor heat source will reduce overall power system mass without requiring increases in nuclear fuel temperature. Such systems utilize energy more efficiently that other direct electric conversion systems resulting in tolerably sized low temperature heat pipe radiators. This finding is primarily due to TPV's recuperation of unused energy thus sparing the reactor mass necessary to replace aforesaid energy and the radiator mass necessary to reject it to space. TPV also avoids design issues associated with moving parts in dynamic power conversion systems. In short, TPV may offer dynamic power conversion efficiency with static power conversion reliability. It has also been shown that high system efficiencies are within the bandgap capability of available semiconductor materials and that efficiencies similar to those predicted hear have been achieved in photovoltaic cells for solar concentrator application, thus further indicating that such systems may be practical for space reactors in the future.

The present work can do no more than tantalize the prospective space power system designer, however. The development of TPV is still in its early stages and there are many open questions that must be answered before a definitive evaluation can be made. Perhaps the most serious issue is the performance and lifetime of high efficiency TPV MIM devices at elevated temperatures. The trade studies in this thesis show that it may be desirable to operate TPV up to 500 K and their lifetime under these conditions appears completely unknown at the time of this writing. The simple model presented here only suggests the efficiencies that might be expected and depends on the assumption that future multi-junction devices will have the same efficiency degradation with temperature as their single junction predecessors. This is another area where little work appears to have been done. More detailed modeling and experimentation must determine the actual performance at elevated temperatures. TPV cell radiation hardness is also in question. Shielding will almost certainly be necessary but the question of how much rests upon irradiation tests. Extensive experience in the solar power community suggests that cells

can be hardened against high energy proton bombardment but further modeling and laboratory work must be done to determine performance and lifetime limits.

Future work in this area should concentrate on the aforementioned cell modeling, to include multi-junction MIM modeling. The impact of TPV array design on spacecraft power control was beyond the scope of the present study but is an area ripe for exploration. Estimation of the maximum achievable output voltage and quantification of system mass impacts accruing from the availability of high voltage DC power at the output terminals of the power conversion system should be high priorities of any future work in this area. Finally, there are open questions surrounding the optimal nuclear control scheme for a reactor which is coupled to a TPV power conversion system. Most modern reactors have load following characteristics which reduce reactor output power automatically when the power conversion system load decreases. It is unclear how best to accomplish this in a TPV system.

APPENDIX A. ENDOREVERSIBLE RADIATIVE THERMO-CHEMICAL ENGINE MODEL OF A TPV SYSTEM

Rubin introduced the theory of endoreversible thermodynamics in 1979. It is a subset of irreversible thermodynamics in which all of the losses in a system occur in the heat transport processes. Thermophotovoltaic output power may be approximated by considering the device a radiative thermo-chemical engine operating between the heat source radiator and the cold sink. This Appendix contains the derivation of the output power equation (23) used in Chapter IV Section B. The derivation that follows is due primarily to De Vos' tutorial on the application of endoreversible thermodynamics to solar energy conversion [Ref. 36] with a few modifications to model a thermophotovoltaic system introduced by Gray and Al-Husseini [Ref. 34]. This thesis deviates from [Ref. 34] by only considering flat plate TPV systems with unity view factor between the heat source radiator and cell.

An endoreversible thermodynamic engine consists of a source, a sink, a converter, and the flows of matter and energy between them. The general case appears on the left below in Figure 74.
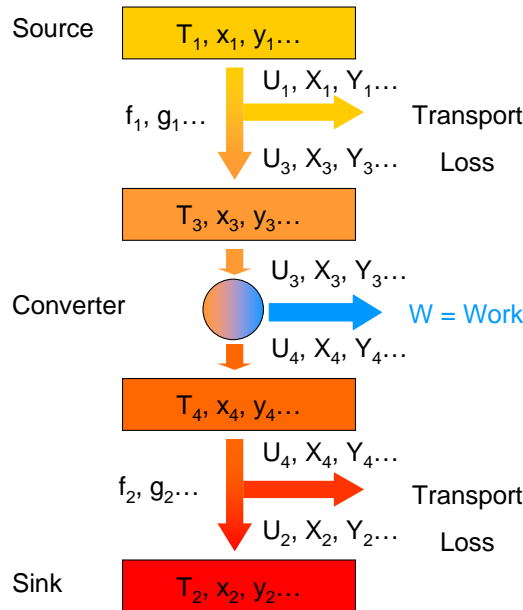

Figure 74.   General Endoreversible Thermodynamic Engine (left) and Endoreversible Engine with Losses Only at Source [After Ref. 36, p. 76]

The four reservoirs each with a temperature property (T_i) and a set of constant internal properties (x_i, y_i, ...) that might represent reservoir chemical potential, voltage or pressure. Transport between reservoirs consists of the energy current (U_i), a set of parameter currents (X_i, Y_i, ...). The parameter currents are defined such that $x_i X_i$ has units of work. Work, W, is performed reversibly in the converter. The rate at which these currents flow is governed by transport equations (f_i, $g_{i,...}$) of the form below.

$$
\begin{aligned}
U_1 &= f_1\left(T_1, x_1, y_1, ...\right) - f_1\left(T_3, x_3, y_3, ...\right) \\
X_1 &= g_1\left(T_1, x_1, y_1, ...\right) - g_1\left(T_3, x_3, y_3, ...\right) \\
Y_1 &= h_1\left(T_1, x_1, y_1, ...\right) - h_1\left(T_3, x_3, y_3, ...\right) \\
U_2 &= f_2\left(T_4, x_4, y_4, ...\right) - f_2\left(T_2, x_2, y_2, ...\right) \\
X_2 &= g_2\left(T_4, x_4, y_4, ...\right) - g_2\left(T_2, x_2, y_2, ...\right) \\
Y_2 &= h_2\left(T_4, x_4, y_4, ...\right) - h_2\left(T_2, x_2, y_2, ...\right)
\end{aligned}
\tag{33}
$$

Conservation of energy implies

$$
\begin{aligned}
U_1 &= U_3 \\
U_4 &= U_3 + W \\
U_2 &= U_4
\end{aligned}
\tag{34}
$$

Since no entropy is assumed to be generated in the converter, conservation of entropy implies that the entropy currents (S) flowing into and out of the converter are the same.

$$
S_4 = S_3 \tag{35}
$$

By definition and the laws of thermodynamics

$$
S = \frac{Q}{T} = \frac{U - (xX + yY + ...)}{T} \tag{36}
$$

where Q is the heat transfer associated with a given energy rate, U.

Thermo-chemical engines are a further subset of endoreversible thermodynamic engines. Thermo-chemical engines are so-called because their reservoirs are characterized only by the chemical potential, μ, and the reservoir temperature. The generic current, X, becomes the particle current, N. We will introduce the simplifying

110

assumption that the transport rate between reservoirs four and two is essentially unlimited. This simulates a cell in thermal contact with a cold sink. This allows us to combine reservoirs two and four into a single logical unit. These assumptions reduce to the system shown below in Figure 75.
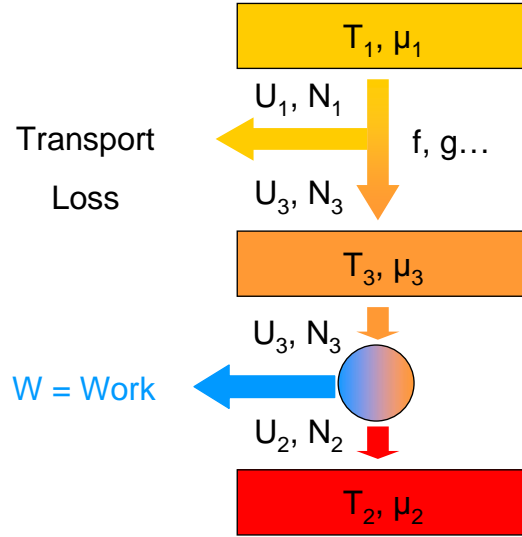
Figure 75.   Thermo-Chemical Engine

Note that there is only one transport process to consider and the transport equations reduce to

$$U_1 = f\left(T_1, \mu_1\right) - f\left(T_3, \mu_3\right)$$
$$N_1 = g\left(T_1, \mu_1\right) - g\left(T_3, \mu_3\right)$$

(37)

The general axioms mentioned previously lead us to conclude that

$$U_1 = U_3 \quad \text{(Conservation of Energy)}$$
$$U_3 = W + U_2 \quad \text{(Conservation of Energy)}$$
$$\frac{U_2 - \mu_2 N_2}{T_2} = \frac{U_3 - \mu_3 N_3}{T_3} \quad \text{(Conservation of Entropy)}$$

(38)

The conservation of particles adds

$$N_1 = N_3$$
$$N_3 = N_2$$

(39)

111

(38) and (39) combine to form an equation for the output work in the system whose first term is identical to the Carnot equation (5).

$$W = \left(1 - \frac{T_2}{T_3}\right)U_1 + \left(\frac{T_2}{T_3}\mu_3 - \mu_2\right)N_1 \tag{40}$$

Equations (37) and (40) combine to form an equation for the output work in a general thermo-chemical engine.

$$W = \left(1 - \frac{T_2}{T_3}\right)\left[f(T_1,\mu_1) - f(T_3,\mu_3)\right] + \left(\frac{T_2}{T_3}\mu_3 - \mu_2\right)\left[g(T_1,\mu_1) - g(T_3,\mu_3)\right] \tag{41}$$

Radiative engines are engines in which the particles exchanging the energy between reservoirs are photons. The transport process is thus modeled by blackbody equations. The energy transport equation is given by

$$f(T,\mu) = \frac{2\pi}{c^2 h^3}\int_{E_G}^{\infty}\frac{E^3 dE}{e^{\left(\frac{E-\mu}{kT}\right)} - 1} \tag{42}$$

The photon transport equation is given by

$$g(T,\mu) = \frac{2\pi}{c^2 h^3}\int_{E_G}^{\infty}\frac{E^2 dE}{e^{\left(\frac{E-\mu}{kT}\right)} - 1} \tag{43}$$

E is the photon energy. E_G is the band gap energy which limits radiative transport, i.e. the larger of the bandgaps of the two materials involved in the energy/particle exchange. Note that these equations assume flat-plate geometry with unity view factor. This is a common geometry in TPV systems. The constants have been chosen to give energy and photon fluxes.

Two further sets of simplifying assumptions apply to a TPV system. First, the chemical potentials of the heat source radiator and cold sink are zero. This is because the radiator and converter are separated by a vacuum and no particles (with the exception of photons) flow between them. The converter is also assumed to be thermally connected to an insulating cold sink and there is no particle exchange between the two. This leaves

112

only one parameter, the chemical potential of the converter itself. This chemical potential is equal to the carrier charge (electron charge) times the bias voltage across the device.

$$\mu_1 = \mu_2 = 0$$
$$\mu_3 = \mu = q_e V$$

(44)

Finally, the temperature of the converter is assumed identical to the temperature of the cold sink. This is reasonable given that they are in direct thermal contact. The final system diagram appears below in Figure 76.
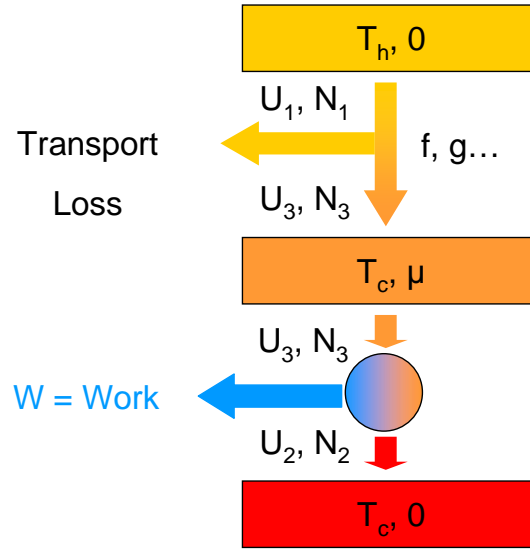
Figure 76.   TPV as Radiative Thermo-Chemical Heat Engine

Setting $T_2=T_3$ and $\mu_2=0$ in the work equation (41) yields

$$W = \mu N_1$$

(45)

It may be surprising that the work output of the cell is independent of the total energy transported into the device. This apparent conundrum can be explained by realizing that N_1 is the net rate of above bandgap photon transport into the cell and μ is the energy per charge carrier. Recall, that this model assumes that all irreversibility occurs outside the device. It therefore assumes that any photon which makes it into the cell generates a carrier and that the carrier leaves the cell to do work, μ, in an external circuit. The transport equations (42) and (43) substituted into the photon particle current equation (37) and work equation (45) yield the output power per unit area.

$$W = \frac{2\pi q_e V}{c^2 h^3} \left[\int_{E_G}^{\infty} \frac{E^2 dE}{e^{\left(\frac{E}{kT_h}\right)} - 1} - \int_{E_G}^{\infty} \frac{E^2 dE}{e^{\left(\frac{E - q_e V}{kT_c}\right)} - 1} \right]$$

$$W = \frac{2\pi q_e V}{c^2 h^3} \left[\int_{E_G}^{\infty} \frac{E^2 dE}{e^{\left(\frac{E}{kT_h}\right)} - 1} - \int_{E_G}^{\infty} \frac{E^2 dE}{e^{\left(\frac{E - V}{kT_c}\right)} - 1} \right] \text{ (for E in eV)}$$

(46)

This derivation only awaits the addition of reflection and spectral control to make it complete. These affect only the first integral in the transport equations. The effect of the spectral control is to reduce the number of photons getting into the cell. This introduces asymmetry into the transport equations in the form of restricted limits of integration on the first integral. Reflection allows only a fraction, (1-R), of the in-band photons make it into the cell to generate charge carriers. Multiplying the first integral by that factor completes this derivation.

$$W = \frac{2\pi q_e V}{c^2 h^3} \left[(1 - R) \int_{E_L}^{E_H} \frac{E^2 dE}{e^{\left(\frac{E}{kT_h}\right)} - 1} - \int_{E_G}^{\infty} \frac{E^2 dE}{e^{\left(\frac{E - q_e V}{kT_c}\right)} - 1} \right]$$

(47)

A MATLAB™ code was produced to solve this equation, find its maximum with respect to voltage (the max power point) and plot it for various bandgaps. These results were compared with those from [Ref. 34] to verify the code prior to using it for the lower range of temperatures considered here. A sample comparison between this code and the results from Gray and Al-Husseini appear below in Figure 77. Good agreement is demonstrated and further results derived from this code are thus justified.
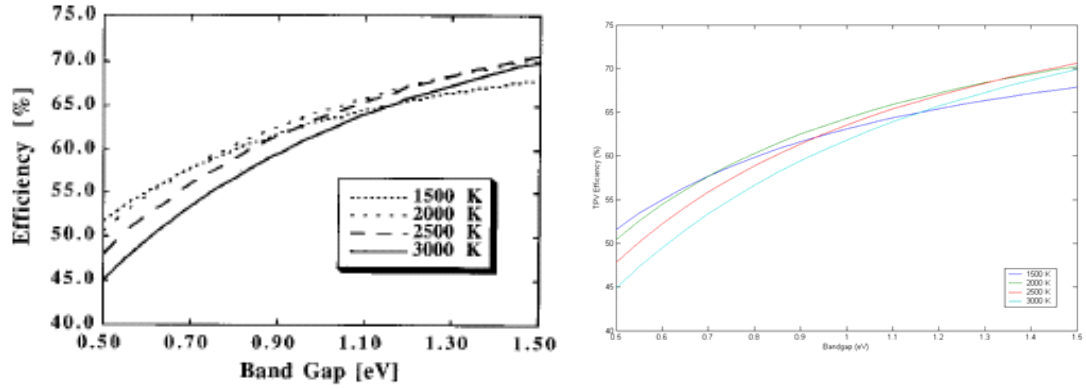
Figure 5. Predicted maximum TPV system efficiency with high pass ($E>E_g$) spectral selection for various temperatures of the black-body emitter. The TPV cell is at 300 K.

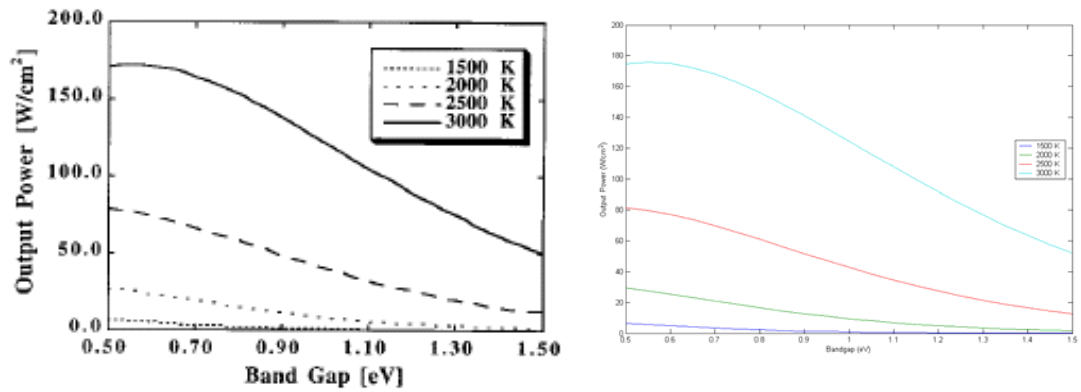**Figure 6.** TPV system output power with high pass ($E>E_g$) spectral selection for various temperatures of the black-body emitter. The TPV cell is at 300 K.

Figure 77.   Comparison of Model Results with Gray and Al-Husseini [from Ref. 34, p. 10]

THIS PAGE INTENTIONALLY LEFT BLANK

# APPENDIX B.   CARBON COMPOSITE HEAT PIPE RADIATORS

That there is a synergistic relationship between power conversion and radiator technologies should be readily apparent. Advances in radiator technology confer benefits on all SNRPS but they particularly favor those with large radiator areas. TPV can thus benefit greatly from methods to reduce radiator specific mass. Picking the right material and working fluid is crucial to the heat pipe radiator design process. Carbon-carbon (C-C) composite heat pipes with various working fluids offer an attractive set of material properties that lead to lower radiator specific mass. Much of the work in this field is due to Dr. Albert Juhasz at NASA's Glenn Research Center in Cleveland, OH. C-C heat pipe radiators appear capable of lowering radiator specific mass to ~1.00 kg/m^2, less than half of the current state of the art pumped loop radiators mentioned previously. This is largely due to the rapid pace of carbon composite technology development [Ref. 24, p. 1].

The key material properties which make carbon composites useful for space radiators are a combination of high thermal conductivity with a high stiffness to mass ratio. These combine to create a radiator which both spreads heat more isothermally than a traditional aluminum panel and weighs less. Carbon composites are increasingly common spacecraft materials and they have been incorporated into more traditional spacecraft radiators that do not use heat pipes. A radiator panel made of carbon composite facesheets with aluminum honeycomb filler has already been flown in space onboard NASA's EO-1 spacecraft [Ref. 55, p. 1]. This panel has successfully been operating on orbit since November 2000 and represents the first use of a carbon composite panel as both a radiator and load bearing structure in a spacecraft [Ref. 56].

A NASA-industry consortium constructed carbon composite heat pipes in conjunction with the NASA Civil Space Technology Initiative (CSTI) High Capacity Power Program. This program was a major NASA effort to develop the technologies required for President George H. Bush's Space Exploration Initiative in the early 1990s. NASA identified spacecraft radiators as a major mass driver in higher capacity space power systems and initiated an effort to develop lower specific mass technology which could be used over a wide variety of operating temperatures. Fabrication and ground

based proof of concept tests were completed on at least two heat pipe units in 1995. [Ref. 57, pp 1-2].

The program produced carbon composite heat pipes lined with various metal foils and using potassium or water working fluid for use as prototype space radiator elements. The prototype unit had a 7.6 cm evaporator section and a 30 cm condenser section with integral fins to increase the radiating surface area. A diagram of the assembled heat pipe appears below in Figure 78.

Figure 78.   Diagram of Carbon Composite Heat Pipe [from Ref. 24, p. 3]
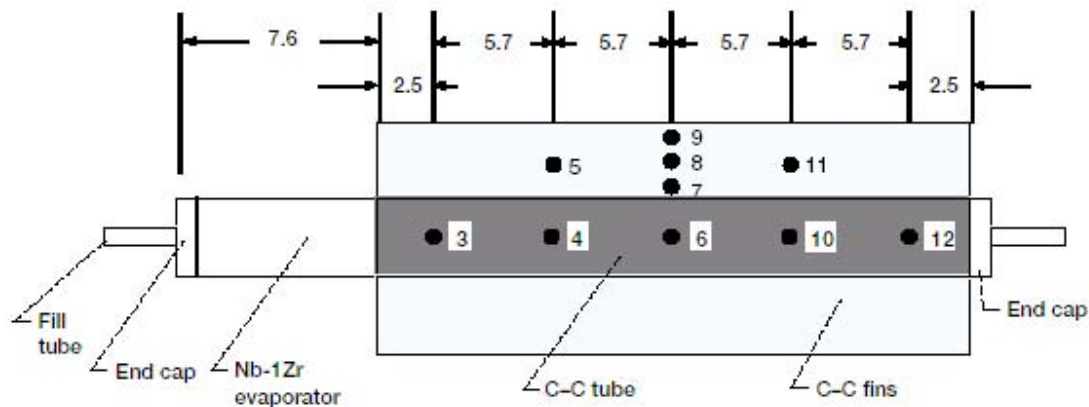
Dimensions on this figure are in centimeters. The end caps and fill tubes have not been mentioned previously but are required to enclose the working fluid and charge the heat pipe. The evaporator is on the left side of the diagram and the numbers on the heat pipe body are the locations of thermocouples used for testing. It is made of niobium with 1% zirconium alloy (Nb-1Zr) and is an extension of the liner material that is used to protect the C-C tube from chemical interaction with the potassium working fluid used in this particular heat pipe. The Nb-1Zr liner is 0.76mm thick where it forms the evaporator and is only one tenth this where it fits into the 1 mm thick C-C outer shell in the condenser [Ref. 24, p. 2-4]. This internal arrangement is illustrated below in Figure 79.
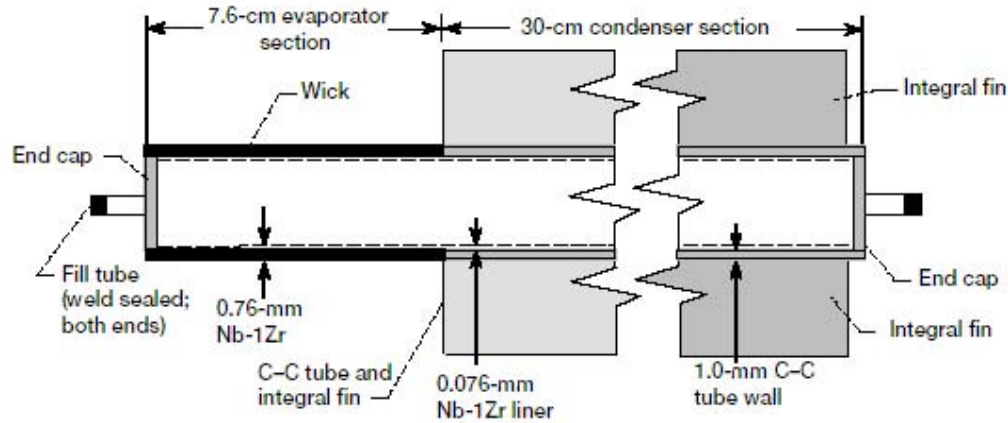
Figure 79.   Internal Arrangement of C-C Heat Pipe [from Ref. 24, p. 4]

Photographs of the heat pipe before and after assembly is shown below in Figure 80. The braze foil depicted below is used to adhere the liner to the tube.
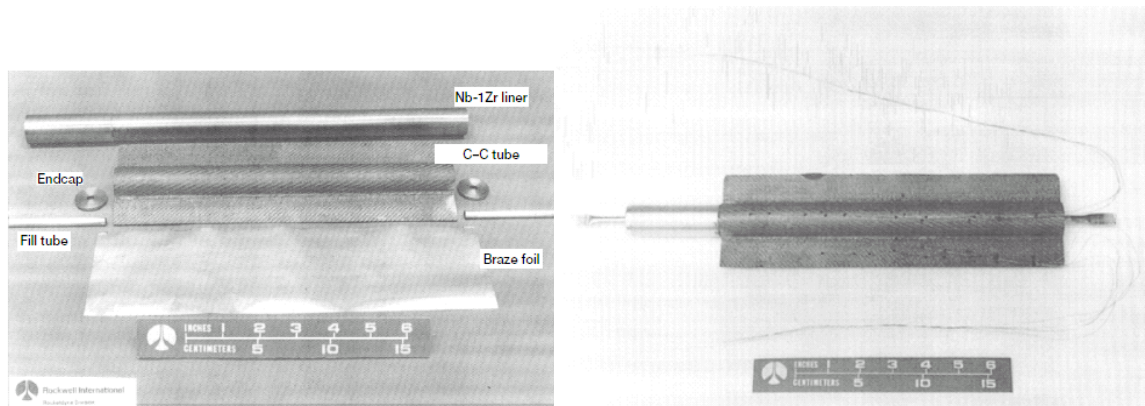
Figure 80.   C-C Heat Pipe Before (Left) and After (Right) Assembly [from Ref. 24, p.5-6]

The integral fins are a key reason for the C-C's impressive specific mass characteristics and deserve particular attention. Fins increase the reliability and may ultimately decrease the specific mass of an individual heat pipe space radiator element. They increase reliability by providing a radiating surface that will not be rendered useless by a single micrometeoroid puncture. This argument is similar to the previous discussion of the benefits of heat pipe radiators over conventional pumped loop systems. The fins decrease the specific mass of a space radiator element by providing more surface area for radiation.

The heat pipe shown above was tested for 11 hours at approximately 650K. Internal recirculation of the potassium working fluid was demonstrated in the finned C-C condenser tube with Nb-1Zr liner. Similar successful results were also obtained in the 400-450 K temperature range using another finned C-C condenser section with a stainless steel liner and demineralized water as the working fluid [Ref. 57, pp. 4-5]. The life time of water with a stainless steel liner is uncertain due to corrosive effects. Conversations with Dr. Juhasz indicate that water heat pipes have a potential lifetime in the 5-15 year range if copper-nickel alloys are chosen for the liner material. 1-2 cm diameter heat pipes would also have to deal with the much higher vapor pressure of the water working fluid (perhaps 16 atmospheres in the temperature range of interest here) and that would necessitate an increase in liner thickness. The increase is considered negligible for specific mass computations. [Ref. 54]

These demonstrations encourage speculation about the consequences for heat pipe radiator elements. The key to reducing specific mass is larger fins. Larger fins increase the surface area proportionally more than they increase the mass because the fins are thin and have low volume. The problem with larger fins is that they, unlike the heat pipe which transports heat to them for rejection, are not at the same temperature throughout. Instead the fin temperature decreases from it root at the condenser tube to the fin edge. Recall from Equation (10) that the radiated power output is proportional to the fourth power of average radiator temperature and it is clear that an efficient radiator must maintain this temperature as high as possible. The thermal conductivity of the fin material therefore determines how large a fin can reasonably be. Higher thermal conductivity implies that a fin will be more nearly isothermal and can be larger without significantly reducing average radiator temperature.

This is where the ever advancing state of the art in carbon composites comes in. Continual improvements in the capabilities of composites have been the norm in the industry. Demand for better carbon fibers persists across large sectors of the economy and drives these developments. Juhasz offers an example of the benefits of this trend applied to space heat pipe radiators below in Figure 81.

120

| Material	T300	P95 WG	K 1100
Thermal conductivity, W/mK	50–80	300–500	750–1000
Heat pipe dimensions, cm			
Length, L	91.4	91.4	91.4
Shell diameter, D	2.5	2.5	2.5
Width, W	2.5	5	7.5
Thickness, T	0.1	0.1	0.1
Heat pipe components mass, g			
C–C shell	169.5	214.0	254.5
Liner with evaporator	41.2	41.2	41.2
End caps	13.1	13.1	13.1
Fill tubes	7.2	7.2	7.2
Braze	22.5	22.5	22.5
Foil wick	24.0	24.0	24.0
Working fluid	13.5	13.5	13.5
Total mass, g	291.0	335.5	376.0
One-sided radiating area, m^2	0.0691	0.116	0.16
Specific mass, kg/m^2	4.21	2.89	2.35
Two-sided radiating area, m^2	0.1382	0.232	0.32
Specific mass, kg/m^2	2.11	1.45	1.18
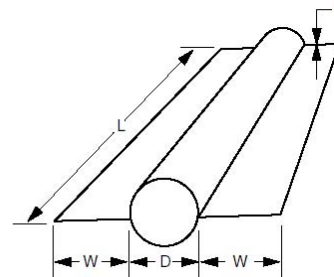
Figure 81.　　　Comparison of Specific Mass for Three C-C Materials [from Ref. 24, p.3]

This figure demonstrates the ability of higher thermal conductivity materials to permit larger fin widths (W) and reduce the specific mass of the radiator element. The thermal conductivity of the three C-C materials (T300, P95 WG, and K1100) increases from left to right. The prototype heat pipe described above was made of T300. Some test sections were fabricated out of the P95 WG. The K1100 has seen experimental use in other spacecraft thermal control applications but not yet as a heat pipe material [Ref. 58]. K1100, as shown in the figure, has the potential to reduce the overall radiator mass to 43% of the ISS radiator panels discussed previously.

The present work is not primarily concerned with the benefits of advanced radiators but the combination of TPV's high efficiency with the carbon-carbon heat pipe's low specific mass was too tempting to dismiss. The Excel model was used to compare two systems: the reference thermoelectric SP-100 with its beryllium-titanium heat pipe radiators replaced with finned carbon-carbon ones and the TPV based system with 0.52 eV bandgap and 85% efficient spectral control defined in Chapter VI. The reference SP-100 system with the C-C radiator massed 4334 kg. The radiator area for the TPV system is identical to the previous case and only the mass changes due to the lower specific mass of the C-C radiators. The results appear below in Figure 82.
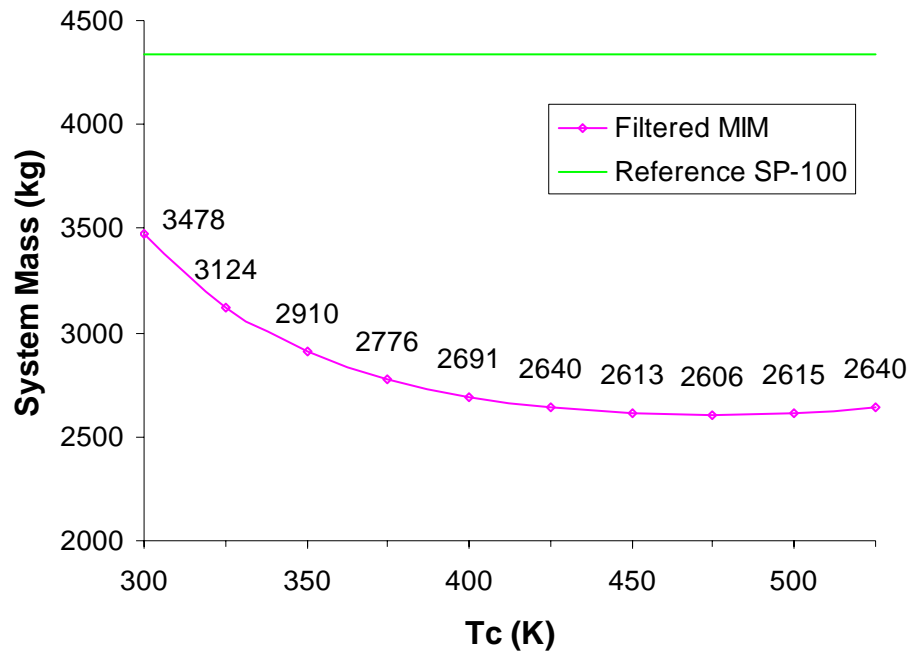
Figure 82.   System Mass vs. Tc with C-C Heat Pipe Radiators

The minimum mass here is 2606 kg. This is a 40 % reduction from the modified SP-100 system. This power system masses 26 kg for every kW of electrical power it produces.

LIST OF REFERENCES

l.   H. G. Rickover, *The Journal of Reactor Science and Engineering*, June 1953.

2.   NASA Jet Propulsion Laboratory, Mars Microrover Power Subsystem Website (http://mars.jpl.nasa.gov/MPF/roverpwr/power.html), last accessed 2 October 2004.

3.   NASA Jet Propulsion Laboratory, Mars Expedition Rover Mission Website (http://marsrovers.jpl.nasa.gov/mission/spacecraft_rover_energy.html), last accessed 2 October 2004.

4.   NASA Jet Propulsion Laboratory, Jupiter Icy Moons Orbiter Website (http://www.jpl.nasa.gov/jimo), last accessed 29 September 2004.

5.   R. H. Frisbee, "Advanced Space Propulsion for the 21st Century", Journal of Propulsion and Power, Vol. 19, No. 6, pp. 1129-1154.

6.   Spectrolab Photovoltaic Products, Photovoltaic Products Webpage (http://www.spectrolab.com/DataSheets/Panel/panels.pdf), last accessed 21 November 2004.

7.   V. L. Teofilo, *Advanced Space Power Sources*, notes from symposium at Naval Postgraduate School (unpublished), 6 November 2003.

8.   J. Dearien and J. Whitbeck, "Advanced Multimegawatt Space Nuclear Power Concepts" in *Thermal-Hydraulics for Space Power, Propulsion and Thermal Management System Design*, W. Krotiuk, ed., Progress in Astronautics and Aeronautics, American Institute of Aeronautics and Astronautics, Inc., Washington, D.C., 1990, Vol. 122, 41-46.

9.   J. A. Angelo and D. Buden, *Space Nuclear Power*, Orbit Book Company, Inc., Malabar, FL, 1985.

10.   L. S. Mason, "A Power Conversion Concept for the Jupiter Icy Moons Orbiter," NASA-TM-2003-212596/AIAA-2003-6007, September 2003.

11.   M.S. El-Genk, Notes from *Space Nuclear Power Systems and Static Energy Conversion Technologies*, Short Course on Space Nuclear Power and Propulsion Systems, Albuquerque, N.M., 7-8 February 2004.

12.   E. S. Pedersen, *Nuclear Energy in Space*, Prentice-Hall Inc., Englewood Cliffs, N.J., 1964.

13.   S. K. Borowksi, "Comparison of Fusion/Antiproton Propulsion Systems for Interplanetary Travel", NASA-TM-107030/AIAA-87-1814, NASA Lewis Research Center, July 1987.

14.   S. S. Voss, "TOPAZ II System Description", LA-UR-94-4, Los Alamos National Laboratory, Los Alamos, NM, 1994.

15. A. Kirpich, G. Kruger, D. Matteo, and J. Stephen, "SP-100 Space Reactor Power System", in *Thermal-Hydraulics for Space Power, Propulsion and Thermal Management System Design*, Progress in Astronautics and Aeronautics, W. J. Krotiuk, ed., Vol. 122, pp. 29-39.

16. D. Buden, "Summary of Space Nuclear Reactor Power Systems (1984-1993)", in *A Critical Review of Space Nuclear Power and Propulsion. (1984-1993)*, American Institute of Physics, New York, NY, 1994.

17. C. Kittel and H. Kroemer, *Thermal Physics*, 2nd Ed., W.H. Freeman and Company, New York, NY, 1980.

18. R.V. Anderson, D. Bost, W.R. Determan, R.B. Harty, B. Katz, V. Keshishian, D. Kramer, A. F. Lillie, E. Matlin, M. P. Moriarty, D. K. Nelson, and W. B. Thomson, "Space-Reactor Electric Systems: Subsystem Technology Assessment", DE8301038, Rockwell International, Energy Systems Group, 29 March 1983.

19. F. L. Pedrotti and L. S. Pedrotti, *Introduction to Optics*, 2nd ed., Prentice Hall, Upper Saddle River, NJ, 1993.

20. A. Juhasz, "An Analysis and Procedure for Determining Space Environmental Sink Temperatures with Selected Computation Results", NASA/TM-2001-210063, NASA Glenn Research Center, Cleveland, OH, January 2001.

21. D. G. Gilmore, *Spacecraft Thermal Control Handbook*, The Aerospace Corporation, El Segundo, CA, 2002.

22. B. W. Maryott, "ISS Thermal Control System" in <u>Astronaut Computer Based Training Volume 3</u> [CD-ROM], NASA Johnson Space Flight Center, 2000, cited 11 October 2004.

23. C. Silverstein, *Design and Technology of Heat Pipes for Cooling and Heat Exchange*, Hemisphere Publishing Corporation, Washington, D.C., 1992.

24. A. J. Juhasz, "Design Considerations for Lightweight Space Radiators Based on Fabrication and Test Experience With a Carbon-Carbon Composite Prototype Heat Pipe", NASA/ TP-1998-207427/REV1, NASA Glenn Research Center, Cleveland, OH, September 2002.

25. P.D. Dunn and D.A Reay, *Heat Pipes*, 4th ed., Elsevier Science Inc., Tarrytown, NY, 1994.

26. Microsoft Corporation, MSN Encarta website, (http://encarta.msn.com/media_461551264/Capillary_Action.html), last accessed 14 October 2004.

27. G. P. Peterson, *An Introduction to Heat Pipes: Modeling, Testing, and Applications*, John Wiley & Sons, Inc., New York, NY, 1994.

28. B. G. Streetman and S. Banerjee, *Solid State Electronic Devices*, 5th Ed., Prentice Hall, Upper Saddle River, NJ, 2000.

29. S. Michael, EC 3230, Space Power and Radiation Effects Lecture Notes, Naval Postgraduate School, Winter 2004, (unpublished).

30. B. Wernsman, R. R. Siergiej, S. D. Link, R. G. Mahorter, M. N. Palmisiano, R. J. Wehrer, R. W. Schultz, G. P. Schmuck, R. L. Messham, S. Murray, C. S. Murray, F. Newman, D. Taylor, D. M. DePoy, and T. Rahmlow, "Greater Than 20% Radiant Heat Conversion Efficiency of a Thermophotovoltaic Radiator/Module System Using Reflective Spectral Control", *IEEE Transactions of Electron Devices*, Vol. 41, No. 3, March 2004, pp. 512-515.

31. B. Davenport, "Advanced Thermophotovoltaic Cells Modeling, Optimized for Use in Radioisotope Thermoelectric Generators (RTGs) for Mars and Deep Space Missions", Master's Thesis, Naval Post Graduate School, Monterey, CA, June 2004.

32. P. F. Baldasaro, J. E. Reynolds, G. W. Charache, D. M. DePoy, C.T. Ballinger, T. Donovan, and J. M. Borrego, "Thermodynamic analysis of thermophotovoltaic efficiency and power density tradeoffs", *Journal of Applied Physics*, Vol. 89, No. 6, March 2001, pp. 3319-3327.

33. K. Emery, "Characterizing thermophotovoltaic cells", *Semiconductor Science and Technology*, Vol. 18, No. 5, May 2003, pp. S228-S231.

34. J. L. Gray and A. El-Husseini, "A Simple Parametric Study of TPV System Efficiency and Output Power Density Including a Comparison of Several TPV Materials", AIP Conference Proceedings, Vol. 358, No. 3, 1996, pp. 3-15.

35. G. Guazzoni and S. Matthews, "A Retrospective of Four Decades of Military Interest in Thermophotovoltaics", The Sixth International Conference on the Thermophotovoltaic Generation of Electricity, A. Gopinath, T.J. Coutts, J. Luther, eds., AIP Conference Proceedings, Vol. 738, American Institute of Physics, New York, NY, November 2004, pp 3-14.

36. A. De Vos, "The Endoreversible Theory of Solar Energy Conversion: a Tutorial", *Solar Energy Materials and Solar Cells*, Vol. 31, 1993, pp. 75-93.

37. P.S. Dutta, H. L. Bhat and V. Kumar, "The physics and technology of gallium antimonide: An emerging optoelectronic material", *Journal of Applied Physics*, Vol. 81, No. 9, May 1997, pp. 5821-5870.

38. O. V. Sulima, A. W. Bett. M. G. Mauk, F. Dimroth, P. S. Dutta, and R. L. Mueller, "Ga-Sb, InGaAsSb, InGaSb, InAsSbP and Ge TPV cells for low-temperature TPV applications", The Fifth International Conference on the Thermophotovoltaic Generation of Electricity, T. j. Coutts, G. Guazzoni, J. Luther, eds., AIP Conference Proceedings, Vol. 653, American Institute of Physics, New York, NY, September 2002, pp. 434-441.

39. T. Schlegl, F. Dimroth, A. Ohm, and A.W. Bett, "TPV Modules Based on GaSb Structures", The Sixth International Conference on the Thermophotovoltaic Generation of Electricity, A. Gopinath, T.J. Coutts, J. Luther, eds., AIP Conference Proceedings, Vol. 738, American Institute of Physics, New York, NY, November 2004, pp 285-293.

40. R. R. Siergiej, B. Wernsman, S.A. Derry, R.G. Mahorter, R.J. Wehrer, S.D. Link, M.N. Palmisiano, R.L. Messham, S. Murray, C.S. Murray, F. Newman, J. Hills, and D. Taylor, "20% Efficient InGaAs/InPAs Thermophotovoltaic Cells", The Fifth International Conference on the Thermophotovoltaic Generation of Electricity, T. j. Coutts, G. Guazzoni, J. Luther, eds., AIP Conference Proceedings, Vol. 653, American Institute of Physics, New York, NY, September 2002, pp. 414-423.

41. D. Wilt, R. Wehrer, M. Palmisiano, M. Wanlass, and C. Murray, "Monolithic interconnected modules (MIMs) for thermophotovoltaic energy conversion", *Semiconductor Science and Technology*, Vol. 18, No. 5, May 2003, pp. S209-S215.

42. J. M. Bierley, "A Parametric Design Study of InGaAs Micro-Thermophotovoltaic Cells Coupled with Various Emitters at Near and Far Spacing", Master's Thesis, Naval Post Graduate School, 2002.

43. M. Houts, et al., "Options for Development of Space Fission Propulsion Systems", in Proceedings of *Space Technology and Applications International Forum (STAIF-2001)*, Albuquerque, NM, AIP 552, American Institute of Physics, New York, NY, 2001, pp. 822-827.

44. L. Dutram, E. McNamara, S. Bailey, et al, "SP-100 Project Integration Meeting", NASA Jet Propulsion Laboratory, 19-21 July 1988, unpublished lecture notes, General Electric, 1988.

45. Spectrolab Corporation, Solar Panel Products Webpage, ('http://www.spectrolab.com/prd/prd.htm'), last accessed 13 November 2004.

46. P. M. Fourspring, D. M. Depoy, J. F. Beausang, E. J. Gratrix, R. T. Kristensen, T. D. Rahmlow, Jr., P. J. Talamo, J. E. Lazo-Wasem, and B. Wernsman, "Thermophotovoltaic Spectral Control", The Sixth International Conference on the Thermophotovoltaic Generation of Electricity, A. Gopinath, T.J. Coutts, J. Luther, eds., AIP Conference Proceedings, Vol. 738, American Institute of Physics, New York, NY, November 2004, pp 171-179.

47. R. J. Wehrer, M.W. Wanlass, D. Taylor, B. Wernsman, J.J. Carapella, R.W. Schultz, S.P. Ahrenkiel, D.M. Wilt, M.W. Dashiell, R.R. Siergiej, S.D. Link, and R.L. Messham, "0.52eV InGaAs/InPAs Thermophotovoltaic Cells", The Sixth International Conference on the Thermophotovoltaic Generation of Electricity, A. Gopinath, T.J. Coutts, J. Luther, eds., AIP Conference Proceedings, Vol. 738, American Institute of Physics, New York, NY, November 2004, pp 445-452.

48. J. F. Beausang, "The Thermodynamics of Thermophotovoltaics", Master of Physics Thesis, Rensselaer Polytechnic Institute, Troy, NY, 2002.

49. R. R. Siergiej, S. Sinharoy, T. Valko, R. J. Wehrer, B. Wernsman, S. D. Link, R. W. Shultz, and R. L. Messham, "InGaAsP/InGaAs Tandem TPV Device", The Sixth International Conference on the Thermophotovoltaic Generation of Electricity, A. Gopinath, T.J. Coutts, J. Luther, eds., AIP Conference Proceedings, Vol. 738, American Institute of Physics, New York, NY, November 2004, pp 480-488.

50. R. Wehrer, M. Wanlass, D. Wilt, B. Wernsman, R. Siergiej, and J. Carapella, "InGaAs Series-Connected, Tandem, MIM TPV Converters", 3rd World Conference on Photovoltaic Energy Conversion, K. Kurkawa, L. Kazmerski, B. McNelis, M. Yamaguchi, C. Wronski, W. Sinke, eds., IEEE, May 11-18, 2003, Osaka, Japan, pp. 892-895.

51. M.W. Wanlass and D. S. Albin, "A Rigorous Analysis of Series-Connected, Multi-Bandgap, Tandem Thermophotovoltaic (TPV) Energy Converters", The Sixth International Conference on the Thermophotovoltaic Generation of Electricity, A. Gopinath, T.J. Coutts, J. Luther, eds., AIP Conference Proceedings, Vol. 738, American Institute of Physics, New York, NY, November 2004, pp 462-470.

52. F. Dimroth, C. Baur, M. Meusel, S. van Riesen, A. W. Brett, "5-Junction III-V Solar Cells for Space Applications", 3rd World Conference on Photovoltaic Energy Conversion, K. Kurkawa, L. Kazmerski, B. McNelis, M. Yamaguchi, C. Wronski, W. Sinke, eds., IEEE, May 11-18, 2003, Osaka, Japan, pp. 616-621.

53. T. Takamoto, T. Agui, K. Kamimura, and M. Kaneiwa, " Multijunction Solar Cell Technologies-High Efficiency, Radiation Resistance, and Concentrator Applications", 3rd World Conference on Photovoltaic Energy Conversion, K. Kurkawa, L. Kazmerski, B. McNelis, M. Yamaguchi, C. Wronski, W. Sinke, eds., IEEE, May 11-18, 2003, Osaka, Japan, pp. 581-586.

54. A. J. Juhasz, Personal communication with author, 9 November 2004.

55. J. Kuhn, S. Benner, D. Butler and E. Silk, "Thermal and Mechanical Performance of a Carbon/Carbon Composite Space Radiator", Proceedings of the *Optomechanical Engineering and Vibration Control Conference*, SPIE Proc. 3786, pp. 162-178, 1999.

56. NASA Goddard Space Flight Center, Earth Observing 1 Website, (http://eo1.gsfc.nasa.gov/Technology/Docs_CCR.html), last accessed 21 October 2004.

57. A. J. Juhasz, "Composite Heat Pipe Development Status: Development of Lightweight Prototype Carbon-Carbon Heat Pipe With Integral Fins and Metal Foil Liner", NASA TM-106909, NASA Glenn Research Center, Cleveland, OH, May 1995.

58. K. C. Snyder, "High Conductivity Composite Sleeves for Large Nickel Hydrogen Cells", White Paper, Eagle Pitcher Technologies LLC, Long Beach, CA, 2000, available from Eagle Pitcher Technologies Website, (http://www.epcorp.com/EaglePicherInternet), last accessed 22 October 2004.

THIS PAGE INTENTIONALLY LEFT BLANK

INITIAL DISTRIBUTION LIST

1.   Defense Technical Information Center
        Ft. Belvoir, VA

2.   Dudley Knox Library
        Naval Postgraduate School
        Monterey, CA

3.   Dr. Sherif Michael
        Department of Electrical and Computer Engineering
        Naval Postgraduate School
        Monterey, CA

4.   Dr. Ashok Gopinath
        Department of Mechanical and Astronautical Engineering
        Naval Postgraduate School
        Monterey, CA

5.   CDR Stephen G. Bowen
        NASA-JSC
        Office Code CB
        Houston, TX

6.   Dr. Franklin Chang-Diaz
        NASA-JSC Advanced Space Propulsion Laboratory
        Office Code CB
        Houston, TX